2015

Investigation of Novel Applications of Nonlinear Optics: From Parametric Oscillation to Image Restoration

Pengda Hong
Lehigh University

Investigation of Novel Applications of Nonlinear Optics: From Parametric Oscillation to Image Restoration

by

Pengda Hong

A Dissertation

Presented to the Graduate Committee

of Lehigh University

in Candidacy for the Degree of

Doctor of Philosophy

in

Electrical Engineering

Lehigh University

August 2015

Approved and recommended for acceptance as a dissertation in partial fulfillment of the requirements for the degree of Doctor of Philosophy.

Prof. Yujie J.Ding
(Dissertation Advisor)

Date

Prof. Sushil Kumar
(Dissertation Advisor)

Accepted Date

Committee Members:

Prof. Yujie J.Ding
(Committee Chair)

Prof. Sushil Kumar
(Committee Chair)

Prof. Filbert J.Bartoli

Prof. D.Richard Decker

Prof. H.Daniel Ou-Yang
(Physics Department)

Dedicated to my Parents

Acknowledgements

First of all, I would like to express my greatest gratitude to my advisors Prof. Yujie Ding and Prof. Sushil Kumar. Without their supports, my research work can't be accomplished and this dissertation can't be finalized. Their insight in optics field study and broad knowledge brought me new horizon. I am always inspired by the bright mind of Prof. Ding, which always shocked me in a novel thinking pattern in research. Under his persistent supervision, I am very fortunate that I have chances to get into four different research topics in nonlinear optics.

I also would like to thank my Ph.D committee members Professor Filbert J.Bartoli, Professor Richard Decker and Professor Daniel Ou-Yang for their many valuable advices in my Ph.D dissertation and presentation. What is more, their good suggestions trigger me some new thinking in my research.

Especially I would like to thanks post-doctor Dr. Xingquan Zou in my research. He is not only my close collaborator, but also my close friend. I always gained passion in research and knowledge in optics from Dr. Zou. Through working with him, I learnt lots of technical skills starting from my joining of nonlinear optics group, and also new perception in optics research. I also would like to thanks Prof. Zhaojun Liu, who imparted me lots of experimental skills.

I also would like to thanks the graduate fellows Da Li, Xiaomu Lin, Ruolin Chen, Guan Sun and Pu Zhao for their help in my research.

I would like to thank my parents, sisters and brothers. With support, love and spiritual encouragement of my big family, I am always following my heart to pursuit the meaning of my life. I always am in debt to my elder brother, who took the responsibility of taking care of my parents. It

is his encouragement drives me to do my best in my research. I also want to thank all of my dear friends, all of you make my life colorful.

Finally, I would like to thanks the scholarships from Lehigh University in fully supporting my study and research.

Contents

List of Figures

Abstract

Nonlinear optical phenomena are the illustrations of the nonlinear responses of polarizations of media to electric fields. Since the first demonstration of frequency doubling from a Ruby laser in 1961, nonlinear optics has been intensively investigated. It has variety of applications from chemical sensing to image restoration.

An optical parametric oscillator (OPO) is a device whereby a pump frequency can be converted to two lower frequencies in a nonlinear medium. There are three key ingredients for an OPO, i.e. a pump laser beam, a nonlinear medium providing a gain for the oscillating parametric wave through the nonlinear polarization, and an optical feedback by use of a cavity. In an OPO based on a $KTiOPO_4$ (KTP) and $KTiOAsO_4$ (KTA) crystal composite consisting of periodically-switched plates, signal twins and idler twins are generated due to two quasi-phase-matching conditions, instead of a single signal and a single idler in a conventional OPO. The two signals or idlers within the twins have perpendicular polarizations. In addition, the frequency separation between the signal twins or idler twins, dictated by the length of each crystal plate, is insensitive to the pump frequency and crystal temperature. Therefore, the signal twins (idler twins) are highly coherent with each other. These three novel features make such a type of the OPO stand out for realizing certain applications such as image restoration and THz generation having unique advantages. Since the signal twins or idler twins have perpendicular polarizations, they can be used to restore blurred images, which is insensitive to polarization of an incoming beam. In contrast, such an application based on a

conventional OPO is sensitive to the polarization of the input beam. In addition, the twins can be heterodyned in a photodiode when their frequency separation is around 100 GHz, which can be used to detect carbon dioxide with an increased sensitivity and to simultaneously clean up the images blurred by atmospheric turbulence. For the AFB-KTP composite, the twins can be used in chemical sensing with a high sensitivity. It is worth noting that the frequency difference of the twin beams can be designed to be cover the range of 100 GHz to a few THz. Our theoretical analysis reveals that THz waves generated by mixing signal twins in a nonlinear medium have much significantly reduced quantum noise, compared with that by mixing a signal and an idler from a conventional OPO.

Raman spectroscopy is an important tool in studying properties of optical materials based on third-order nonlinear process. In order to analyze anti-Stokes signals, relatively high pump power is usually required. As a result, local heating effects make Raman peaks lose their frequency accuracy. Anti-Stokes signals can be enhanced in a waveguide structure of lithium niobate, such that relatively low pump power is needed for spectroscopic studies. Such an advantage may open up the possibility for developing a portable Raman spectroscopic device. In the waveguide, both the forward and the backward anti-Stokes spectra can be distinguished. By amplifying an anti-Stokes Raman-shifted output in a laser amplifier, the corresponding system can be used to extend the detectable wavelength range of a silicon avalanche photodiode. A coherent anti-Stokes Raman output can used for image restoration based on phase conjugation.

In this dissertation, I will focus on our investigations of novel nonlinear optical phenomena and applications based on second-order and third-order nonlinear processes. First of all, I will present our result on the generation of signal twins from an OPO based on KTA crystal twins, then

summarize our studies on the generation of the idler triplets by using an AFB-KTP composite and a bulk KTP crystal being placed in the same OPO cavity. I am also going to give an overview of our work on the generation of 2 μm from an AFB-KTP composite. Second, I will present our results on image restoration based on transmission and reflection configurations. The reflection geometry is more practical than the transmission geometry in a field application. Third, I will summarize our key results on the generation of terahertz (THz) waves by frequency-mixing idler twins in a nonlinear crystal. We have observed noise reduction and linewidth narrowing, resulting in the enhancement of the THz output power. Fourth, I are going to summarize our findings on the enhancements of forward and backward anti-Stokes signals generated by a lithium niobate waveguide. We have observed significant frequency shifts of certain Raman peaks.

Chapter 1 Introduction

1.1 Motivation

Shortly after the invention of laser, nonlinear optics has attracted lots of attentions in fundamental and technical research. Various nonlinear phenomena have been discovered, such as sum frequency generation, Kerr effect, four-waves mixing and so on. The first three research study in this dissertation are based on second order nonlinear process, they are investigation of optical parametric oscillation, image restoration by phase conjugation and THz generation by difference frequency generation. The fourth study about single photon detection is based on third order nonlinear process. Optical parametric oscillation is an important tool in gas sensing, i.e. CO_2 and methane, bio-medicine and quantum communication. For conventional OPO based on single nonlinear bulk crystal, one idler and one signal are generated for satisfying condition of birefringence. They can be used as source for difference frequency generation for THz or GHz waves. However, the frequency difference between idler and signal is sensitive to temperature fluctuation and pump beam

wavelength, which makes it unpractical for utilization. What is more, walk-off effect for *e* ray also casts higher threshold for conventional OPO. We would like to introduce pair of nonlinear crystals for generation of signal twins or idler twins. The waves generated from frequency difference should be insensitive to temperature fluctuation and change of pump wavelength. One of the features for this configuration is that the frequency separation between signal twins or idler twins is dedicated by crystal thickness, so we can design the frequency of wave generated through controlling the length of crystal. Furthermore, walk-off effect is also minimized. For generation of 1.5 μm signal twins, we used two 15 mm KTA crystals. The pair of signal twins can be used for GHz generation by heterodyning, and it can be used for image restoration and CO_2 detection in atmospheric environment at the same time. One of the advantages for this scheme is that we do not need to use another pump beam for this process. For OPO, we also study the properties of multi-wavelength signals at 1 μm from coupled KTP OPO, and 2 μm beams generated from KTP stacks based OPO. Such twin beams at 1 μm or 2 μm should be highly coherent for THz generation.

Optical phase conjugation can generate the replica of input beam after phase distortion, and it has been explored for image restoration, such as in removing the scattering from bio-tissue and recovering image quality. It is also has been demonstrated for compensation of pulse distortion and modal dispersion. In previous strategies for image recovery by phase conjugation, they suffered some shortcomings, such as high pump power needed for four-waves mixing, long response time for photorefractive effect and particular polarization of pump beam needed, so they can't meet the requirements in image correction blurred by dynamic atmospheric turbulence, especially for instantaneous response speed, since the atmospheric turbulence has the feature of random fluctuation. We would like to propose novel scheme based on second order nonlinear process for

image restoration, it has features of real-time response speed, low pump power and polarization insensitivity to input beam. What is more, dynamic atmospheric turbulence is introduced by rotating a phase plate. It may be the only scheme for achieving image restoration in atmospheric turbulence.

THz waves have wide applications in imaging, materials characterization and radar. In order to bridge the THz gap, the frequency range between 0.1 THz to 3 THz, various approaches for THz generations have been proposed, such as quantum cascade lasers, optical rectification and so on. Among these methods, frequency difference generation bears the advantages of room temperature operation and set-up compatibility. THz generation by mixing idler and signal beams from conventional OPO based on single KTP has been demonstrated, however, if the OPO is not injection seeded, oscillation will originate from quantum noise and such large quantum noise affects the quality of THz wave. In contrast, for signal twins and idler twins generated from AFB-KTP composite, they are highly coherent, such as owning the same phase, such that the phase difference between them can always be cancelled in DFG process for THz generation. As a result, the quantum noise is expected to be significantly reduced. We would like to theoretically study the properties of THz wave for their output power, linewidth and stability. The mechanism behind will be revealed by our semi-classical approaches. This study will give new perception in THz generation.

Raman is a powerful tool in revealing the properties of materials. Due to much lower occupation number for higher energy electrons, anti-Stokes signal is much weaker than Stokes signal. As a result, usually higher pump power is used to generate measurable anti-Stokes signal, which would cause local heating effects. In order to solve this problem, we would like to develop single photon detection system with low pump power, this is a very important step for developing portable single photon detection system. Another purpose of our experiment is that we would like to explore silicon

photodiode for single photon detection, since it has higher conversion efficiency and lower dark count number than InGaAs photodiode. Through utilization of silicon photodiode, the measurement sensitivity will be increased.

1.2 Fundamental of Nonlinear Optics

Maxwells' equations in (1) and (2) have been widely used in describing the propagation of electromagnetic waves in space within medium. Different from linear optics, for nonlinear optics, the polarization term consists of linear term $\vec{P}_L$ and nonlinear term $\vec{P}_{NL}$ [1, 2]. The nonlinear term is the driving force for the nonlinear phenomena observed, such as sum frequency generation and difference frequency generation of second order nonlinear process and Kerr effect of third order nonlinear process.

$$\nabla \times \vec{H} = \frac{\partial}{\partial t}(\varepsilon_0 \vec{E} + \vec{P}) \qquad (1)$$

$$\nabla \times \vec{E} = -\frac{\partial}{\partial t}(\varepsilon_0 \vec{H}) \qquad (2)$$

Where $\vec{P}$ is the total polarization, and it can be expressed as:

$$\vec{P} = \vec{P}_L + \vec{P}_{NL} = \varepsilon_0 \chi_L \vec{E} + \vec{P}_{NL}$$

And $\vec{P}_{NL} = \varepsilon_0(\chi^{(2)}E^2 + \chi^{(3)}E^3 + \chi^{(4)}E^4 + \cdots\cdots\cdots)$, $\chi^{(2)}, \chi^{(3)}, \chi^{(4)}$ ... ... correspond to second order nonlinear coefficient, third order nonlinear coefficient, forth order nonlinear coefficient and other higher order nonlinear coefficients.

In combination of Eqs. (1) and (2), we can get the equation for propagation of electromagnetic waves:

$$\nabla^2 \vec{E} = \mu_0 \varepsilon_0 \frac{\partial^2}{\partial t^2} \vec{E} + \mu_0 \frac{\partial^2}{\partial t^2} \vec{P}_{NL} \quad (3)$$

This wave equation shows the nonlinear polarization term is the driving force for the propagation

of electromagnetic waves in nonlinear crystal. For example, for KTA or KTP crystal, when the nonlinear crystal is pumped by a laser beam, the electric dipole will be generated. Since the nonlinear dipole exists, it will radiate other frequency waves, this will make frequency conversion happen, such as frequency down conversion and frequency up conversion. If the nonlinear crystal is continuously pumped by laser, the generated waves will be accumulated in space. The efficiency of accumulation in energy depends on the phase matching condition for pump beam and generated beams.

In first three topics of this dissertation, I will focus on second order nonlinear process. It lies on the second order nonlinear coefficient, which is much larger than third order and other higher order nonlinear coefficients. If intensity of nonlinear polarization is larger enough, we can directly use optical parametric amplification or optical parametric generation. If it is small, usually a cavity is introduced to form optical parametric oscillator for resonating the fluorescence to couple out of measurable energy. OPO is a very fundamental and important tool and it will be discussed in Chapter 2. Fig. 1.1 shows the schematic of sum frequency generation and difference frequency generation, and the schematic of energy transfer is shown in Fig. 1.2. If the nonlinear crystal is pumped by two different laser beams with frequency of ω_1 and ω_2. For a simply model,

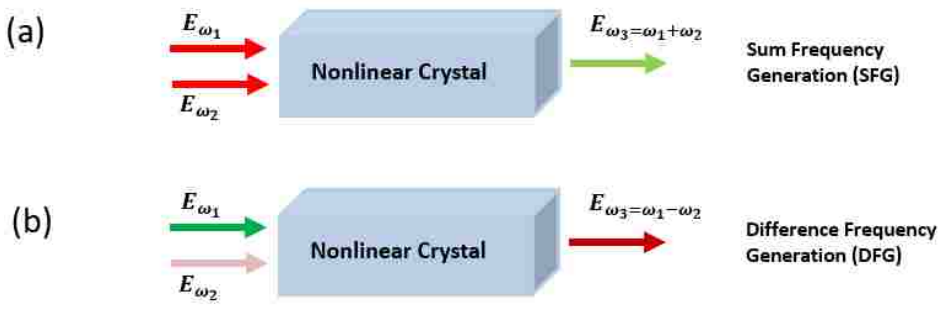

Fig. 1.1. Illustration of (a) sum frequency generation and (b) difference frequency generation.

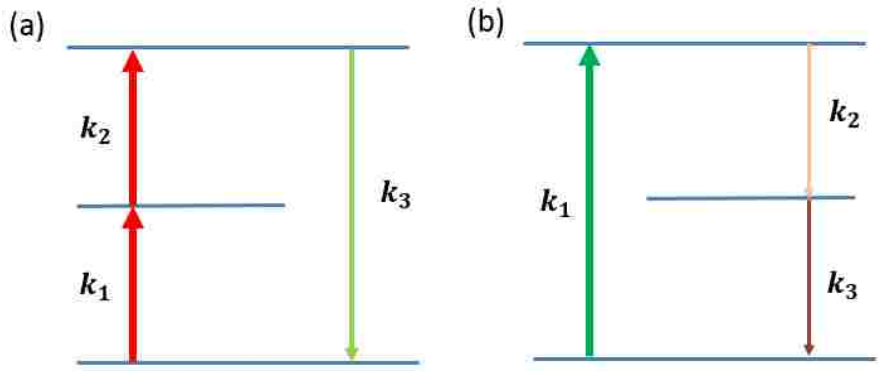

Fig. 1.2. Schematic of photons transfer in the process of (a) sum frequency generation and (b) difference frequency generation.

one can express the two waves as:

$$E_J = E_j \sin(\omega_j t) \quad (4)$$

$$E_L = E_l \sin(\omega_l t) \quad (5)$$

After photon mixing in nonlinear crystal, we can get the second order nonlinear polarization as the following:

$$\begin{aligned}\left(\vec{P}_{NL}\right)_i &= 2\varepsilon_0 d_{ijk}\{E_j \sin(\omega_j t) + E_l \sin(\omega_l t)\}^2 \\ &= 2\varepsilon_0 d_{ijk}[{E_j}^2 sin^2(\omega_j t) + {E_l}^2 sin^2(\omega_l t) + 2E_j \sin(\omega_j t) E_l \sin(\omega_l t)] \\ &= 2\varepsilon_0 d_{ijk}[1 - \tfrac{1}{2}E_j \sin(2\omega_j t) - \tfrac{1}{2}E_l \sin(2\omega_l t) + E_j E_l \cos(\omega_j - \omega_l)t - \\ &\quad E_j E_l \cos(\omega_j + \omega_l)t] \end{aligned} \quad (6)$$

Where d_{ijk} is the nonlinear susceptibility tensor, and $d_{ijk} = 2\chi^{(2)}_{ijk}$.

In expression (6), there are five different terms for different frequencies generated: 0, $2\omega_j$, $2\omega_l$, $\omega_j + \omega_l$, $\omega_j - \omega_l$. The first term corresponds to optical rectification, $2\omega_j$, $2\omega_l$ represent second harmonics generation, $\omega_j + \omega_l$ term corresponds to sum frequency generation, $\omega_j - \omega_l$ term corresponds to difference frequency generation. If the frequency of two pump beams are the same, $\omega_j + \omega_l$ term is also second harmonic generation (SHG). For $\omega_j - \omega_l$ term, under the condition that $\omega_j \approx \omega_l$, we have $|\omega_j - \omega_l| \ll \omega_j$, this can be used in THz generation by DFG in nonlinear crystal [3, 4]. Phase conjugation from DFG for image restoration will be demonstrated in Chapter

3.

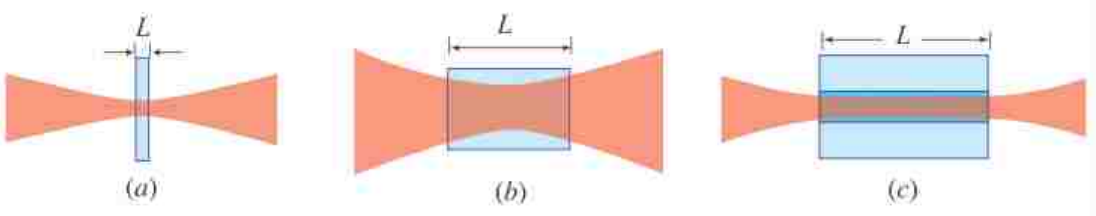

Fig. 1.3. Illustration of interaction of beam and nonlinear materials in (a) thin material, (b) thick material and (c) waveguide.

Conversion efficiency is an important issue in nonlinear optics, three most general cases in studying conversion efficiency affected by focusing are illustrated in Fig. 1.3 [5]. The efficiency of second harmonic generation can be determined as:

$$\eta_{SHG} = C^2 \frac{L^2}{A} P \qquad (7)$$

Where C is a constant, and it is proportional d^2 to and ω^2. L is the interaction length, A is the spot size and P is the pump power.

From the expression of (7), one can see that in order to reach the maximum value of SHG efficiency, on one hand, the suitable pulsed laser can be used, for example, femtosecond laser or other high peak power laser, on the other hand, one can maximize the ratio of $\frac{L^2}{A}$ [5]. Under the condition that the nonlinear crystal length L is long enough and spot size A is fixed, the interaction length L is confined by diffraction limit. For Gaussian beam, $\frac{L^2}{A}$ is equivalent to $\frac{4A}{\lambda^2}$, which means that if the pump beam is focused on the largest spot size, one can get the maximum SHG efficiency, thick nonlinear crystal falls into this case [Fig. 1.3(b)]. If it is thin nonlinear material, as illustrated in Fig. 1.3(a), we should focus the pump beam into smallest spot size. For waveguide structure in Fig. 1.3(c), we usually slightly focus the pump beam into the waveguide. In Chapter 5, we investigate generation of backward and forward anti-Stokes from lithium niobate waveguide. Similar to the case of SHG, two objectives are used for coupling 1 μm beam into waveguide. The maximum

coupling efficiency is determined by the matching between focused beam size and width of waveguide. One of the technical considerations in focusing pump beam is that pump intensity should be below the damage threshold for nonlinear crystal. The above discussion is also valid for DFG.

d_{ijk} is the 3×3×3 tensor, due to Kleinman's symmetry, it reduces to 6×3 tensor. After the contracted notation is introduced for d_{ijk}, the nonlinear polarization for second order nonlinear process can be expressed as following:

$$\begin{pmatrix} P_x^{(2)}(\omega_3) \\ P_y^{(2)}(\omega_3) \\ P_z^{(2)}(\omega_3) \end{pmatrix} = 4\varepsilon_0 \begin{pmatrix} d_{11} & d_{12} & d_{13} & d_{14} & d_{15} & d_{16} \\ d_{21} & d_{22} & d_{23} & d_{24} & d_{25} & d_{26} \\ d_{31} & d_{32} & d_{33} & d_{34} & d_{35} & d_{36} \end{pmatrix} \begin{pmatrix} E_x(\omega_1)E_x(\omega_2) \\ E_y(\omega_1)E_y(\omega_2) \\ E_z(\omega_1)E_z(\omega_2) \\ E_y(\omega_1)E_z(\omega_2)+E_z(\omega_1)E_y(\omega_2) \\ E_x(\omega_1)E_z(\omega_2)+E_z(\omega_1)E_x(\omega_2) \\ E_x(\omega_1)E_y(\omega_2)+E_y(\omega_1)E_x(\omega_2) \end{pmatrix} \quad (8)$$

In the practical study, the spatial symmetry of nonlinear medium should be considered for nonlinear susceptibility tensor, some of elements will become zero and some of the survived elements are the same. Following are nonlinear susceptibility tensor of some key nonlinear crystals used in my investigation:

For potassium titanyl phosphate, ($KTiOPO_4$ or KTP), it is orthorhombic, the expression of d_{ijk} is given as:

$$d_{ijk} = \begin{pmatrix} 0 & 0 & 0 & 0 & d_{15} & 0 \\ 0 & 0 & 0 & d_{24} & 0 & 0 \\ d_{31} & d_{32} & d_{33} & 0 & 0 & 0 \end{pmatrix}$$

The tensor for potassium titanyle arsenate ($KTiOAsO_4$ or KTA) also has the same form.

For GaP, it is cubic structure, the expression of d_{ijk} is given as:

$$d_{ijk} = \begin{pmatrix} 0 & 0 & 0 & d_{14} & 0 & 0 \\ 0 & 0 & 0 & 0 & d_{25} & 0 \\ 0 & 0 & 0 & 0 & 0 & d_{36} \end{pmatrix} \qquad \text{where } d_{14} = d_{25} = d_{36}.$$

GaN and GaAs also belong to cubic structure, so their nonlinear susceptibility tensors can be expressed as the tensor of GaP.

For lithium niobate, it is trigonal structure, the expression of d_{ijk} is given as:

$$d_{ijk} = \begin{pmatrix} 0 & 0 & 0 & 0 & d_{15} & d_{16} \\ d_{21} & d_{22} & 0 & d_{24} & 0 & 0 \\ d_{31} & d_{32} & d_{33} & 0 & 0 & 0 \end{pmatrix} \qquad \text{where } d_{16} = d_{21} = -d_{22}, \quad d_{31} = d_{32}$$

$$d_{15} = d_{24}.$$

The specific value of the elements of tensors for the above materials, one can check Ref. [6].

1.3 Outline of Dissertation

In this dissertation, novel applications of nonlinear optics in four research topics are demonstrated: optical parametric oscillation, image restoration, THz generation and single photon detection.

In chapter 2, the concept of walk-off correction for OPO is introduced. Three different types of OPO are investigated for various applications: generation of signal twins at 1.5 μm from two inverted KTAs OPO, multi-wavelength signals at 1 μm beams from coupled OPO and 2 μm degenerate beams from KTP stacks based OPO.

In chapter 3, polarization-insensitive image restoration by phase conjugation in second order nonlinear crystal is demonstrated. Simulated atmospheric turbulence is introduced for phase distortion. Transmission and reflection configurations have been achieved. Our earlier work using a homemade plate to distort wave front will also be introduced.

In chapter 4, we demonstrate that idler twins generated from AFB-KTP composite are highly coherent, THz generated from such pair of idlers is insensitive to the temperature fluctuation. One order magnitude higher of THz output power is measured, compared with that of mixing signal-idler from conventional OPO. Theoretical work by semi-classical approach will be shown in this

session.

In chapter 5, forward and backward anti-Stokes signals generated from lithium niobate bulk material and waveguide are studied. An enhancement of signal intensity from waveguide is observed at low pump power and the spectra for these two configurations show unique features.

Conclusions will be made in Chapter 6, and future work for the above topics will be also proposed.

Chapter 2 Optical Parametric Oscillation

2.1 Introduction to Optical Parametric Oscillation (OPO)

2.1.1 Configuration of OPO

Since the first demonstration of Optical parametric oscillator in 1965 at Bell lab by Joseph Giordmaine and Bob Miller, it has been widely explored for extending the band of conventional laser source, and has applications in spectroscopy [7], microscope [8], quantum communication [9] and remote sensing [10]. OPO has the feature of all solid state, wavelength tenability and room temperature operation. It is also important source of squeeze light for quantum optics study.

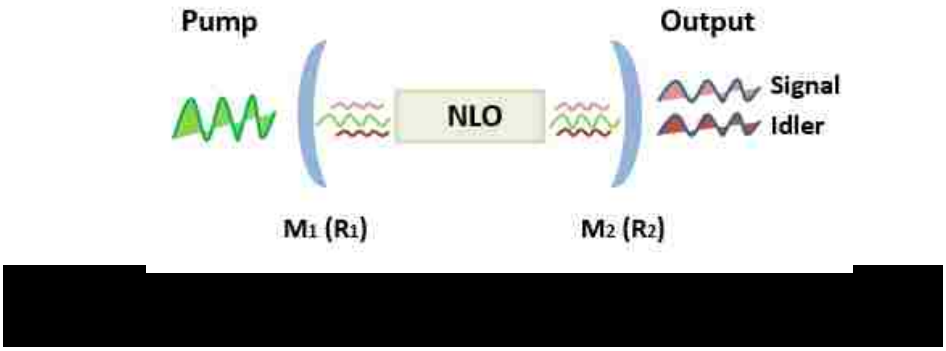

The simple schematic of OPO is shown in Fig. 2.1. Pump beam is used to excite a nonlinear crystal in OPO cavity, one signal and one idler beams are coupled out of cavity. For type II nonlinear process, pump beam, signal and idler beams need to satisfy the phase matching condition:

$$\frac{2\pi}{\lambda_p} n_p(o) - \frac{2\pi}{\lambda_s} n_s(e) - \frac{2\pi}{\lambda_i} n_i(o) = 0 \qquad (1)$$

and conservation of photon energies:

$$\frac{1}{\lambda_p} = \frac{1}{\lambda_s} + \frac{1}{\lambda_i} \qquad (2)$$

For OPO, there are three key ingredients: (a) Pump source is required to excite nonlinear crystal; (b) Nonlinear crystal provides parametric gain; (c) Cavity is incorporated to provide optical feedback, which is similar to laser.

For the unseeded OPO, the parametric oscillation starts from quantum noise, for example, it may begin from E_{w_1}, and then the nonlinear polarization term $P_{w_2}^{(NL)}$ is generated, which is defined as $P_{w_2}^{(NL)} = \chi^{(2)} E_p E_{w_1}^*$. It is the driving term for radiation of E_{w_2} and results into parametric gain. Similarly, OPO also may start from E_{w_2} the corresponding nonlinear polarization term $P_{w_1}^{(NL)}$ will be generated, which is the driving term for radiation of E_{w_1}. The bandwidth of signal and idler generated from unseeded OPO is broad banded, this is quite different from seeded OPO.

One of the difficult issues in nonlinear process lies in the spatial overlap of extraordinary ray and ordinary ray, this originates from the difference in their dispersion relations and group velocity. In Fig. 2.2, the schematic of extraordinary ray and ordinary ray is demonstrated. Extraordinary ray is in the plane formed by *z* axis and wave vector, while ordinary ray is perpendicular to the plane formed by *z* axis and wave vector.

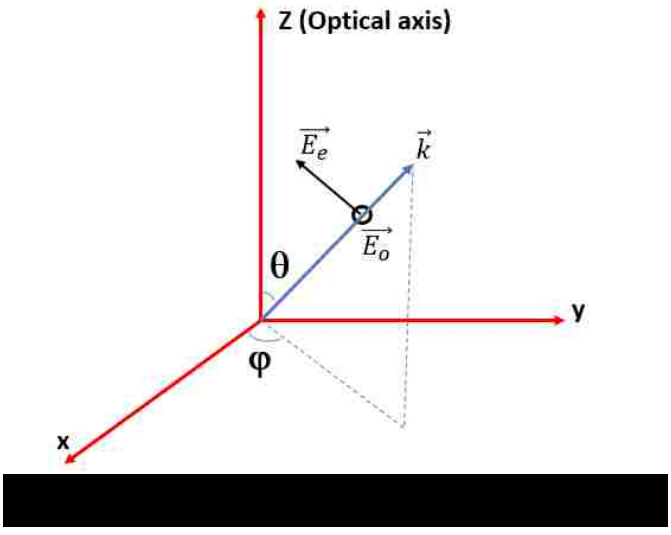

2.1.2 Walk-off Correction

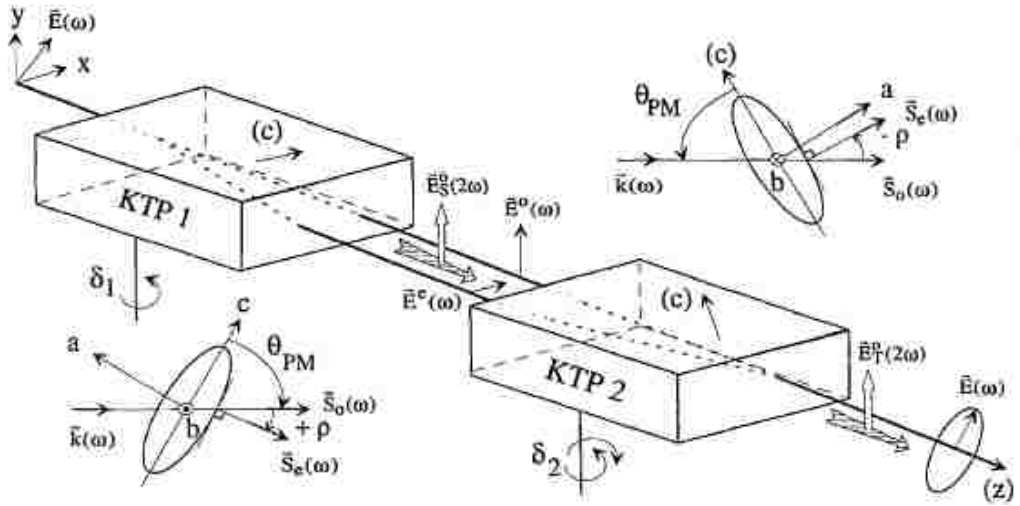

Fig. 2.3. Illustration of walk-off effect on extraordinary ray in type II nonlinear process.

Spatial walk-off effect on extraordinary ray in type II OPO is demonstrated in Fig. 2.3 [11]. As shown in figure, a spatial walk-off effect is casted on extraordinary ray, such effect will significantly increase the threshold of OPO and limit its conversion efficiency [12]. In order to overcome this disadvantage, a second identical nonlinear crystal is introduced into cavity for walk-off correction.

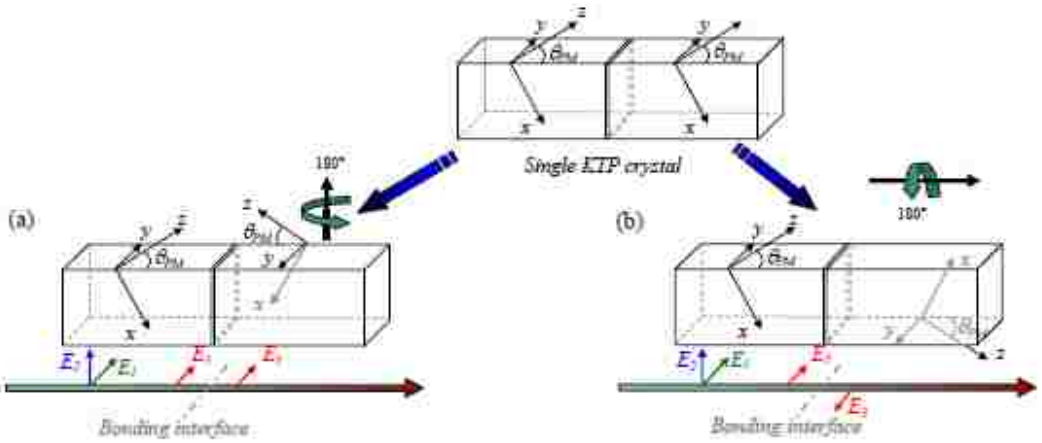

Fig. 2.4. Schematic demonstration of walk-off correction through bonding two identical KTPs with (a) the same nonlinear effective coefficient, (b) opposite nonlinear effective coefficient.

Fig. 2.4 illustrates two schemes of walk-off correction through attaching two identical KTPs with the same or opposite nonlinear coefficient [13]. After second KTP is introduced, the walk-off effect caused by the first KTP is compensated by second KTP. Fig. 2.4(a) illustrates that two KTP is bonding through head to head configuration for cancelling total walk-off effect. In this configuration, the nonlinear effective coefficient keeps the same. In contrast, for the second configuration, the walk-off correction is achieved by rotating the *z*-axis of second KTP crystal, resulting in reversing its nonlinear coefficient.

The first bonding way for walk-off correction is quasi-noncritical phase match. Under such scheme, one pair of signal and idler will be coupled out of KTP twins based OPO, this is similar to single bulk KTP based OPO, in which it processes high conversion efficiency and high beam quality. For second scheme, quasi-phase matching is met and two sets of signal and idler beams will be generated, since there is wave vector mismatch for $\Delta k l = \pm\pi$, where l is the thickness of single KTP crystal. The conversion efficiency of the first scheme for walk-off correction is lower than the first one, but benefits from the highly coherent property of the twin signals and idlers beams simultaneously generated from bonded KTP, such two close wavelength signals or idlers can be utilized in THz generation by DFG [14] and polarization-insensitive image restoration [15-17]. We have observed the enhancement of THz power from mixing highly coherent idler beams from AFB-KTP based OPO, compared with that by mixing idler and signal beams from bulk KTP based OPO. The THz power enhancement is attributed to the significant reduction of quantum noise [18]. Broadband and polarization-insensitive image restoration is achieved through phase conjugated beams from nonlinear AFB-KTP composites. The phase conjugation from second order nonlinear composite based on QPM has unique features in clearing up the image blurred by phase distortion and

simulated atmospheric turbulence.

2.1.3 Previous Work on OPO

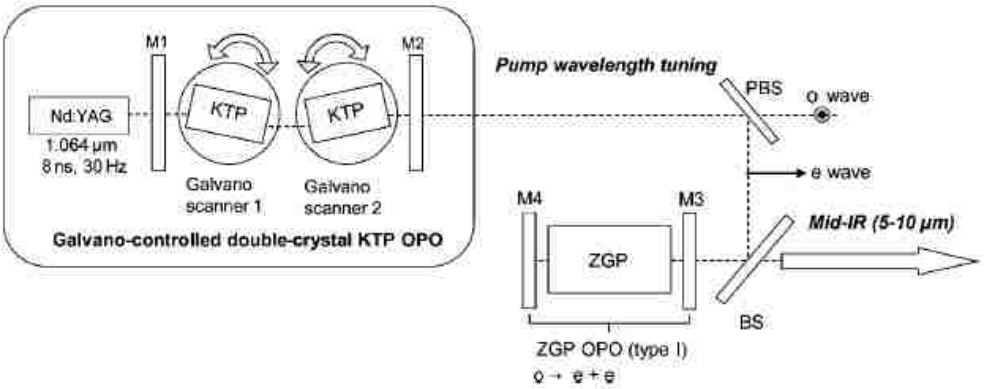

[redacted]

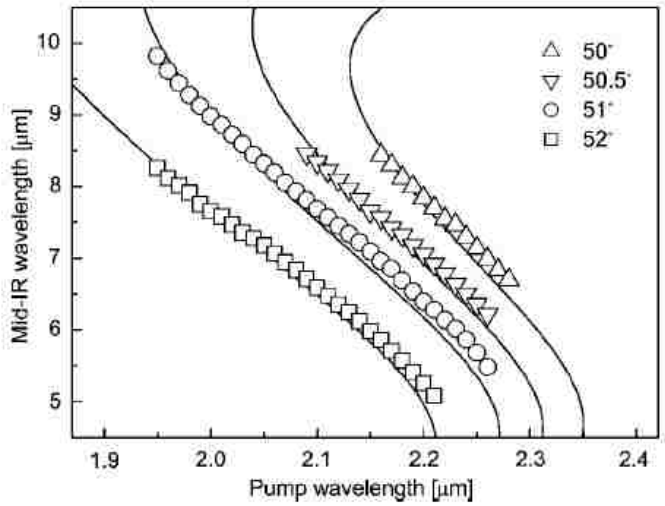

[redacted]

As a specific example of the scheme for KTP twins bonding for QNCPM is introduced. In this literature [19], the researchers demonstrate that tunable mid infrared beams generated from $ZnGeP_2$ pumped by output beam of double KTPs based OPO. In the configuration illustrated in Fig. 2.4, the wavelength of signal and idler can only be tuned through changing the temperature of nonlinear

crystals, since the crystal angle is fixing after being bonded. Different from such configuration, Prof. Ito demonstrated wavelength tunablity of signal and idler through rotating the position of two KTP crystals. The experiment setup is demonstrated in Fig. 2.5. Two identical crystals are placed in OPO cavity with the head to head configuration, so QNCPM is satisfied. KTP crystals are cut at $\theta=53°$ and with a dimension of 10 mm × 10 mm × 10 mm. The KTP OPO is pumped by a Nd:YAG laser operated at 30 Hz. The θ angle of two KTPs can be jumped to a specific value or continuously tuned, so wavelength tunable signal and idler can be got from this type II phase matching OPO. When the angle of KTP is tuned from 47.8 °to 56.5 °, the extraordinary ray is correspondingly tuned from 1.87 μm to 2.4 μm and it is used as pump for ZGP OPO for generation of Mid-IR beam, while ordinary beam is dumped.

Fig. 2.6 demonstrates tunablity of Mid-IR beams from ZGP OPO at four different KTP angles. Through controlling the KTP position, the wavelength of Mid-IR beams can be tuned within 5 μm to 9.8 μm.

In experiment of generation of 1.57 μm beams [20], we demonstrate that eye-safe nearly degenerate signal twins from OPO in inverted KTA twin crystals. Different from the work in Ref. [12], two sets of crystal length of KTA are studied: 15 mm and 23.3 mm. From the quasi-phase matching condition, the separation of signal twins generated from OPO is dedicated by the thickness of KTA crystals. For OPO based on KTA with thickness of 15 mm, the frequency difference corresponds to 117.5 GHz.

In multiple coupled OPO experiment [21], we demonstrate three types of OPO: conventional OPO, AFB-KTP based OPO and AFB-KTP & bulk KTP combined OPO. In multiple coupled OPO, three pairs of idlers are coupled out of cavity, we observe that there are strong coupling effect between

idler beams generated from bulk KTP and two coupled OPOs from AFB-KTP, which is indicated in similar conversion efficiency, slope efficiency and significant reduction in linewidth of two idlers generated from AFB-KTP, compared with that of conventional OPO and AFB-KTP based OPO.

In the last part of this chapter, I will also show our preliminary work on degenerate 2 μm beams generated from KTP stacks OPO.

2.2 Nearly-Degenerate 1.57 μm Signal Twins Generated by OPO in Inverted KTA Crystal Twins

2.2.1 Motivation of Project

In this part, the generation of eye-safe nearly-degenerate 1.57 μm twin signals from twin KTA crystals based OPO is reported. Different from research work on KTP based OPO demonstrated in Ref. [12], instead of using KTP crystal, KTA crystal is adopted for this experiment. As one of isomorphs of KTP crystal, KTA crystal owns similar nonlinear coefficient for frequency conversion [22], and it also has its unique features: (a) KTA crystal has lower absorption in 3.29 μm wavelength region, which will significantly increase the conversion efficiency of 1.57 μm beams; (b) When it is operated at high pump power, it allows minimal thermal induced refractive distortion [23]. In this project, there are only two KTA plates in our setup, in contrast, 20 plates of KTP crystals are used for QPM in Ref. [12]. Furthermore, we designed 15 mm or 23.3 mm crystal length of KTA for generation of idler twins, resulting into narrower frequency separation compared with that from KTP stacks with each slice thickness of 1.19 mm. The wavelength of pairs of idlers and signals is close with each other from 2 μm KTP stacks OPO, while for our KTA crystal OPO, the idlers beams

are at 3.29 μm. Dedicated by quasi phase matching, as the length of KTA crystal increases, the separation of frequency will decrease.

One of important applications of 1.57 μm twin beams from inverted KTA OPO is in carbon dioxide detection. The key consideration of wavelength selection in CO_2 detection is wavelength insensitivity to atmospheric temperature variance and avoidance of overlap with water profile [24]. The passive CO_2 detection by sunlight [25] and active remote sensing approach with OPO [10] or laser source [26] have been developed in the past. The setup for differential absorption Lidar (DIAL) with around 1.6 μm beams [10] is demonstrated in Fig. 2.7, one beam is for on line and the other is for off line, as shown in Fig. 2.8. The backscattered light is collimated by a telescope and the carbon dioxide concentration is determined by measurement of the intensity of backscattered 1.57 μm light by PIN photodiode receiver.

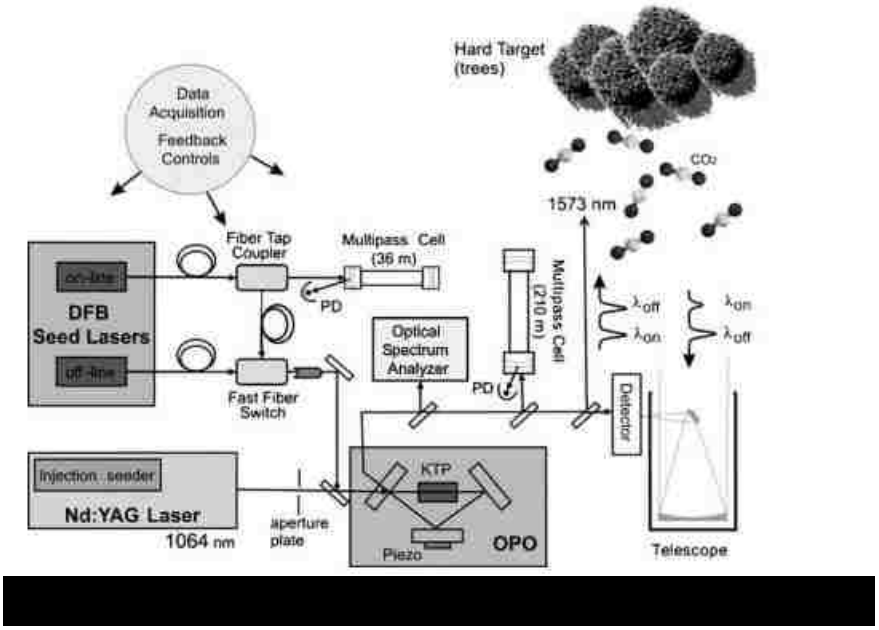

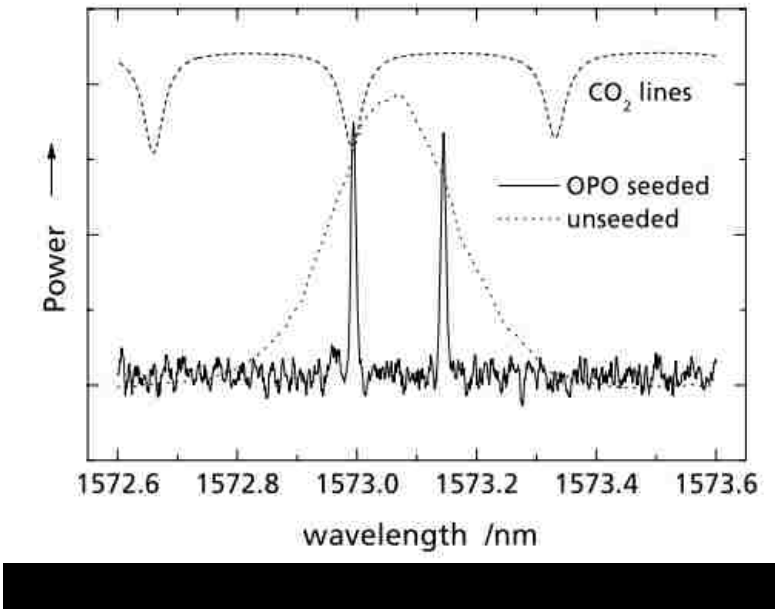

Different from beams with single wavelength from bulk KTP, we can not only collect the information of intensity change in backscattered signals collected by telescope, but we also can measure the phase evolution of signals, so that the signal sensitivity can be dramatically improved with the utilization of nearly degenerate 1.57 μm twin beams. Furthermore, 3.4 μm emitted from OPO can detect the CH_4 concentration, such as on the surface of Mars.

In the past, eye-safe 1.57 μm beams generated from extracavity KTA OPO [23, 27] and intracavity KTA OPO [28, 29] have been reported. Because in intracavity KTA OPO configuration, beams resonate in OPO with round trips before being coupled out of cavity, its conversion efficiency from optics to optics is higher and threshold is lower, compared with extracavity OPO. However, the later one is easier to be operated. From single KTA crystal OPO, only one signal and one idler are generated from non critical phase matching. In Ref. [30, 31], KTA and KTP have been exploited for THz parametric oscillation. In their configurations, it suffers from low conversion efficiency caused by reduced effective lengths. In this experiments, as to our best knowledge, it is the first time the nearly degenerate 1.57 μm beams are generated from inverted twin KTA crystals extracavity OPO.

In this session, we theoretically and experimentally exploited OPO based on crystal twins for generation of signal twins. We first demonstrate our rigorous calculation in oscillation condition and threshold behavior for singly resonant OPO. Our analysis shows that frequency separation of signal twins is inversely proportional to thickness of crystal. In comparison of bulk, AFB composites and crystal twins, the gain for twin crystals is larger than that of AFB composites and it can approach to that of bulk materials. Different from a pair of signal and idler generated from bulk materials, the frequency difference of signal twins keeps constant even there is change in pump wavelength and temperature fluctuation of crystal. Instead of using 16 or 20 plates in Ref. [12], we only adopted two nonlinear crystals for QPM, accumulation of wave vector mismatch can be significantly reduced for OPO based on twin crystals. We experimentally measure the frequency difference of signal twins generated from OPO based on KTA crystals with crystal thickness of 15 mm, and it is determined to be 117.9 GHz.

2.2.2 Theoretical Study of Threshold Behavior

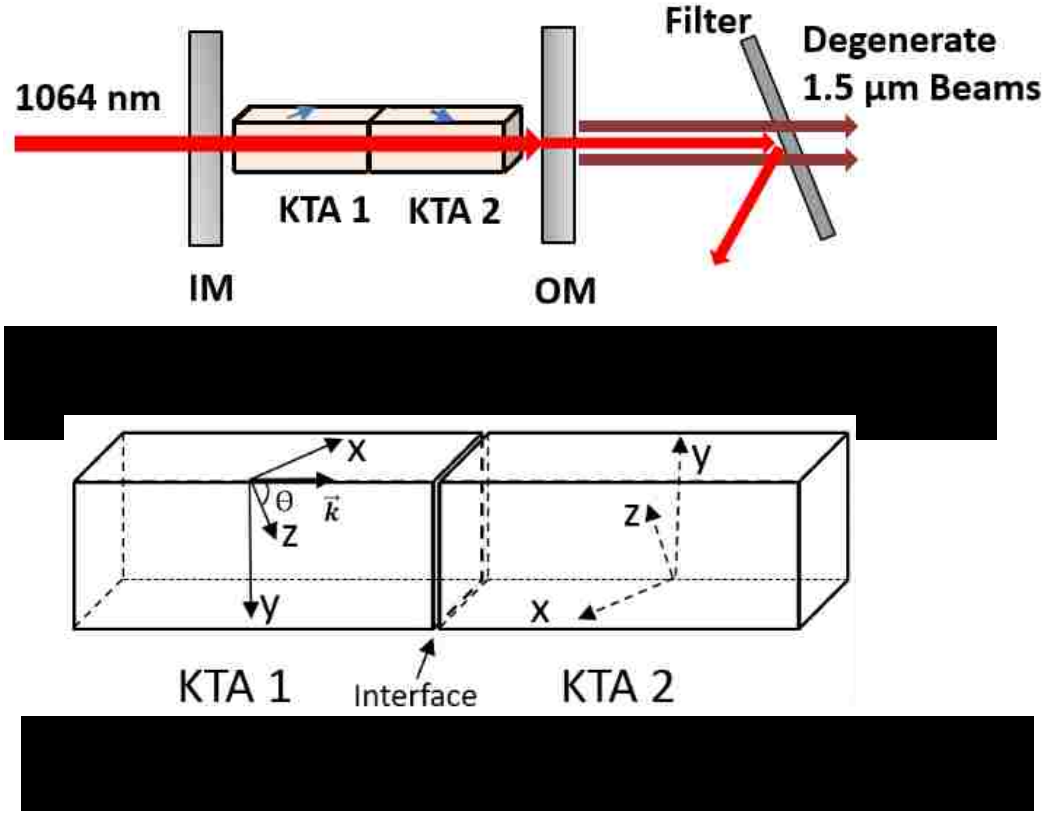

Fig. 2.9 and 2.10 show configuration of OPO based on nonlinear crystal twins, crystal twins are bonded with opposite sign of nonlinear coefficient. Consider electric fields of pump, signals and idlers waves in the forms:

$$E_i = A_i e^{i(w_i t - k_i z_i)} \qquad (3)$$

Where A_i is electric field amplitude of pump, signal and idler waves for $\mathrm{i} = \mathrm{p}, \mathrm{s}, \mathrm{i}$.

Following Ref. [2], A_i can be expressed in the following:

$$A_s(z)e^{i\left(\frac{\Delta k}{2}\right)z} = A_s(0)\left[\cosh(\mathrm{b}z) - \mathrm{i}\frac{\Delta k}{2\mathrm{b}}\sinh(\mathrm{b}z)\right] - \mathrm{i}(\frac{\mathrm{g}}{2\mathrm{b}})A_s^*(0)\sinh(bz) \qquad (4)$$

$$A_i^*(z)e^{-i\left(\frac{\Delta k}{2}\right)z} = A_i^*(0)\left[\cosh(\mathrm{b}z) + \mathrm{i}\frac{\Delta k}{2\mathrm{b}}\sinh(\mathrm{b}z)\right] + \mathrm{i}(\frac{\mathrm{g}}{2\mathrm{b}})A_i(0)\sinh(bz) \qquad (5)$$

Where g is the parametric gain, and b is defined as:

$$\mathrm{b} = \frac{1}{2}\sqrt{g^2 - (\Delta k)^2} \qquad (6)$$

We denote *l* to be thickness of each crystal, through using the quasi-matching condition: $\Delta k = \pm\frac{\pi}{l}$, and assuming the gain is small enough, $gl < \pi$, one can simplify Eqs. (4) and (5) to be:

$$\begin{pmatrix} A_{s1,s2}(l) \\ A^*_{i1,i2}(l) \end{pmatrix} =$$

$$\begin{pmatrix} e^{\mp i\frac{\pi}{2}}[\cos\frac{\pi}{2}\sqrt{1-\left(\frac{gl}{\pi}\right)^2} \pm i\frac{1}{\sqrt{1-\left(\frac{gl}{\pi}\right)^2}}\sin\frac{\pi}{2}\sqrt{1-\left(\frac{gl}{\pi}\right)^2}] & -ie^{\mp i\frac{\pi}{2}}\frac{\sin\frac{\pi}{2}\sqrt{1-\left(\frac{gl}{\pi}\right)^2}}{\sqrt{1-\left(\frac{gl}{\pi}\right)^2}}\left(\frac{gl}{\pi}\right) \\ ie^{\mp i\frac{\pi}{2}}\frac{\sin\frac{\pi}{2}\sqrt{1-\left(\frac{gl}{\pi}\right)^2}}{\sqrt{1-\left(\frac{gl}{\pi}\right)^2}}\left(\frac{gl}{\pi}\right) & e^{\mp i\frac{\pi}{2}}[\cos\frac{\pi}{2}\sqrt{1-\left(\frac{gl}{\pi}\right)^2} \pm i\frac{1}{\sqrt{1-\left(\frac{gl}{\pi}\right)^2}}\sin\frac{\pi}{2}\sqrt{1-\left(\frac{gl}{\pi}\right)^2}] \end{pmatrix}$$

$$\times \begin{pmatrix} A_{s1,s2}(0) \\ A^*_{i1,i2}(0) \end{pmatrix} \qquad (7)$$

The equations above relate electric field amplitude of the outputs to the inputs, under the condition of small gain, $gl \ll \pi$, we can simplify the matrix in Eq. (7) to be:

$$\begin{pmatrix} \mp i\frac{\pi}{4}\left(\frac{gl}{\pi}\right)^2 - \left[1+\frac{1}{2}\left(\frac{gl}{\pi}\right)^2\right] & \mp i\frac{gl}{\pi} \\ \mp i\frac{gl}{\pi} & \pm i\frac{\pi}{4}\left(\frac{gl}{\pi}\right)^2 - \left[1+\frac{1}{2}\left(\frac{gl}{\pi}\right)^2\right] \end{pmatrix} \quad (8a)$$

Since the crystal twins are boned with opposite nonlinear coefficient, the sign of g for second nonlinear coefficient should become negative, so its matrix will be:

$$\begin{pmatrix} \mp i\frac{\pi}{4}\left(\frac{gl}{\pi}\right)^2 - \left[1+\frac{1}{2}\left(\frac{gl}{\pi}\right)^2\right] & \pm i\frac{gl}{\pi} \\ \pm i\frac{gl}{\pi} & \pm i\frac{\pi}{4}\left(\frac{gl}{\pi}\right)^2 - \left[1+\frac{1}{2}\left(\frac{gl}{\pi}\right)^2\right] \end{pmatrix} \quad (8b)$$

Therefore, we can obtain the matrix for correlating input amplitude to the output amplitude after the second crystal by multiplying the above matrix and yields following matrix:

$$\begin{pmatrix} 1+2\left(\frac{gl}{\pi}\right)^2 & 0 \\ 0 & 1+2\left(\frac{gl}{\pi}\right)^2 \end{pmatrix} \quad (9)$$

It is worth mentioning that if we do not rotate the second nonlinear crystal, the matrix product will become identity matrix, which means that there is no gain for crystal twins.

From self-consistency condition, we get the condition for the singly oscillation in OPO based on twin nonlinear crystals as the following equation:

$$R_b R_o \left[1+2\left(\frac{gl}{\pi}\right)^2\right] e^{-2ik_1 l_c} = 1 \quad (10)$$

Where $r_1 = \sqrt{R_b R_o}$, and R_b and R_o are the reflectivities of the back reflector and output mirror. Based on Eq. (10), one can obtain $2k_1 lc = 2m\pi$, m is the cavity mode. Threshold for singly resonant OPO based on nonlinear crystal twins yields to be:

$$(I_{th})_{1,2} = \frac{n_p n_{s1,s2} n_{i1,i2} \lambda_{s1,s2} \lambda_{i1,i2} \left(1-\sqrt{R_b R_o}\right)}{16\eta_0 d^2 l^2 \sqrt{R_b R_o}} \quad (11)$$

where η_0 is the vacuum impedance and subscripts 1 and 2 correspond to two pairs of the signal twins and idler twins. For generations of signal twins of λ_{s1} and λ_{s2} at around 1.57 μm with pump at 1.064 μm, consider $d = d_{24} \sin\theta$, d_{24}=2.4 pm/V [6], R_l = 0.99, R_r= 0.75, the threshold for singly

resonant OPO based on crystal twins can be estimated to be 64.0×10^6 W/cm^2.

One of the major advantages of OPO based on crystal twins is the capability of simultaneously generating twin signals and twin idlers. Eq. (1) can be re-written in terms of the wavelengths and indices of the parametric waves participating in the interaction:

$$n_p(w_p)\frac{w_p}{c} - n_i(w_{i,\pm})\frac{w_{i\pm}}{c} - n_s(w_{s,\pm})\frac{w_{s,\pm}}{c} = \pm\frac{2\pi}{2l} \qquad (12)$$

The plus and minus signs in Eq. (12) correspond to the signal twins and idler twins. In the conventional QPM, only plus sign can be used to satisfy the phase mathcing condition, and therefore, only one signal is generated. The three wavelengths are also related to one another through energy conservation, as shown in Eq. (2).

According to Eq. (12), as the length of each domain is increased, the wave vector mismatch, required to satisfy Eq. (12), is reduced, and therefore, the frequency separation is decreased. Indeed, for efficient OPO, the QPM condition must be satisfied. Through deriving the Eq. (12), we expand the refractive index at the first order of Taylor expansion around the refractive index of signal and idler generated from bulk nonlinear crystal. One can obtain the frequency separation of the twin signals and twin idlers as:

$$\Delta\nu \approx \frac{c}{(n_{g,s}-n_{g,i})*l} \qquad (13)$$

Where $n_{g,s}$ and $n_{g,i}$ are the group indices of refraction for the signal and idler waves generated by a single crystal. From Eq. (13), we can know that frequency difference is inversely proportional to the crystal length. The plot of $\Delta\nu$ versus crystal thickness is shown in Fig. 2.11. For $l \approx 15$mm, one can determine $\Delta\nu$ to be 198.95 GHz. At this frequency region, GHz waves can be generated by mixing signal twins in heterodyning [32]. As shown in Fig. 2.11, by significantly increasing the length of each KTA domain, the frequency separation of the signal twins is reduced from ~3 THz to

~100 GHz, by a factor of around 30.

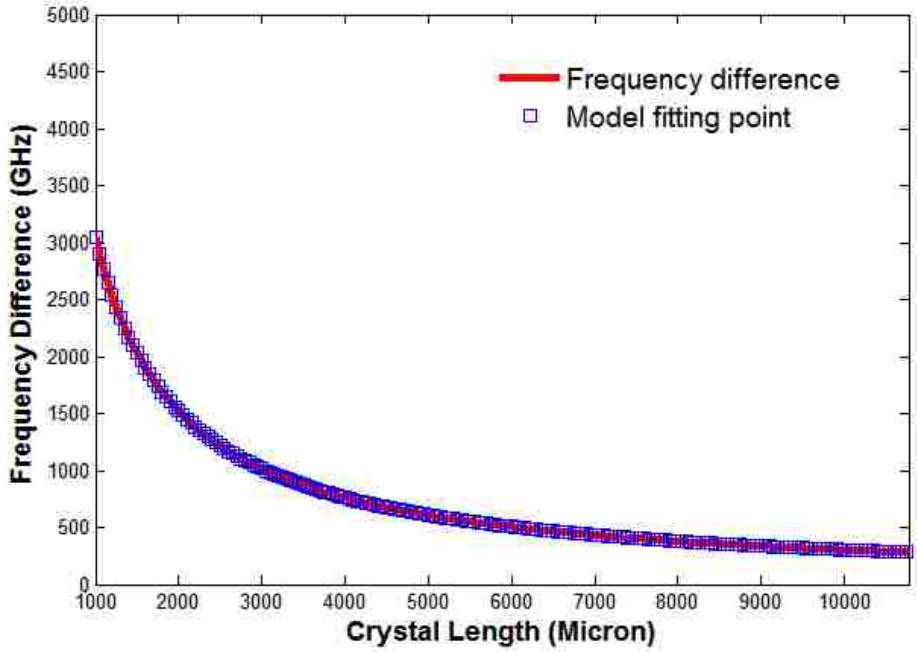

Normalized output power as a function of crystal length for bulk, AFB composites and crystal twins is shown in Fig. 2.12. For birefringence condition for bulk KTA, it displays quadratic dependence. The modulation pattern for AFB composites with multiple layers, due to the periodically switching nonlinear coefficient sign, it evolves as ripples around quadric dependence. In contrast, the diagram for twin crystals is close to be connected by two quarter cycles.

As we know in the above discussion, even there is a mismatch in twin crystals, it will only grow a little bit during signal and idler resonance, while for AFB composites, the mismatch will be accumulated very quickly, since there are many layers in AFB composites. Here we would like to consider the effect of error in accuracy of crystal length on phase term, from $\Delta k = \pm\frac{\pi}{l}$, we can get $\pm\frac{\delta\varphi}{\pi} = \pm\frac{\Delta l}{l}$. Compared with each layer thickness for AFB composites, it is more than ten times larger for our twin crystals, as a result, twin crystals has a much better tolerance in crystal

length variation error in manufacturing. Another advantage for twin crystals in comparison with AFB composites lies in that: for $g < \frac{\pi}{l}$, twin crystals has larger gain; For $g > \frac{\pi}{l}$, our conversion efficiency $\frac{gl}{\pi}$ is larger. What is more, when $g \gg \frac{\pi}{l}$, the conversion efficiency of twin crystals $\sqrt{(\frac{gl}{\pi})^2 - (\Delta k)^2}$ will approach that of bulk materials, since Δk will play no role in amplification. Specifically, for the AFB with crystal thickness of around 1 mm, it nearly displays no gain. In contrast, the gain for crystal twins is around 15 cm^{-1}, it is large enough for amplification.

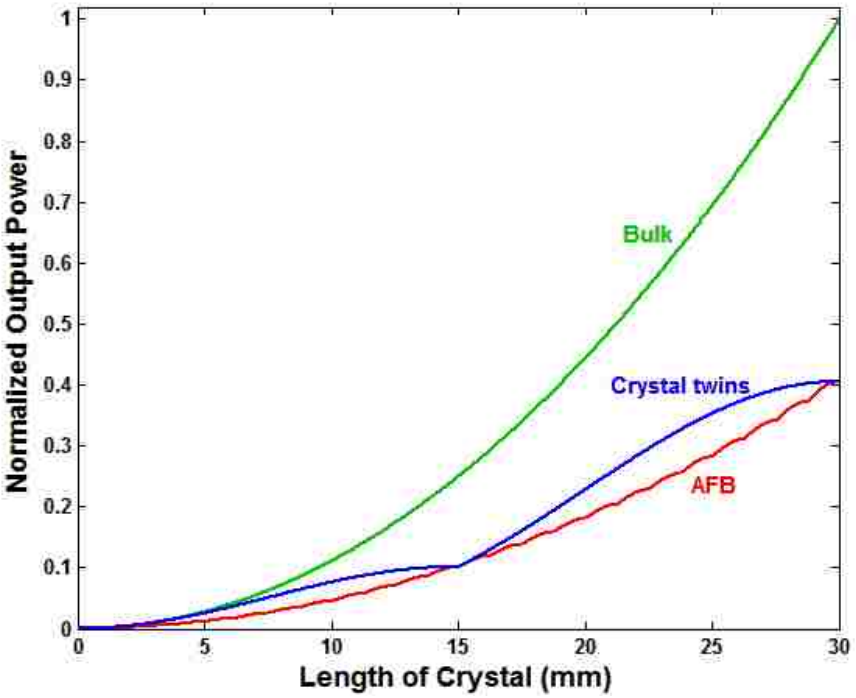

2.2.3 Ultrastable Properties of Signal Twins

As we have discussed earlier, the pair of signal twins should demonstrate highly coherent property. In order to illustrate the advantage of signal twins from KTA twins OPO, another OPO based on bulk KTP is introduced. The wavelength of output signals versus pump wavelength is shown in Fig. 2.13, when OPO is pumped at 770 nm. At around 52.6 °cut angle, degenerate signals and idlers with frequency difference of ~120 GHz are generated. We study the wavelengths tuning of signal twins

from twin KTAs with crystal cut angle of 78.2 °and signal and idler from single KTA with 52.6 °cut angle as a function of pump wavelength [Fig. 2.14] and crystal temperature [Fig. 2.15]. For twin signals at 1.5 μm, as illustrated in Fig. 2.14(a), on one hand, when we tunes the pump wavelength, the frequency difference of output beams keeps constant, on the other hand, for conventional OPO based on single KTA, it changes a lot. We determine that the frequency difference for signal twins is a factor of 700 less insensitive in comparison with that of convention OPO, which means that we can scan the wavelength of 1.5 μm output beams through tuning pump beams and at the same time keep frequency difference to be a constant. Within the pump range from 1.042 μm to 1.082 μm, the frequency difference of signal twins is around 120 GHz to 130 GHz. For conventional OPO based on bulk KTA, the degenerate point is designed for being available at pump 770 nm. ~100 GHz waves can only be generated within very narrow pump wavelength range, as demonstrated in Fig. 2.14(b). Furthermore, if there is temperature fluctuation in twin KTA crystals, as shown in Fig. 2.15(a), the frequency difference is nearly a constant. For conventional OPO based on single KTA, at room temperature, the frequency difference of idler and signal corresponds to 126.7 GHz, and it will fluctuate as the temperature of crystal changes. Compared with signal and idler from single KTA, signal twins demonstrate a factor of less 130 insensitive in temperature fluctuation. The ultrastable characteristics of signal twins can be explained by Eq. (13), because the frequency difference is determined by the difference of group indices of signal and idler, and the group velocity dispersion caused by pump wavelength change and temperature fluctuation of crystal will not change the frequency difference. As a result, the frequency difference will be insensitive to change of pump wavelength and temperature fluctuation of crystal. In conclusion, the frequency difference of signal twins is insensitive to pump wavelength tuning and temperature fluctuation of KTA crystal,

these two features make signal twins beams to be ideal source for image restoration and low quantum noise heterodyning.

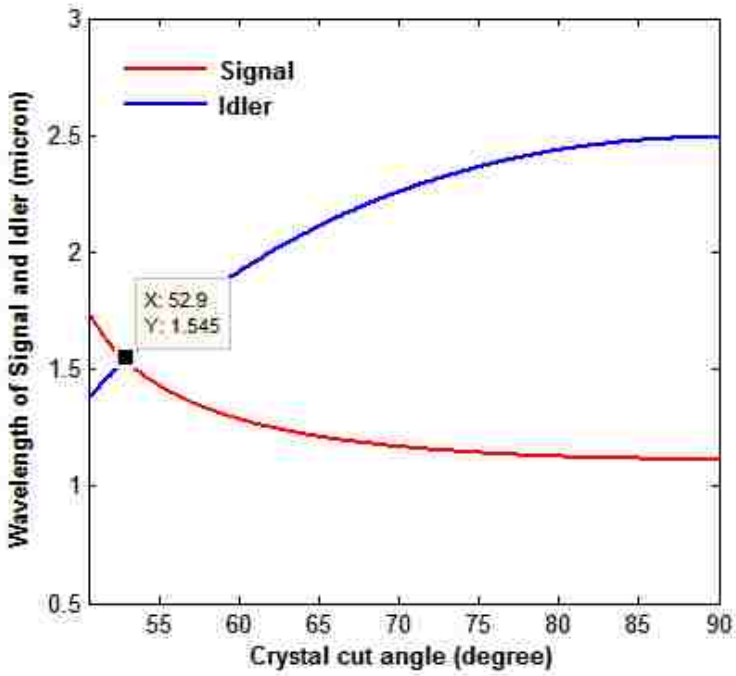

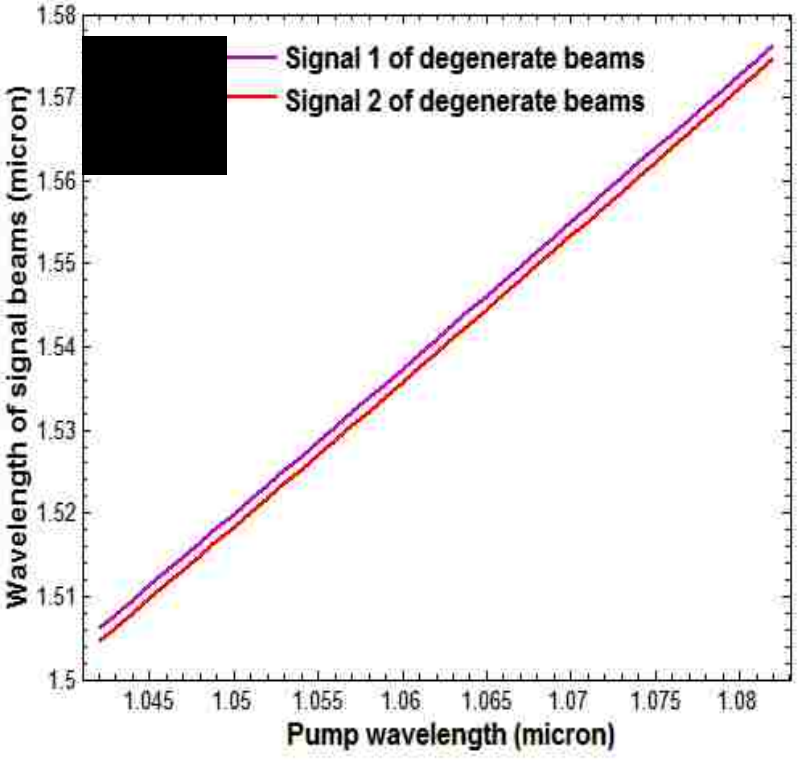

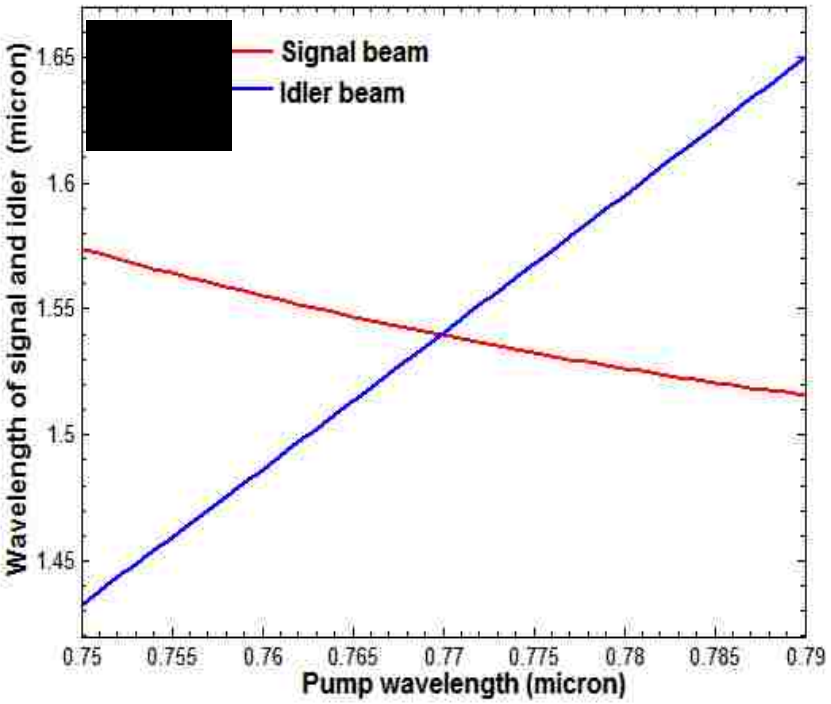
Signal beam
Idler beam
Wavelength of signal and idler (micron)
1.65
1.6
1.55
1.5
1.45
0.75
0.755
0.76
0.765
0.77
0.775
0.78
0.785
0.79
Pump wavelength (micron)

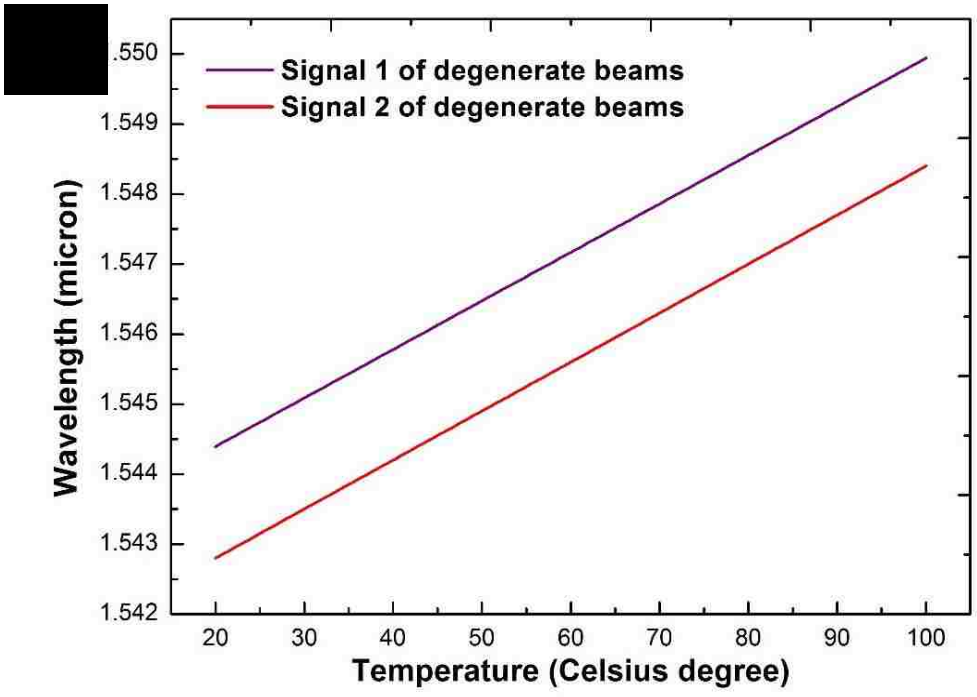
Signal 1 of degenerate beams
Signal 2 of degenerate beams
Wavelength (micron)
1.550
1.549
1.548
1.547
1.546
1.545
1.544
1.543
1.542
20
30
40
50
60
70
80
90
100
Temperature (Celsius degree)

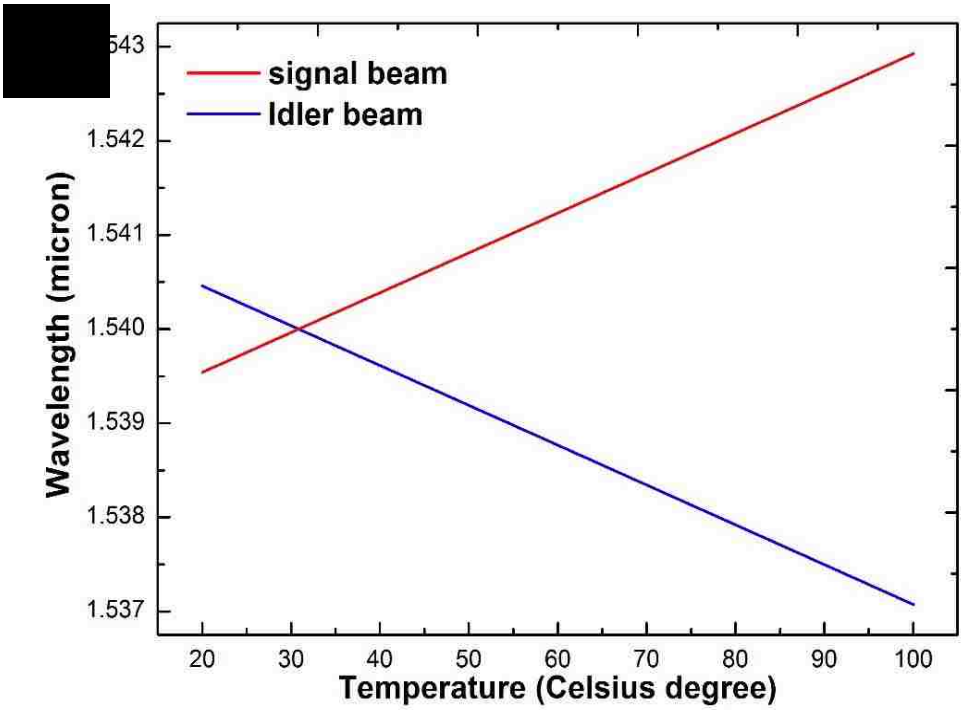

Fig. 2.15. Wavelengths of (a) signal twins generated from KTA twins with crystal cut angle of 78.2 °and (b) signal and idler generated from single KTA crystal with cut angle of 52.6 °as a function of KTA crystal temperature.

2.2.4 Experimental Setup

In order to examine our theory, we have conducted an experiment for generation of 1.57 μm signal twins based on KTA crystal twins. Fig. 2.9 and 2.10 demonstrate the experimental setup of twin KTAs based OPO for generation of nearly degenerate 1.57 μm twin signals. KTA crystals used in this experiments is cut at θ=78.2 °, φ=0 °, and both sides of facets are coated for high transmission at 1.534 μm for singly resonance. There are two different sets of crystal lengths for our study: 15 mm and 23.3 mm. The laser source is a Nd: YAG high power laser with 10 Hz repetition rate and 10 ns pulse duration width, and the wavelength is 1.064 μm. The compact singly resonant OPO consists of backreflector (input mirror) and output mirror. The pump input side of backreflector is coated with high transmission at 1.064 μm and the cavity side of backreflector is coated HR at 1.534

μm and HT at 1.064 μm. For output mirror, the cavity side has a reflectivity of 70% ±3% at 1534 nm, and the output side is coated at high transmission at 1.534 μm.

2.2.5 Experimental Results and Discussions

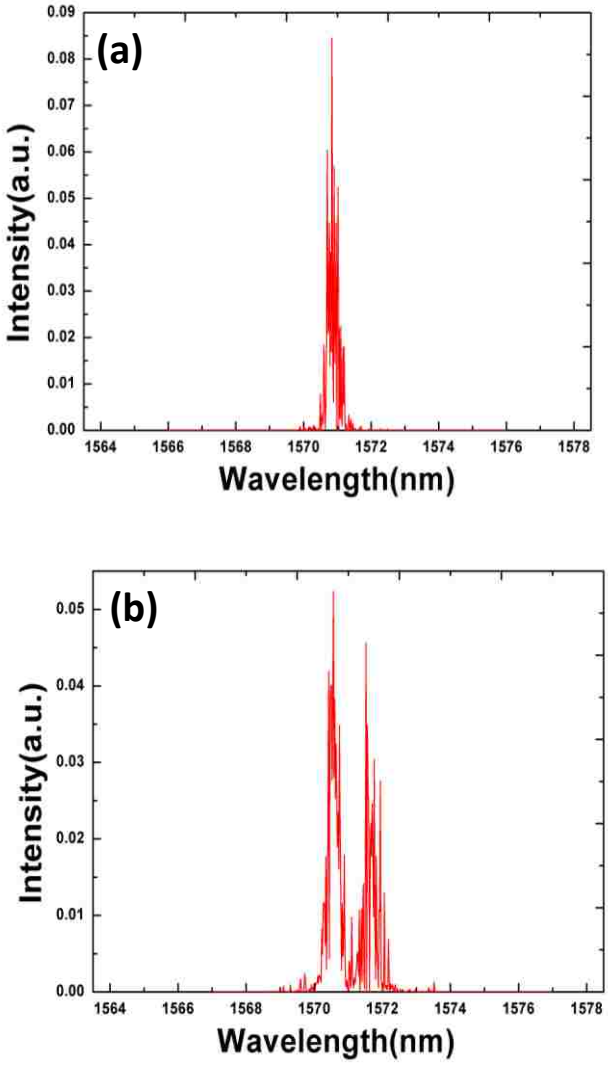

Fig. 2.16. Spectra of signal(s) generated from singly resonant 15 mm KTA crystal(s) based OPO with (a) single crystal, (b) twin crystals.

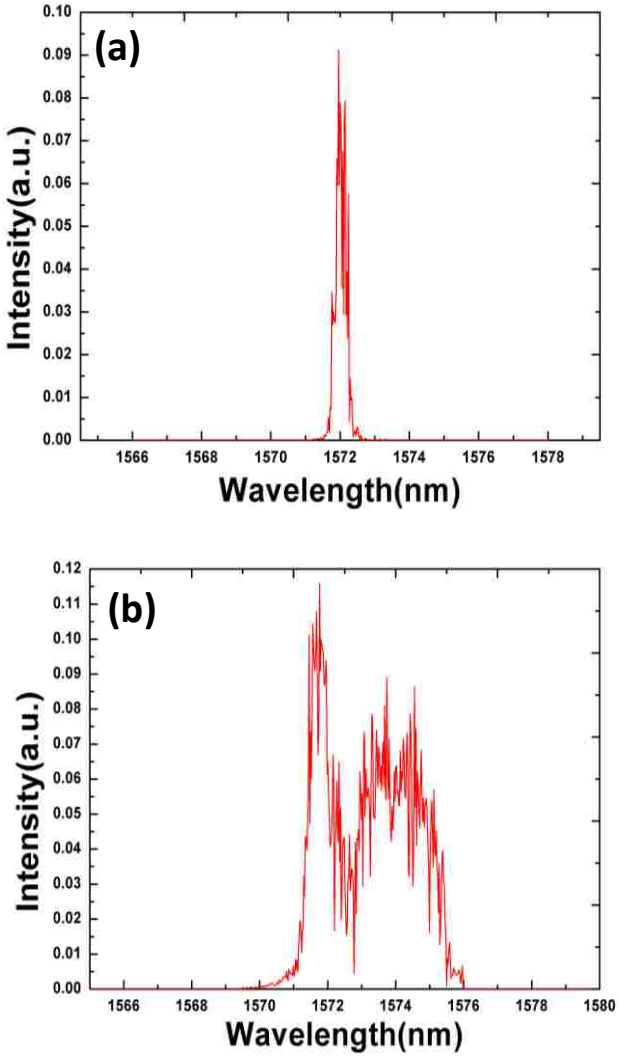

Fig. 2.17. Spectra of signal(s) generated from singly resonant 23.3 mm KTA crystal(s) based OPO with (a) single crystal, (b) twin crystals.

Fig. 2.16 and Fig. 2.17 show the spectra of signal(s) generated from KTA based OPOs with crystal length of 15 mm and 23.3 mm, respectively. The wavelength and linewidth of signal from single 15 mm KTA based OPO is measured to be 1570.84 nm and 0.3 nm, as shown in Fig. 2.16(a), while for

singly resonant twin KTAs based OPO, the signal is split into nearly degenerate pair with wavelength of 1570.36 nm and 1571.33 nm, and the linewidth is 0.38 nm and 0.32 nm, respectively [Fig. 2.16(b)]. Such pair of signals owes much lower quantum noise for difference frequency generation from our theoretical analysis in [18], which makes it to be ideal source for heterodyning in photodiode [32]. In Fig. 2.17(a), it demonstrates that the wavelength and linewidth of signal from single KTA crystal OPO is 1572.95 nm and 0.38 nm, the wavelength is slight different from the one of 15 mm KTA based OPO, which should come from the crystal cut accuracy in manufacturing. As shown in Fig. 2.17(b), the linewidth of signal at 1571.69 nm is measured to be 0.8 nm and the one at 1573.95 nm is measured to 1.74 nm. The broadening in linewidth at 1573.95 nm is observed, this would be caused by absorption at 3.3 μm in OPO cavity. There are two competitive factors for narrowing linewidth: gain and absorption. For twin 15 mm KTAs based OPO, the gain is much larger than the absorption for 1571 nm.

First Stoke Raman has been observed from KTA OPO [33], and in our experimental setup, it is expected to be available in output beams and if we used periodically poled KTA, Stoke Raman signals can be enhanced by strongly coupling of idler beams and vibration [34].

The dependence of output power on pump power is studied, as shown in Fig. 2.18. The threshold of single 15 mm KTA based OPO is measured to be 25 mJ, and when twin KTA crystals is placed into the cavity, the threshold is decreased to be 21.05 mJ, and their slope efficiencies are 10.91% and 11.27%, respectively. When the crystal length increases to 23.3 mm, the threshold for single KTA based OPO is further reduced to 17 mJ, and the one for twin KTA crystals based OPO is determined to be 10.22 mJ. At the same time, their corresponding slope efficiencies increase to be 17.93% and 18.09%, respectively. The reduction in threshold and increase of slope efficiency are caused by the

increase of parametric gain for KTA crystal with longer crystal length. For 23.3 mm twin KTA crystals, the signal output pulse energy is measured to be 6.61 mJ with 45.2 mJ of 1.064 μm pump energy, which corresponds to 14.62% conversion efficiency.

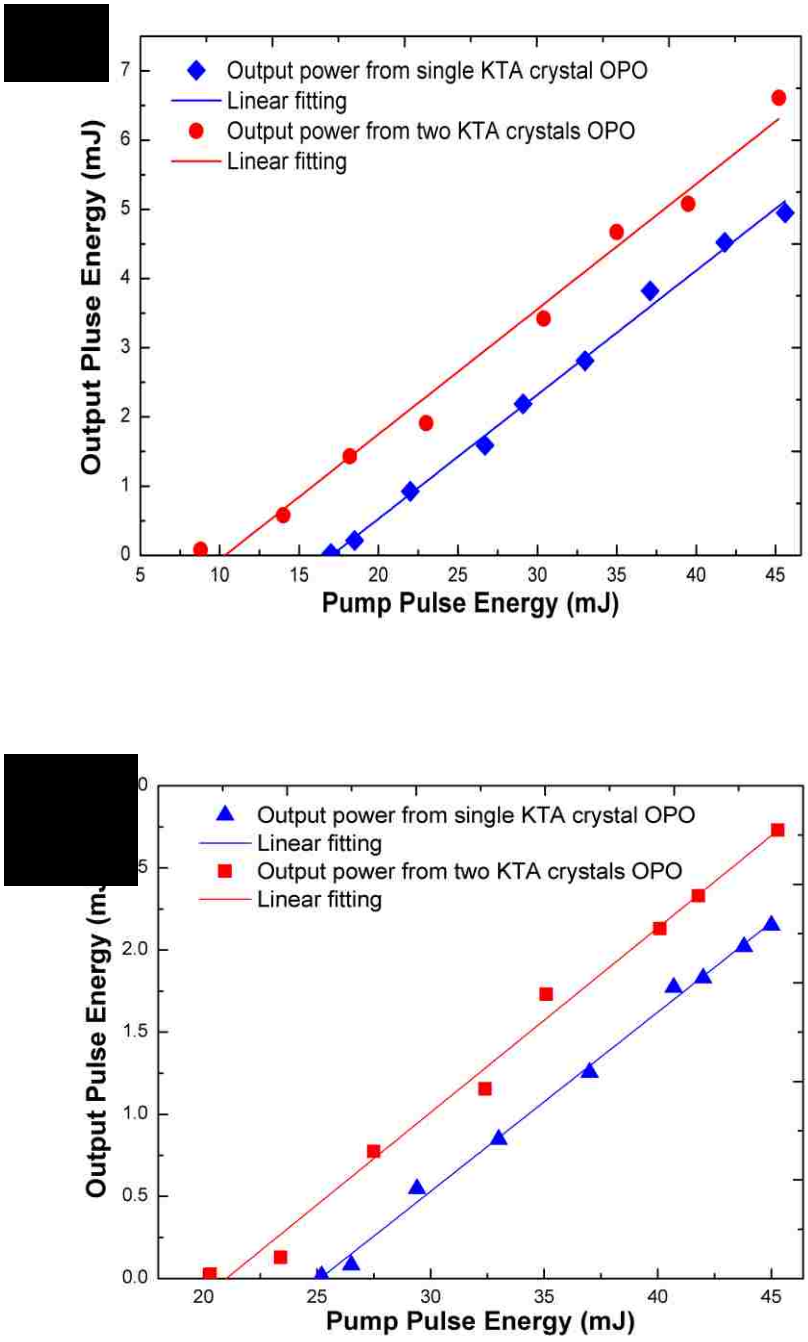

Fig. 2.18. Output pulse energy of signal beam(s) from (a) 15 mm (b) 23.3 mm single KTA based OPO and twin KTA crystals based OPO as function of pump pulse energy.

2.3 Multiple 1 μm Degenerate Idler Beams from KTP OPOs

2.3.1 Introduction to Generation of Multiple 1 μm Degenerate Idler Beams

As one of important nonlinear crystals, KTP has been utilized in OPO within wavelength range from 350 nm to 4.5 μm [35]. Compared with lithium niobate, it has advantages in some applications, since it does not have photorefractive effects. For conventional OPO based on single KTP crystal, phase matching condition is fulfilled by birefringence for pump and one set of idler and signal. THz wave generation has been demonstrated through mixing this pair of signal and idler [36]. But such scheme suffers one drawback—the THz frequency which corresponds to the frequency difference of idler and signal beams is subjected to crystal orientation, pump wavelength and temperature of crystal. As a result, it has limitations in THz waves, millimeter and micrometer wave generation. Usually a pair of KTP crystals are introduced for overcoming this drawback [37]. Through controlling the orientations of the two crystals, the wavelengths of two idlers can be tuned.

2.3.2 Experimental Setup and Discussions

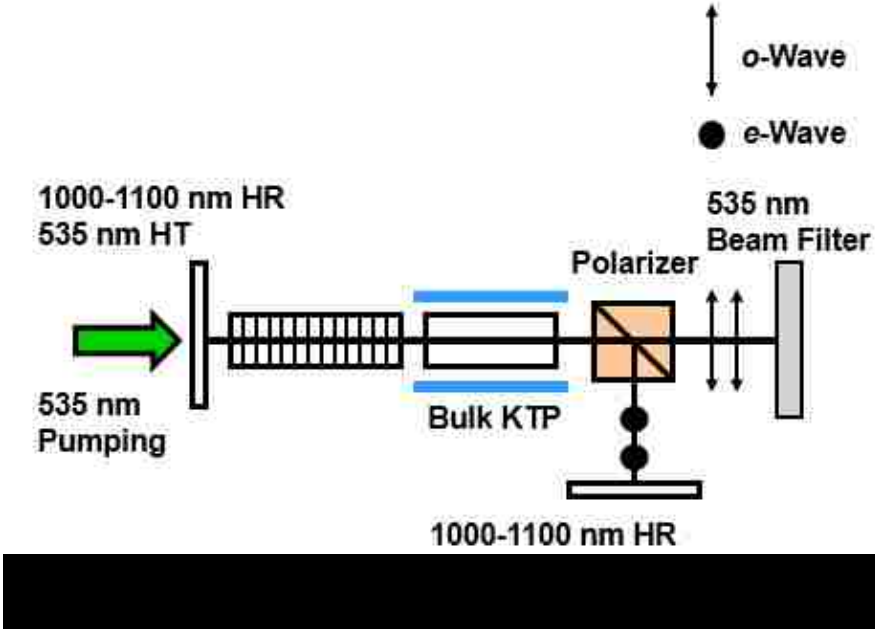

Fig. 2.19 illustrates the experimental setup for generating 1 μm multi-wavelength idlers from KTP OPO cavity. The OPO cavity consists of an input mirror and output mirror, both of them reach high reflectivity for 1000-1100 nm and input mirror is coated with high transmission at 535 nm for pump beam. A cubic polarizer is inserted into OPO cavity for realizing singly resonance of signal beams, and such singly resonant OPO is more stable than doubly resonant one for multi-wavelength beams generation. In this experimental design, only idler beams is efficiently coupled out of OPO cavity. One bulk KTP and one AFB-KTP composites are adopted in our study. Bulk KTP is cut along *x*-axis, and have a dimension of 5 mm ×5 mm ×20 mm, and AFB-KTP composites are made up of 20 slices of *x*-cut KTP with thickness of 1.19 mm, in which *z* axes of KTP slices are periodically switched, 20 layers of KTP are bonded by adhesive-free technique with low interface absorption. One pair of signal and idler are generated from bulk KTP through birefringence phase matching condition. In contrast, two sets of signals and idlers are generated by quasi-phase matching condition.

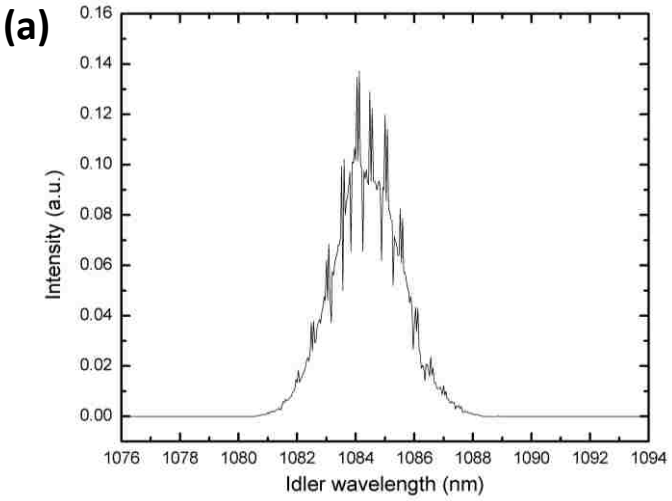

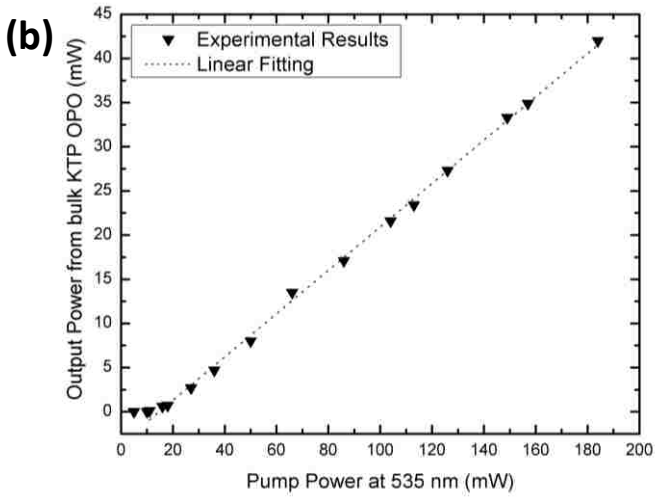

Fig. 2.20. (a) Spectra and (b) measured output power for bulk KTP OPO.

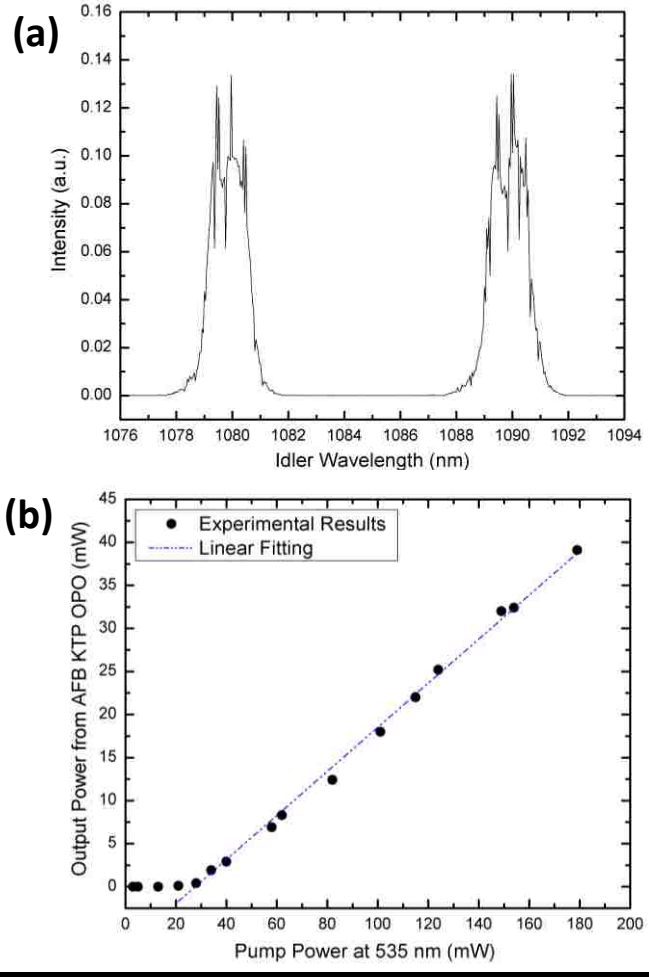

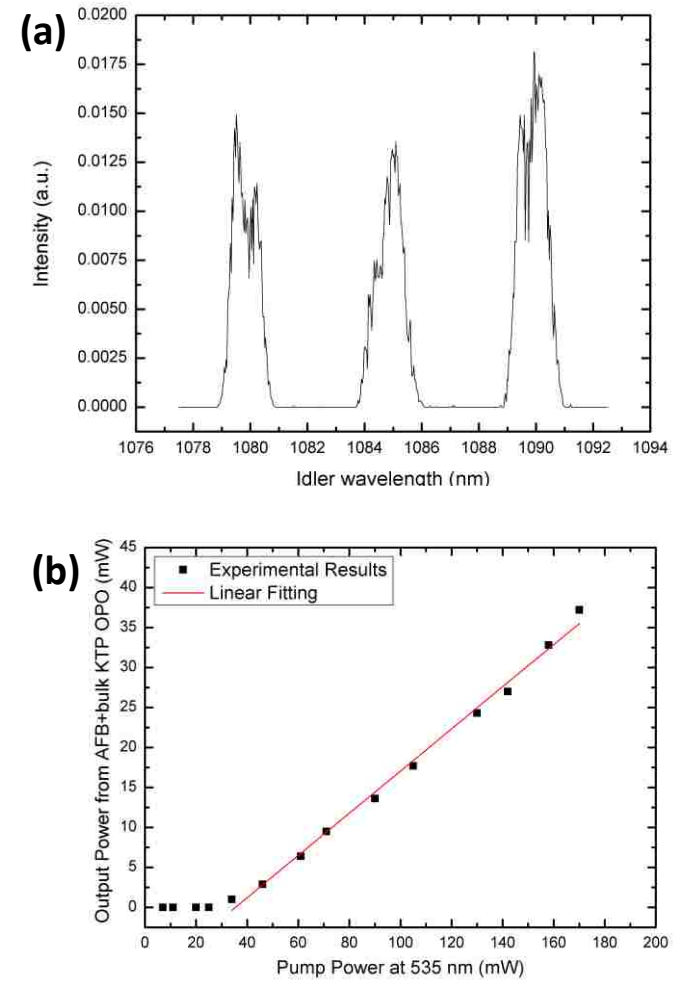

[redacted]

Three types of OPOs are studied for the coupling effect of idler beams generated: traditional bulk KTP based OPO, AFB-KTP based OPO and joint bulk KTP and AFB-KTP OPO (denoted as BA KTP OPO), the linewidth and output power from each OPO cavity are carefully measured. As shown in Fig. 2.20, only one idler beam is measured and its linewidth is 2.158 nm, and threshold of bulk KTP based OPO is determined to 14.74 mW. For AFB-KTP OPO, the linewidths of idler beams generated are around 1.402 nm and threshold is measured to be 27.64 mW [Fig. 2.21]. The linewidths generated from AFB-KTP composites and bulk KTP are measured to be 1.079 nm, 1.025

nm and 1.033 nm respectively, and threshold is measured to be 35.32 mW for BA KTP OPO [Fig. 2.22]. From linear fitting of output power from each KTP OPO, the slope efficiencies are determined to be 24.54%, 25.60% and 26.36%, respectively. This shows that the conversion efficiency is nearly the same for these three types of OPO, and generation of additional idler from bulk KTP does not decrease the overall conversion and slope efficiency. The linewidth of idler from bulk KTP OPO is broadest and it becomes narrower in BA OPO cavity. At the same time, the linewidth of idlers generated from AFB-KTP also becomes narrower. The narrowing linewidth effect is similar to the function of nonlinear filter.

The above experiment shows that for AFB-KTP OPO, the insertion of bulk KTP plays the role of nonlinear medium and gain, what is more, the presence of idler generated from bulk KTP causes phase mismatching. Similarly, for bulk KTP OPO, the presence of AFB-KTP plays the role of gain, and at the same time it causes phase mismatching for the output beams of BA KTP OPO. The mutual gain role indicates that there is strong coupling effect between idler twins beams generated from AFB-KTP and idler from bulk KTP crystal. Such strong coupling effect not only results into narrowing linewidth in BA KTP OPO, but also maintaining the conversion efficiency and slope efficiency. Such configuration with strong coupling effect can be utilized in quantum communication.

2.4 Doubly-Resonant OPO for Generation of Multi-Degenerate 2 μm Beams

2.4.1 Introduction to Generation of Multi-Degenerate 2 μm Beams

The 2 μm to 5 μm mid-infrared region has overtone vibrational absorption lines of atmospheric

content and gas [38], so OPO radiation within this wavelength region can be used in detection of chemical gas. In contrast, 1.57 μm or 1 μm introduced in session 2.2 and 2.3 will be useless for this purpose, scientists would like to develop OPO with longer wavelength radiation. As an example of various applications, 2 μm radiation from solid state laser, such as Tm, Hm:YLF laser, has been used in wind measurement [39]. However, in traditional methods, only particular one wavelength is generated from solid state laser or conventional OPO. As an improvement, we would like to introduce signal twins or idler twins for chemical sensing. With such novel configuration, the sensitivity will be significantly increased. Furthermore, the quantum conversion efficiency for THz generation by mixing degenerate 2 μm beams is higher than that by mixing 1 μm beams, so signal twins will provide another important source for DFG THz generation.

In this part, I will introduce our preliminary work on generation of degenerate 2 μm beams, which will be the first step for my study in chemical sensing and THz generation.

2.4.2 Experimental Setup and Discussion

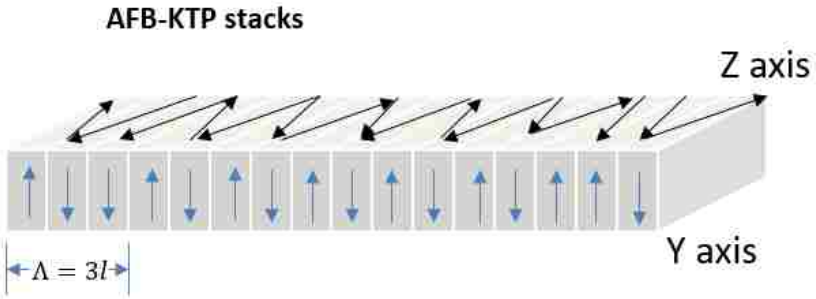

Fig. 2.23. Demonstration of KTP stacks with three grating layers for quasi phase matching. KTP layer at the right end side is a spare layer for walk-off correction.

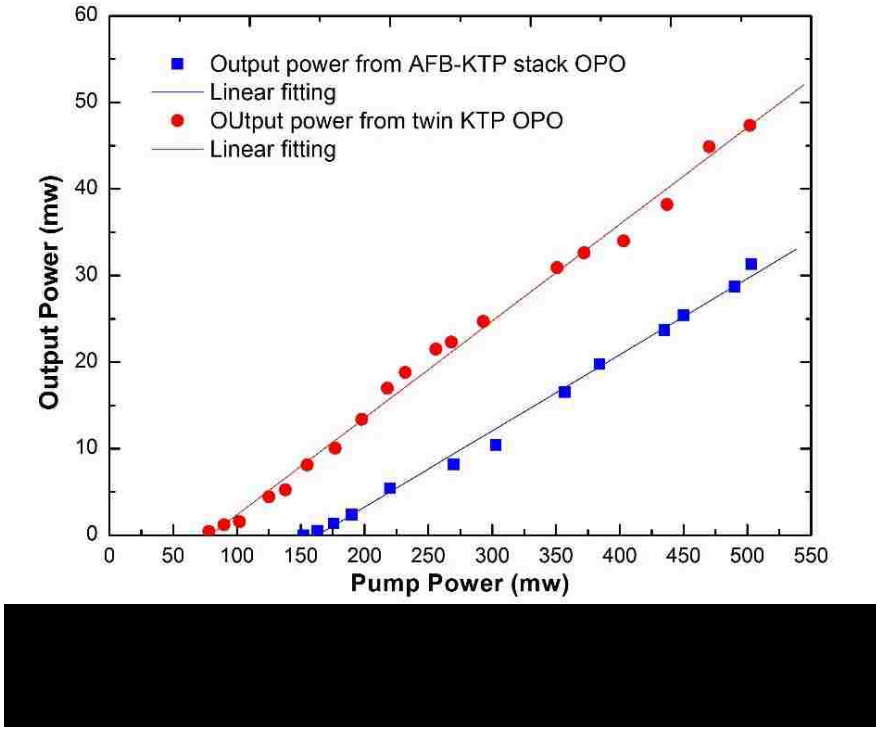

The laser source used in this experiment is the high power Nd: YAG laser with repetition rate of 10 Hz and pulse duration of 10 ns. Fig. 2.23 depicts that scheme of crystal stacks for reaching quasi phase matching condition. In order to compensate walk-off effect in KTP crystal, the KTP plates are bonded in *z* axis with head to tail configuration, resulting into the periodically switched nonlinear effective coefficient. The walk-off compensated KTP composite is made of 16 plates KTP stacks and the thickness of each plate is 2 mm. Both facets of KTP are coated with high transmission at 1 μm and 2 μm. Different from Ref. [12], we used Plano-Plano OPO cavity design. The KTP plates is cut along crystal direction of θ=50.2 °, φ=0 °for type II phase matching. Walk-off compensation is achieved through the complicatedly switching *z* axis direction, as shown in Fig. 2.23. The KTP stacks are bonded in a way that two opposite d_{eff} layers with one negative d_{eff} layer.

The output power of multi-wavelength signals and idlers from KTP stacks based OPO is measured, as shown in Fig. 2.24. The OPO cavity is consisted of backreflector (input mirror) and output mirror.

The backreflector is coated with high transmission for 1 μm and high reflectivity at 2 μm, while output mirror has 85% ±5% reflectivity at 2 μm and is coated with HT at 1 μm. For KTP stacks based OPO, the threshold is determined to be 163 mW and slope efficiency is 8.8%. And for twin KTPs based OPO, its threshold is 78 mW and slope efficiency is 11.2%. Both of two output power dependence can be linear fitting. For KTP stacks based OPO, output power of 31.2 mW is measured with pump power of 503 mW, corresponding to 6.24% conversion efficiency.

Chapter 3 Image Restoration by Phase Conjugation

3.1 Introduction to Image Restoration

3.1.1 Origin of Phase Conjugation

Since the first observation of optical phase conjugation (OPC) in backward-stimulated Brilliouin scattering in 1972 [40], OPC has been utilized in image restoration [41], modal dispersion in fiber [42], compensation of pulse distortion [43] and holography [44]. In image restoration, phase conjugation generated from nonlinear process is the replica of input beam and it has been utilized in correction of wave front distortion after input beam propagates through phase distortion medium. It has the features of time reversal and wave front reversal. The general mechanism of phase conjugation for image restoration is demonstrated in Fig. 3.1 [45]. Image recovery can't be achieved by conventional mirror in case (a). In contrast, in case (b), the image is recovered by a phase conjugation mirror after original image is distorted by a phase distortion medium.

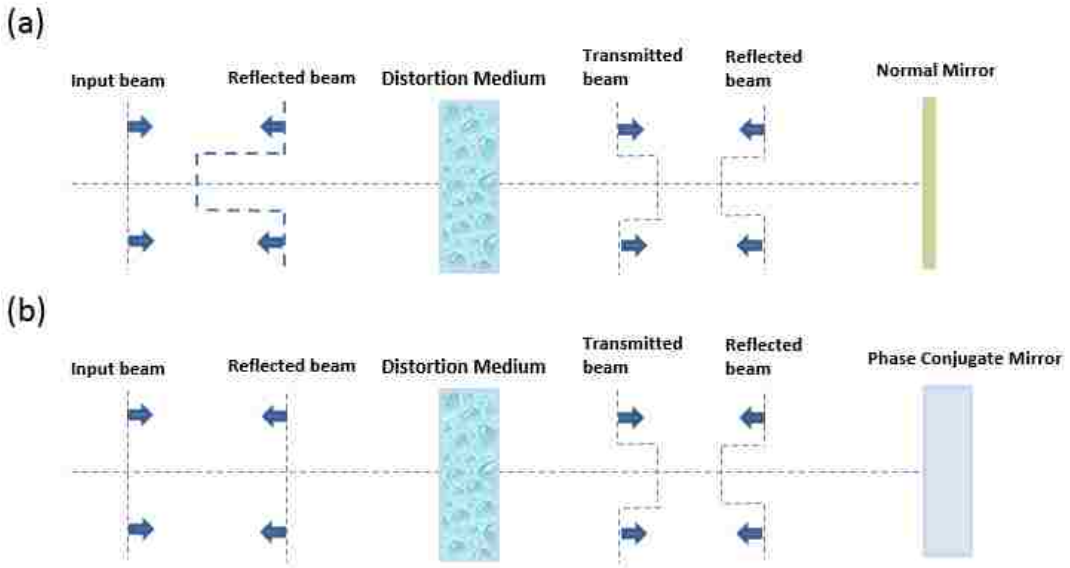

Fig. 3.1. Illustration of principle of phase conjugation mirror in image restoration. (a) A normal mirror is used to reflect input beam; In comparison to (a), phase conjugate mirror is utilized in (b) for image restoration.

The input beam for forming original image can be expressed as a plane wave [45],

$$\mathrm{E}(\mathrm{z},\mathrm{x},\mathrm{y},\mathrm{w}) = A_0(\mathrm{z},\mathrm{x},\mathrm{y})e^{ikz}e^{-iwt} \qquad (1)$$

After it propagates through a distortion medium, a phase distortion is imposed,

$$\mathrm{E}'^{(\mathrm{z},\mathrm{x},\mathrm{y},\mathrm{w})} = A_0(\mathrm{z},\mathrm{x},\mathrm{y})e^{i[kz+\varphi(z,x,y)]}e^{-iwt} \qquad (2)$$

In case (a) of conventional mirror, the reflected beam can be expressed as:

$$\mathrm{E}''(\mathrm{z},\mathrm{x},\mathrm{y},\mathrm{w}) = \mathrm{R} \times A_0(\mathrm{z},\mathrm{x},\mathrm{y})e^{-ikz+i\varphi}e^{-iwt} \qquad (3)$$

And such phase distortion term for reflected beam will accumulate and be doubled to 2φ after it traces back the same beam path of input beam:

$$\mathrm{E}'''(\mathrm{z},\mathrm{x},\mathrm{y},\mathrm{w}) = \mathrm{R} \times \mathrm{T} \times A_0(\mathrm{z},\mathrm{x},\mathrm{y})e^{i[-kz+2\varphi]}e^{-iwt} \qquad (4)$$

Differently, in case (b) of phase conjugation mirror, the sign of phase distortion term for reflected beam becomes opposite:

$$\mathrm{E}''(\mathrm{z},\mathrm{x},\mathrm{y},\mathrm{w}) = \mathrm{R}' \times A_0(\mathrm{z},\mathrm{x},\mathrm{y})e^{i[-kz-\varphi]}e^{-iwt} \qquad (5)$$

So the total phase distortion will be cancelled and phase aberration will be removed. As a result,

image restoration is realized:

$$\mathrm{E}'''(\mathrm{z},\mathrm{x},\mathrm{y},\mathrm{w}) = \mathrm{R}' \times \mathrm{T} \times A_0(\mathrm{z},\mathrm{x},\mathrm{y}) e^{i[-kz-\varphi]} \times e^{i\varphi} e^{-iwt}$$

$$= \mathrm{R}' \times \mathrm{T} \times A_0(\mathrm{z},\mathrm{x},\mathrm{y}) e^{-ikz} \times e^{-iwt} \qquad (6)$$

A specific case of OPC in restoration of wave front is photorefractive effect in turbidity suppression for bio-imaging [46, 47]. The scattering is the key factor in randomizing light path and distorting wave front, such scattering effect is caused by variations in distribution of refractive index in biological tissue. Different from dynamic changing turbid medium, biological turbid material can be treated as stationary object, so temporal response of optical phase conjugation will not play any role in image restoration. Although response speed of photorefractive effect is limited by space-charge field by which the refractive index is modulated in biological materials, researchers have exploited it in restoring image quality blurred by bio-tissue [48].

One of examples for photorefractive effect in restoring image quality in demonstrated in Fig. 3.2 [41], the amplitude and phase of scattered beam from bio-tissue are recorded, and the backward phase conjugation wave is generated. After the phase conjugation wave propagates through bio-tissue, the wave front of scattered beam will be recovered and turbidity suppression can be achieved.

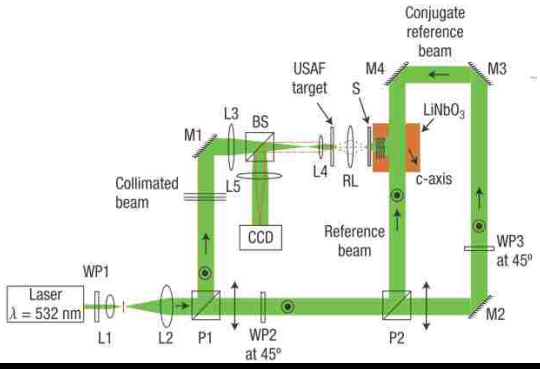

Four-waves mixing also has been explored for image restoration, and it has the feature of

instantaneous response, compared with photorefractive effect. Four-waves mixing based on three order nonlinear process requires two pump beams, as shown in Fig. 3.3 [45]. In this configuration, backward phase conjugation is generated with forward input beam.

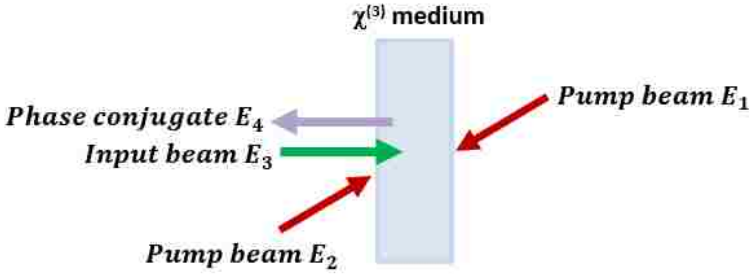

Fig. 3.3. Illustration of generation of phase conjugation by three-waves mixing.

3.1.2 Advantages of Phase Conjugation Generated from Second Order Nonlinear Process

As above mentioned, several different approaches have been adopted for achieving OPC, such as photorefractive effect and four-waves mixing. However, they have some drawbacks in their mechanisms. Four-waves mixing has been demonstrated in [49, 50], but it requires too high power, since high order nonlinear effective coefficient is quite small. This makes the four-waves mixing not be a practical scheme for image restoration in atmospheric turbulence.

While for photorefractive effect, the response speed is quite slow, usually 10^{-3}-1s [51, 52]. Atmospheric turbulence has the characteristics of dynamics and randomness [53, 54] in distorting the wave front of input beam for forming image, such feature is generated by rapidly changing refractive index in atmospheric turbulence, which is caused by moisture, variations in composition, air pressure and so on [55]. As a result, the image restoration based on photorefractive effect can't be utilized in restoration of image blurred by dynamic atmospheric turbulence, since it requires instantaneous response after input beam is sent through dynamic atmospheric turbulence.

Compared with four-waves mixing, the pump power for second order nonlinear process is much lower. The scheme of phase matching condition for generating phase conjugation based on second order nonlinear process in demonstrated in Fig. 3.4. Usually the theta angle (θ) is very small and can be negligible in practical case.

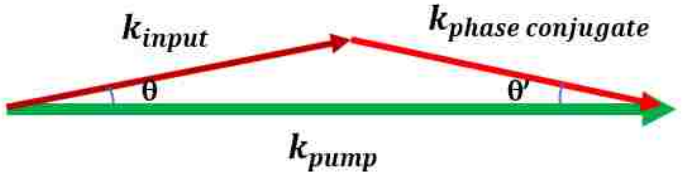

In Ref. [56, 57], experiments of phase conjugation based on second order nonlinear process have been conducted, however only specific polarization and wavelength of pump beam can be used for generation of OPC, since phase matching condition is needed to be met. Some nonlinear materials have been studied for phase conjugation based on DFG, such as β-BaB_2O_4 (BBO), but generation of phase conjugation is sensitive to the polarization of pump beam [58]. Investigation of quality of phase conjugation affected by flatness of pump wave front shows that the mechanism also encounters such disadvantage [59]. In order to make an experimental scheme to be a practical one, polarization insensitivity to pump beam is a very important criteria, since natural light is randomly polarized. In Ref. [60], dual wavelengths were generated from two OPOs based on two periodically poled lithium niobate (PPLN) pumped by the same laser, however, the polarization of dual idlers is the same. In contrast, in the previous work, generation of signal twins and idler twins from AFB-KTP has been achieved [12, 14]. At the degenerate point, it consists of signal and idler beams. Since signal and idler have perpendicular polarizations, polarization-insensitive image restoration can always be achieved at these degenerate points. When the wavelength of pump beam is shifted to

nondegenerate points within some certain region, polarization-insensitive image restoration also can be achieved if phase matching condition is met.

In this chapter, broadband and polarization-insensitive restoration of image by phase conjugation through difference frequency generation (DFG) is studied. Such scheme overcomes disadvantages in the methods mentioned above. Second order nonlinear coefficient is much larger than the third order nonlinear coefficient, so the pump power needed for achieving phase conjugation can be very low. Based on second order nonlinear process, the response speed is limited by temporal resolution, so it is instantaneous. Polarization-insensitive image restoration is achieved by adhesive-free-bonded (AFB) periodically inverted $KTiPO_4$ (KTP), it can be realized in both cases of *s*-polarized and *p*-polarized input beam.

3.1.3 Theoretical Work on Achieving Phase Conjugation with Low Pump Power

It has been demonstrated that the nonlinear reflectivity rate of backward phase conjugation can be approached to 100% in theoretical calculation in a novel scheme, and only ~ 1 mW low pump power is needed for achieving backward phase conjugation by DFG in a second order nonlinear crystal [61]. For this scheme, as shown in Fig. 3.5, pump beam resonates in the intracavity OPO and its power is significantly reduced to few mili-Watts, and nonlinear cavity reflectivity rate is dramatically increased by Fabry-Perot cavity for second order nonlinear crystal stacks. Another feature for this scheme is that broadband phase conjugation can be achievable in periodically inverted poled KTP stack, which is beneficial for realizing QPM in DFG.

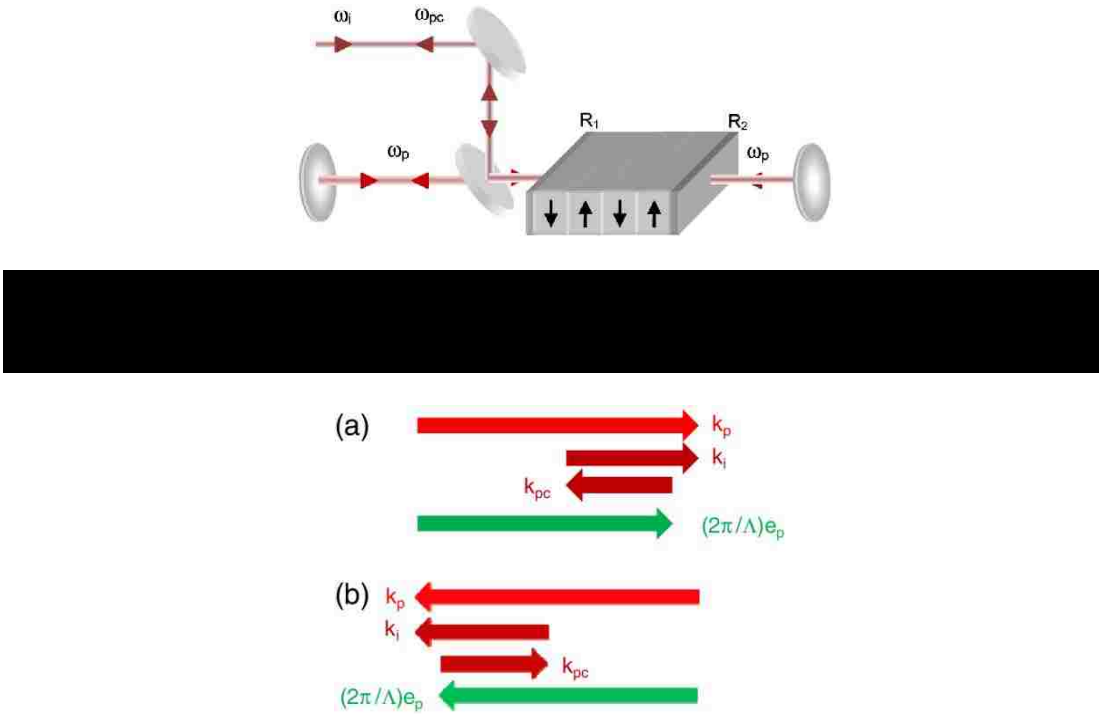

Fig. 3.6. Demonstration of backward quasi-phase matching by three-waves mixing. Wave vectors in (b) are reversed relative to in (a).

Under this novel configuration, pump power of 0.1% threshold power for achieving backward parametric oscillation is needed in order to get 100% reflectivity rate for phase conjugation. When the pump power is slightly higher than several mili-Watts, the reflectivity rate of phase conjugation will be larger than 1. While for the configuration without phase conjugation mirror, the pump power needed is much higher. The response time for this scheme based on second order nonlinear crystal is not only dedicated by temporal resolution of pump beam, but also laser cavity response time due to the presence of resonant cavity for pump beam.

3.1.4 Organization of Chapter 3

In this chapter, three experiments are demonstrated: novel scheme of image recovery after image distorted by phase distortion [15], transmission configuration [16] and reflection configuration [62]

of restoration of image blurred by atmospheric turbulence. In novel scheme experiment, a home-made phase distortion plate is placed in the beam path of input idler to severely distort the image. The distortion of wave front is produced by the non-uniform surface of phase plate. For transmission configuration and reflection configuration of image recovery, a pseudo-Kolmogorov phase plate is adopted to simulate the distortion effect caused by dynamic atmospheric turbulence, such phase plate is made of acrylic and optical polylar region by Near-Index-Match technology [63].

Here I would like to figure out the difference and connection among these three experiments. In novel scheme of image restoration, it demonstrates that broadband and polarization-insensitive restoration of wave front blurred by phase distortion, and it is based on transmission configuration. This novel scheme is applied in correcting image blurred by dynamic atmospheric turbulence in transmission configuration experiment, since the phase conjugation part and original image forming part are separated by distortion plate, there are some limitations on its applications. While for reflection configuration of image restoration, the phase conjugation part and original image forming part are on the same side, it is an important step for practical utilization, such as in biological turbidity suppression in bio-imaging.

3.2 Polarization-Insensitive Image Recovery Based on Phase Conjugation by Three-waves Mixing: Novel Scheme

3.2.1 Experimental Setup

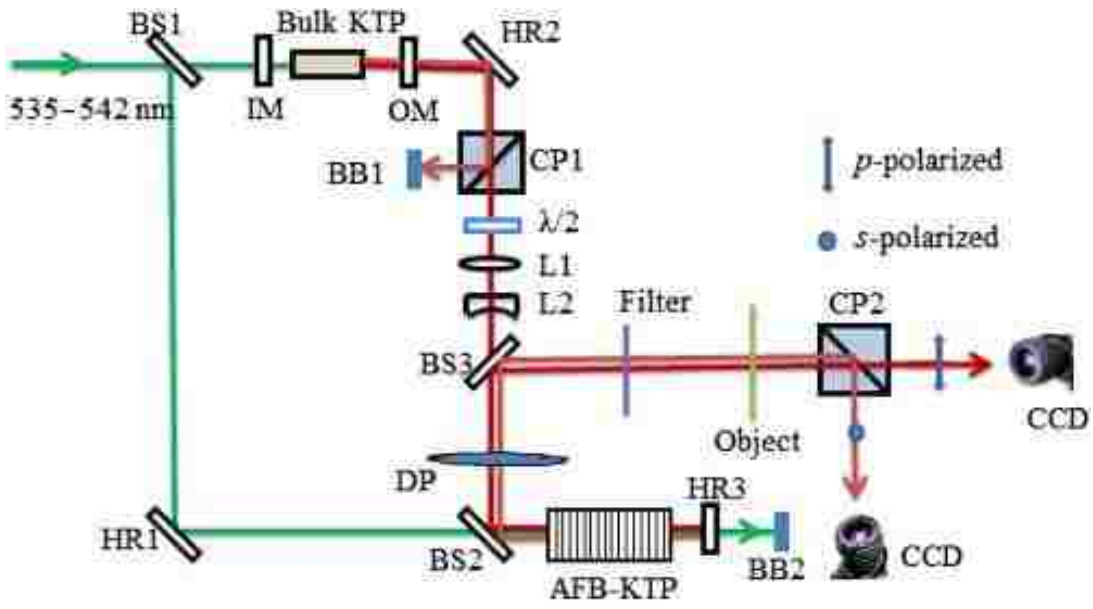

Fig. 3.7. Experimental setup for image reconstruction. BS1-3, beam splitter; IM, input mirror; OM, output mirror; H1-3, high reflection mirror; CP1-2, cubic polarizer; L1-2, convex and concave lens; λ/2, half-wave plate; DP, distortion plate; CCD, CCD camera.

Fig. 3.7 illustrates the experimental setup for image recovery with features of broadband and polarization insensitivity through phase conjugated beams generated from second order nonlinear composite. High power laser system of Quanta Physics- master oscillator/Power oscillator generates tunable wavelength 535 nm-542 nm with 10 Hz repetition rate and 4.8 ns pulse width. After passing through beam splitter BS1, pump beam is divided into two parts, one part is used in generation of 1 μm input beam from optical parametric oscillator, while another part is utilized for generation of phase conjugated beams in AFB-KTP composite by three-waves mixing. Signal and idler beams are coupled out of bulk KTP based OPO cavity, and idler is separated from mixing beams by cubic polarizer 1. Idler input beam for forming original image is beam-size enlarged and collimated by

convex lens L1 and concave lens L2. Also the polarization of idler input can be tuned by a half wave polarizer. A phase distortion is casted on input idler after a distortion plate is placed in its beam path. For our imaging system, the equivalent length of two beam arms guarantees the spatial and temporal overlap of input idler and pump beam, resulting in efficient generation of phase conjugated beams by DFG in AFB-KTP composites. Different from distorted idler input beam, a phase distortion term with opposite sign is imposed on phase conjugated beam. Both of idler input and phase conjugated beam are reflected back by high reflection mirror HR3 and retrace the incoming beam path. For idler input beam, another phase distortion is added and then total distortion accumulates to be twice, which makes wave front severely distorted. In contrast, the phase distortion terms are cancelled after phase conjugated beams pass through distortion plate, which indicates that the phase conjugated beams can be used in blurred image correction. The phase conjugated beams with restored wave front and idler input beam with distorted wave front are reflected by BS3 and directed to imaging part. The residue pump and input beam are filtered out by a filter. The mixing beams of idler input and phase conjugated beams illuminate a USASF target and carry the information of object. Due to the perpendicular polarization of idler input and phase conjugated beams, the images formed by idler input (original image without phase distortion and distorted image) and restored image are captured by two separated CCD cameras. For *p*-polarized idler input, image without wave front distortion and blurred image are captured by CCD 1, and reconstructed image formed by *s*-polarized phase conjugated beams is captured by CCD 2.

3.2.2 Results and Discussions

3.2.2.1 Polarization-Insensitive Image Restoration Achieved at Degenerate Point of Pump Beam

The dependence of wavelength of signals and idlers generated from AFB-KTP composite on pump beam is measured and demonstrated in Fig. 3.8. With 539 nm pump beam (degenerate point), due to quasi-matching condition, two sets of signals and idlers are generated from OPO cavity. The four wavelengths merge into two wavelengths at this degenerate point, one of wavelengths is around 1073 nm, and the other is around 1083 nm.

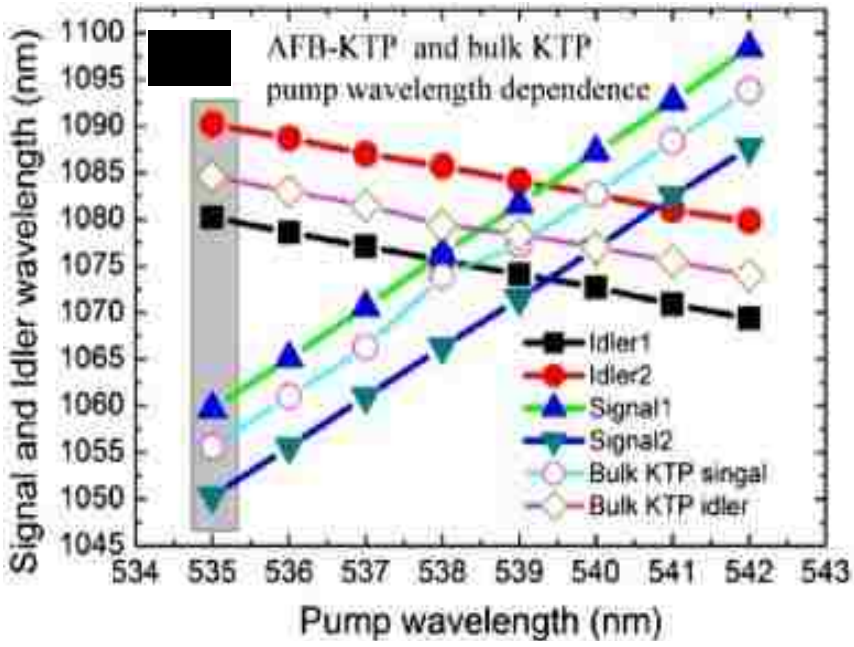

Fig. 3.8. Wavelength of Signals and idlers generated from bulk KTP crystal and AFB-KTP composite versus pump wavelength (535nm-542nm).

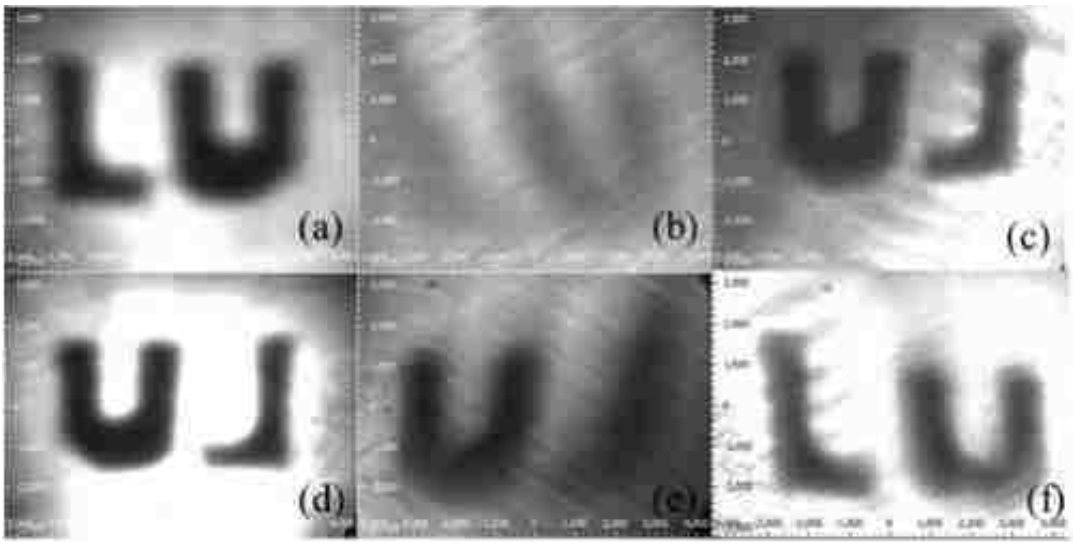

Fig. 3.9. Polarization-insensitive image restoration at near degenerate point of 539 nm. Original images without phase distortion generated by (a) *p*-polarized and (d) *s*-polarized input beam; (b) and (e) Images with phase distortion; (c) and (f), recovered images by phase-conjugated beams generated from difference frequency generation.

The polarization-insensitive image recovery is demonstrated in Fig. 3.9 at pump wavelength of 539 nm. The original image shown in Fig. 3.9(a) and Fig. 3.9(d) are formed by *p*-polarized and *s*-polarized input beams' direct illumination on target. After the insertion of distortion plate in the beam path of idler input, a phase distortion term is imposed on wave front of idler input, resulting in generation of blurred images [Fig. 3.9(b) and Fig. 3.9(e)]. The blurred images are cleaned up by *s*-polarized and *p*-polarized phase conjugated beams generated by DFG in AFB-KTP composite, as shown in Fig. 3.9(c) and Fig. 3.9(f), the object information is reconstructed by phase conjugated beams effectively. The polarization-insensitive image restoration can be achieved at the degenerate point of 539 nm, the mechanism lies in that there are dual polarizations of phase conjugated beams for image correction. An estimated 80% image quality is restored by phase conjugation in Fig. 3.9(c) and Fig. 3.9(f).

3.2.2.2 Polarization-Insensitive Image Restoration Achieved at Nondegenerate Point of Pump Beam

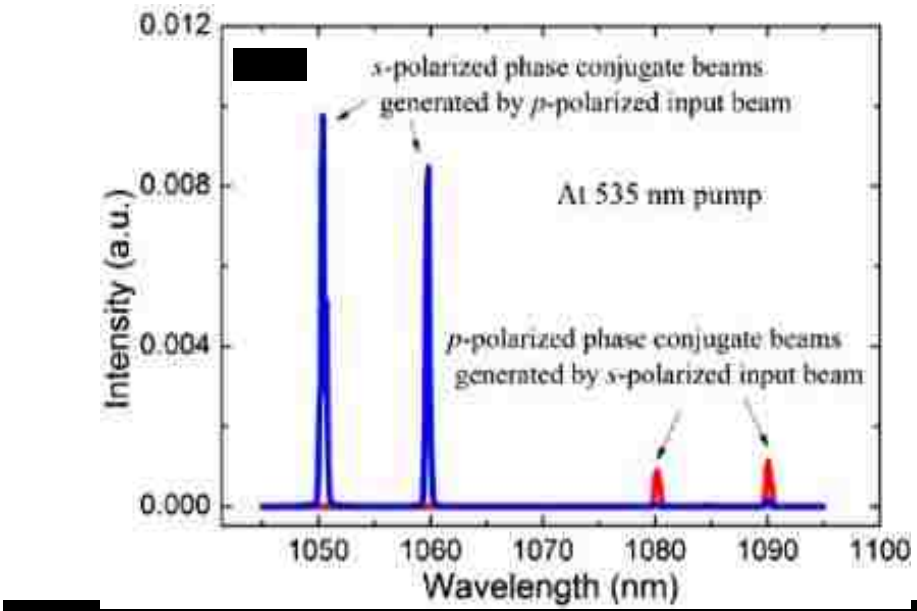

Polarization-insensitive image recovery not only can be achieved at degenerate point of pump beam, but also can be realized at nondegenerate point. At pump wavelength of 535 nm, the wavelength of idler input is around 1085 nm, and *p*-polarized phase conjugated beams with wavelengths of ~1080 nm and ~1090 nm are generated by *s*-polarized idler input [Fig. 3.10]. Through tuning the polarization of idler input to *s* polarization, *p*-polarized phase conjugated beams (~1060 nm and ~1050 nm) are generated for image correction [Fig. 3.10]. The wavelengths of these dual phase conjugated beams are the same with those of being coupled out of AFB-KTP based OPO cavity, as shown in Fig. 3.8.

Fig. 3.11 demonstrates the image quality is recovered by phase conjugated beams at pump wavelength of 535 nm. Fig. 3.11(a) is the image without wave front's distortion formed by *p*-polarized input beam. The image information is completely lost with phase distortion for idler input, [Fig. 3.11(b)]. The phase abbreviation is eliminated by *s*-polarized phase conjugated beams and image information is recollected [Fig. 3.11(c)]. Similarly, the *s*-polarized idler input beam generated original image [Fig. 3.11(d)] becomes blurred by phase distortion [Fig. 3.11(e)], and *p*-polarized phase conjugated beams correct the wave front's distortion for image [Fig. 3.11(f)], the image quality is effectively recovered as the one by *s*-polarized phase conjugated beams [Fig. 3.11(c)].

Furthermore, polarization-insensitive image recovery can be achieved within broad wavelength range of 535 nm-542 nm. At this broadband wavelength, image recovery can be realized in both cases of *p*-polarized and *s*-polarized input beam, in which the corresponding *s*-polarized or *p*-polarized phase conjugated beams from AFB-KTP composite are utilized. Our scheme overcomes the disadvantages reported in Ref. [56], in which phase conjugated beams can only be generated by input beam with specific wavelength and polarization. One shortcoming for our configuration is that

we should make sure that the CCD cameras and phase conjugated beam are as close as possible, since there may exist small angle between phase conjugated beams due to the mechanism of their generation.

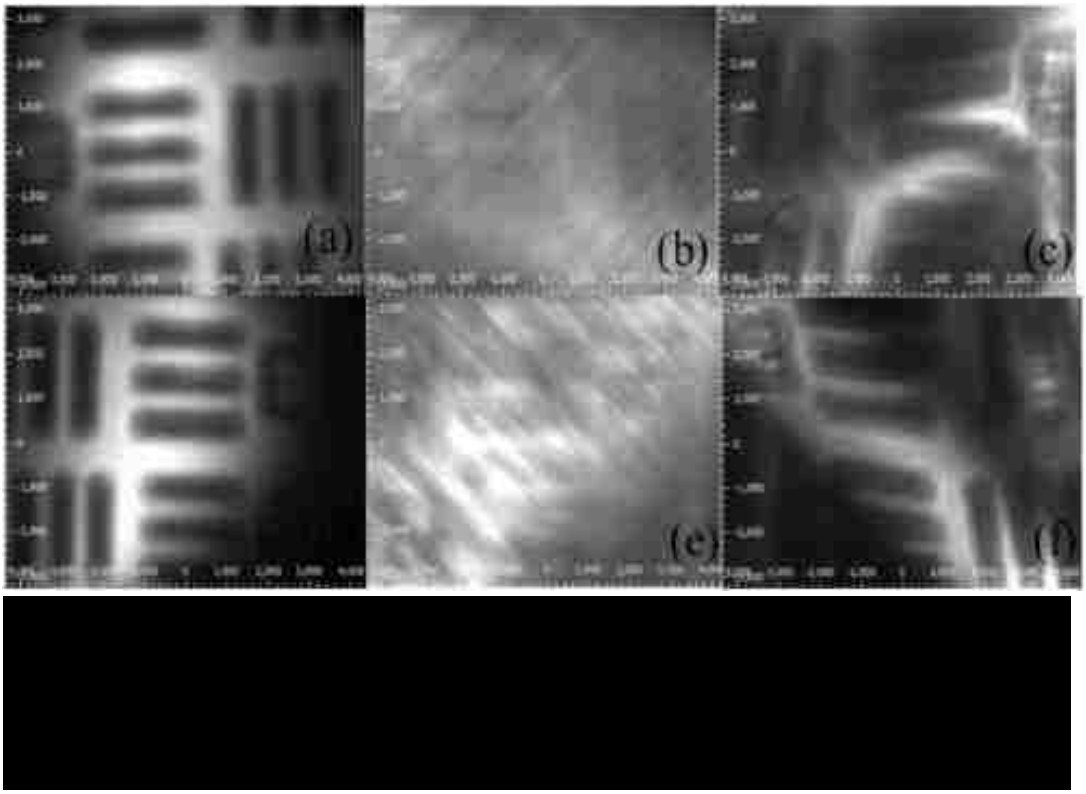

3.2.3 Summary of Project

In this project, polarization-insensitive image recovery is realized by phase conjugation in second order nonlinear composite by DFG process. Instead of using bulk KTP for generation of phase conjugated beams, AFB-KTP composite is adopted. Only low input beam power and pump power are needed for our configuration, since the phase conjugation gain of second order nonlinear process is much higher than higher order ones, and also 100% reflectivity rate for phase conjugation can be achieved in theory. Finally, polarization-insensitive image recovery can be realized within broad pump wavelength of 535 nm-542 nm.

3.3 Reconstruction of Image Blurred by Simulated Atmospheric Turbulence through Phase Conjugation Beams from Second Order Nonlinear Crystal: Transmission Configuration

3.3.1 Experimental Setup

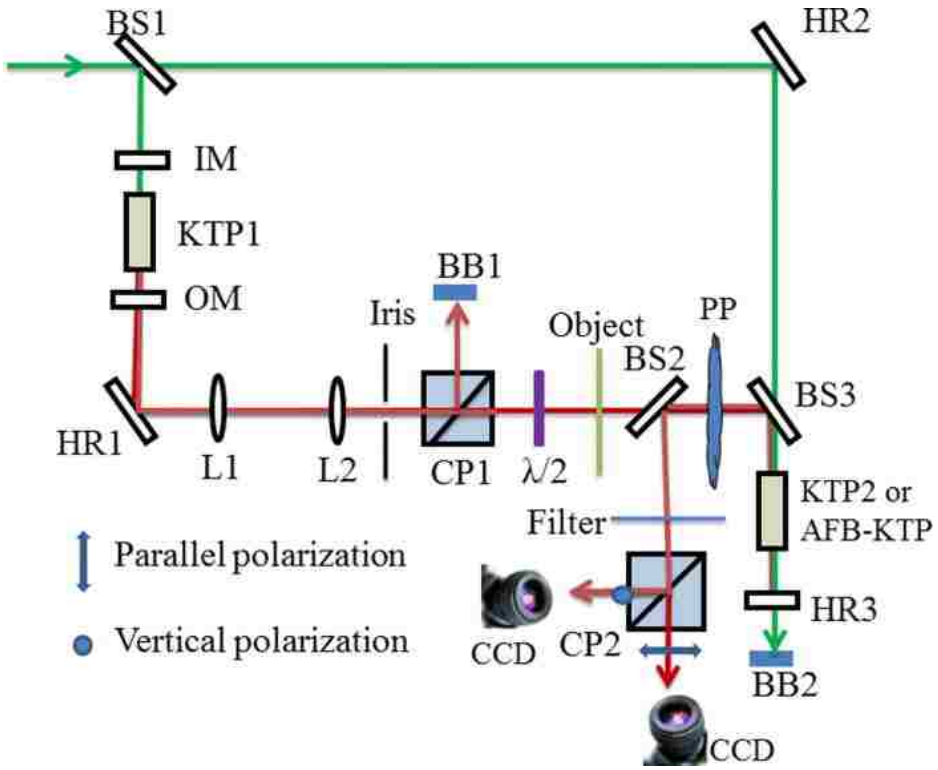

Fig. 3.12. Experimental setup for image recovery. BS1-2, beam splitter; IM, input mirror; OM, output mirror; HR1-3, high reflection mirror; CP1-2, cubic polarizer; L1-2, convex lens; λ/2, half-wave plate; PP, distortion phase plate; BB1-2, beam block; CCD, CCD camera.

Fig. 3.12 demonstrates the experimental setup for restoration of image blurred by simulated atmospheric turbulence based on transmission configuration. Beam splitter BS1 divides green pump beam into two arms, one arm is used for DFG process with idler input beam in nonlinear bulk KTP crystal or AFB-KTP composite. Another arm of pump beam is utilized as pump source for optical parametric oscillator based on bulk KTP 1. The higher power laser pulse is generated by a MOPO

system of Quanta Physics with 10 Hz repetition rate and 4.8 ns duration width. In order to guarantee efficient generation of phase conjugated beams, the length of arm 1 and arm 2 is close to each other, which makes the temporal and spatial overlap of idler input beam and pump beam in nonlinear bulk crystal or composite. One pair of signal and idler is coupled out of bulk KTP OPO cavity and collimated by lens L1&2, their beam size is adjusted by Iris. Cubic polarizer CP1 is used to separate the idler input beam from signal. The initial polarization of idler input beam is *p* polarized and it can be tuned by a half wave plate in its beam path. Without insertion of phase plate between beam splitter BS2 and BS3, the original image is formed. After illuminated on object, idler input beam carrying the information of object transmits through BS2 and directed by BS3 to KTP 2 or AFB-KTP composite, then it is reflected backward by a high reflection mirror HR3 and retraces the incoming beam path. The residual pump beam is blocked by a filter in front of cubic polarizer 2 before the object information is captured by CCD and the corresponding original image is generated. The wave front of idler input beam is distorted by phase plate after its insertion and the corresponding image is severely blurred by phase distortion. The distorted image is captured by the same CCD camera as that for original image. The idler input beam with distorted wave front interacts with green pump beam in bulk KTP 2 or KTP composite for three-waves mixing. Opposite phase distortion relative to that of the distorted idler input beam imposed on the generated phase conjugated beams is cancelled when it propagates through phase plate, resulting in the restoration of image quality. Due to the perpendicular polarization of phase conjugated beams and idler input beam, the recovered image is collected by an encountered CCD camera.

In this project, we achieve real-time restoration of image blurred by dynamic atmospheric turbulence by bulk KTP 2 and polarization-insensitive image restoration by AFB-KTP composite.

Both of them are *x* cut (θ = 90º, φ = 0º). The simulated atmospheric turbulence is mimicked by rotating the pseudo-Kolmogorov phase plate in the beam path. The phase plate is made of 4096 ×4096 phase arrays and it is made by Near-Index-Match optics technology [63, 64]. There is beam path difference in phase arrays of plate and specifically phase distortion is generated by thickness difference of acrylic and optical polymer. For phase plate, one of the important parameters is Fried parameter or spatial coherence length, r_0. It is used to determine the amount of distortion. r_0 is defined as the distance over which the phase changes by the order of 1 rad. In the transmission and reflection configuration of image restoration, r_0 for phase plate is around 0.3 mm at the 1.05 μm.

3.3.2 Image Restoration Achieved by Phase Conjugation from Bulk KTP

3.3.2.1 Demonstration of Image Restoration

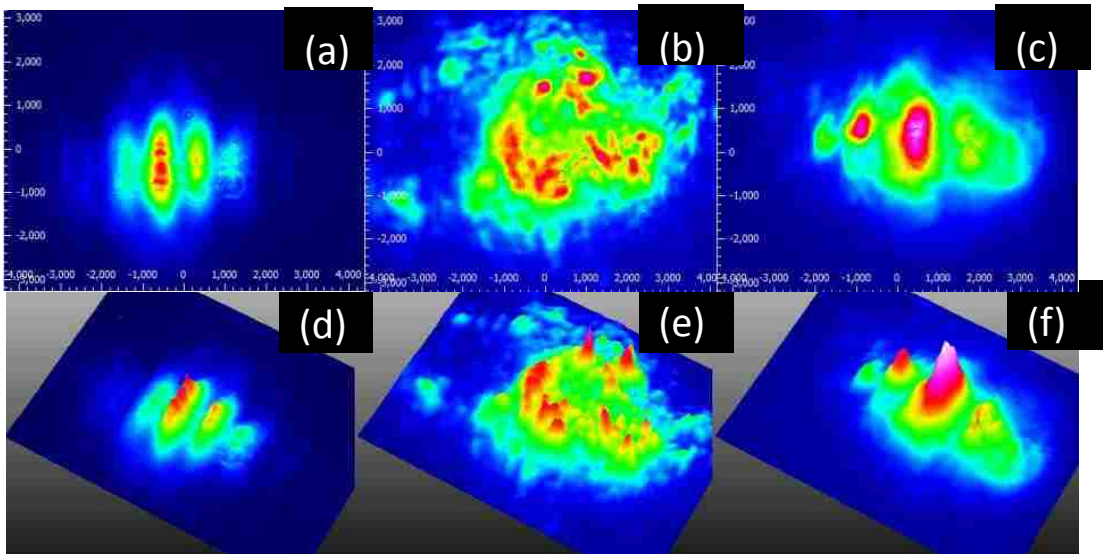

Fig. 3.13. Demonstration of image reconstruction achieved by *s*-polarized phase conjugated beams from bulk KTP crystal. (a) Original images without phase distortion, and (b) images with phase distortion, (c) restored image by phase conjugated beams at pump wavelength of 540 nm. (d),(e) and (f) are the corresponding 3-D images.

Fig. 3.13 illustrates the image restoration by phase conjugation from bulk KTP. There are four separated and clear vertical lobes in original image [Fig. 3.13(a)], and it is completed distorted by

simulated atmospheric turbulence and no object information can be collected [Fig. 3.13(b)]. The phase distortion is effectively removed by phase conjugated beam and image quality is reconstructed [Fig. 3.13(c)], in which vertical lobes become clear again. At pump beam with wavelength of 541 nm, the wavelength of *p*-polarized signal input beam is 1075 nm and its spectra (red color) is shown in Fig. 3.14. Phase conjugated beam is generated by three-waves mixing of 1075 nm signal input beam and 541 green pump beam in KTP 2, and its wavelength is 1089 nm and it is *s* polarized [blue color].

3.3.2.2 Centrosymmetric Inversion of Original Image and Recovered Image in Transmission Configuration

Phase conjugation generated from DFG process needs to meet the phase matching condition. The physical scheme is illustrated in Fig. 3.15. Based on the transmission configuration, the positions of vertical lobes of original image and restored image display centrosymmetric inversion [65], as shown in Fig. 3.16(a) and 3.16(c). Such centrosymmetric inversion is caused by phase matching condition. In practical experiment, due to alignment of optics system for spatial overlap of signal beam and pump beam, there may exist a small angle tilt (θ). The input beam, pump beam and phase conjugated beam need to meet conditions of phase matching and energy conservation in three-waves mixing, so the geometric distribution of phase conjugated beam should display centrosymmetric inversion relative to that of signal input beam or idler input beam.

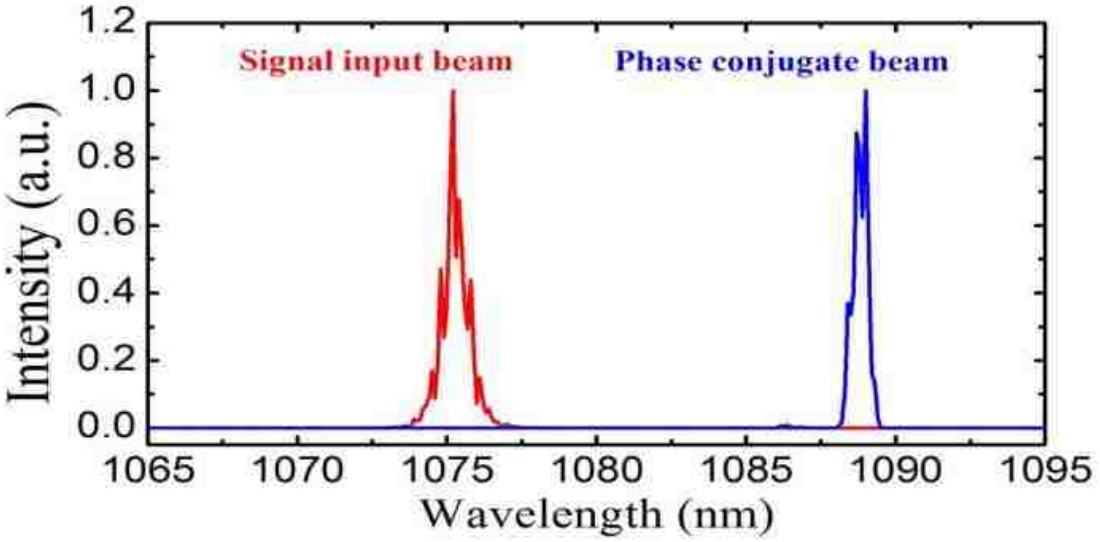
Signal input beam
Phase conjugate beam
Intensity (a.u.)
1.2
1.0
0.8
0.6
0.4
0.2
0.0
1065
1070
1075
1080
1085
1090
1095
Wavelength (nm)

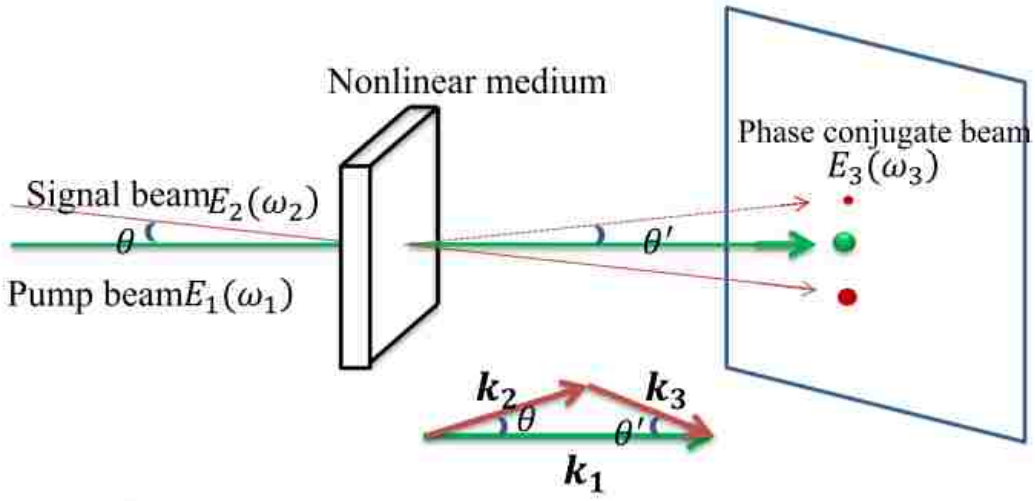
Nonlinear medium
Phase conjugate beam
$E_3(\omega_3)$
Signal beam$E_2(\omega_2)$
θ
θ'
Pump beam$E_1(\omega_1)$
k_2
k_3
θ
θ'
k_1

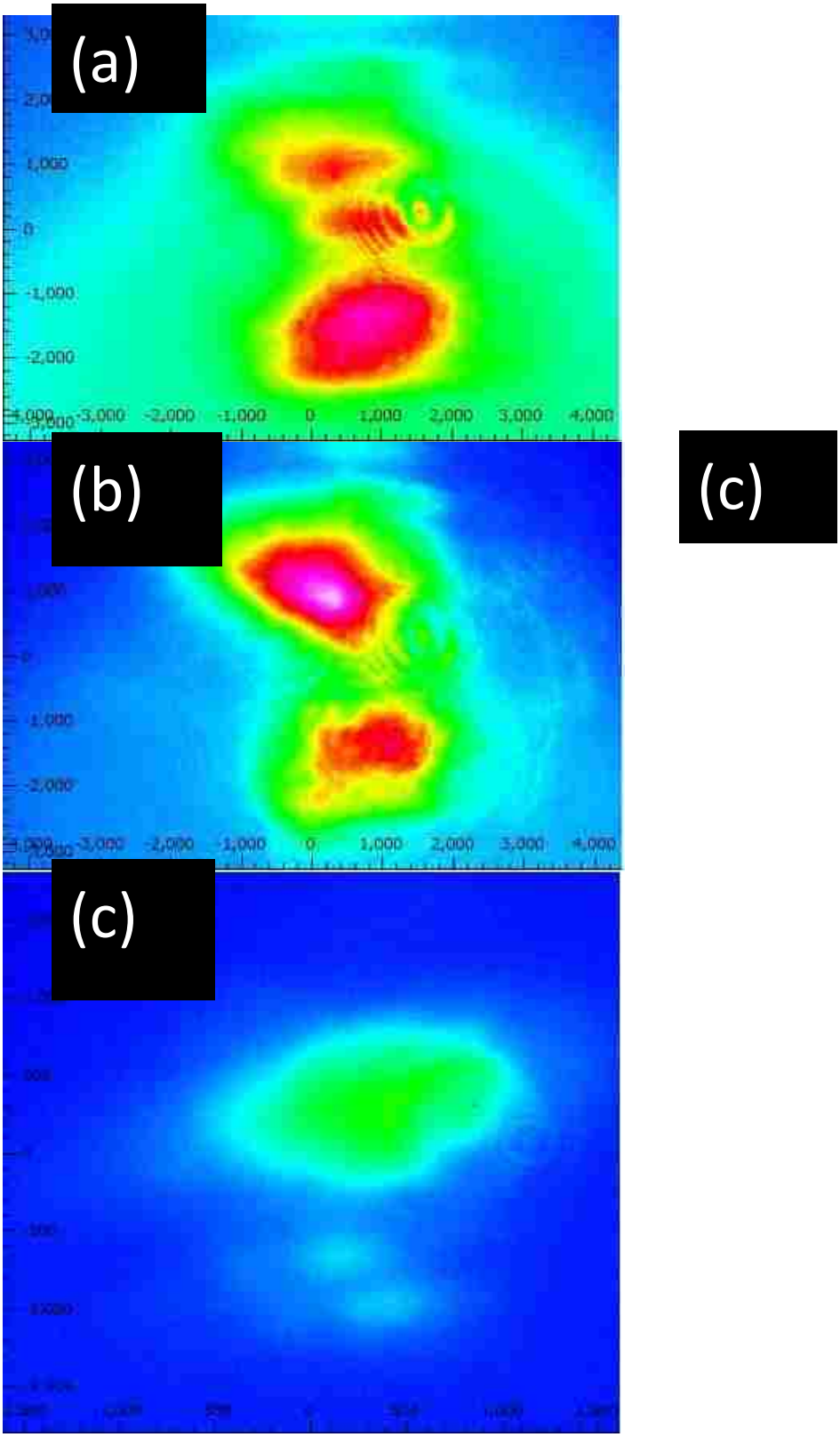

Fig. 3.16. Demonstration of centrosymmetric inversion in reconstruction of image with parallel bars achieved by *s*-polarized phase conjugated beam from bulk KTP crystal. (a) Original image without phase distortion, (b) image with phase distortion and (c) restored image by phase conjugated beam at pump wavelength of 540 nm.

The centrosymmetric inversion between original image and restored image is demonstrated in Fig. 3.16. Fig. 3.16(a) shows the unique pattern of original image with three distinguishable parallel bars, and the brightest one is at the lowermost position. After the wave front of input beam is distorted by turbulence, there are only two bars left in Fig. 3.16(b), which means that object information becomes incomplete. The image is restored by phase conjugation and it is shown in Fig. 3.16(c). Its pattern is similar to original image with three clear bars. Originated from phase matching condition between pump beam, input beam and phase conjugation beam, it demonstrates centrosymmetric inversion between restored image and original image.

3.3.2.3 Image Restoration in Dynamic Atmospheric Turbulence

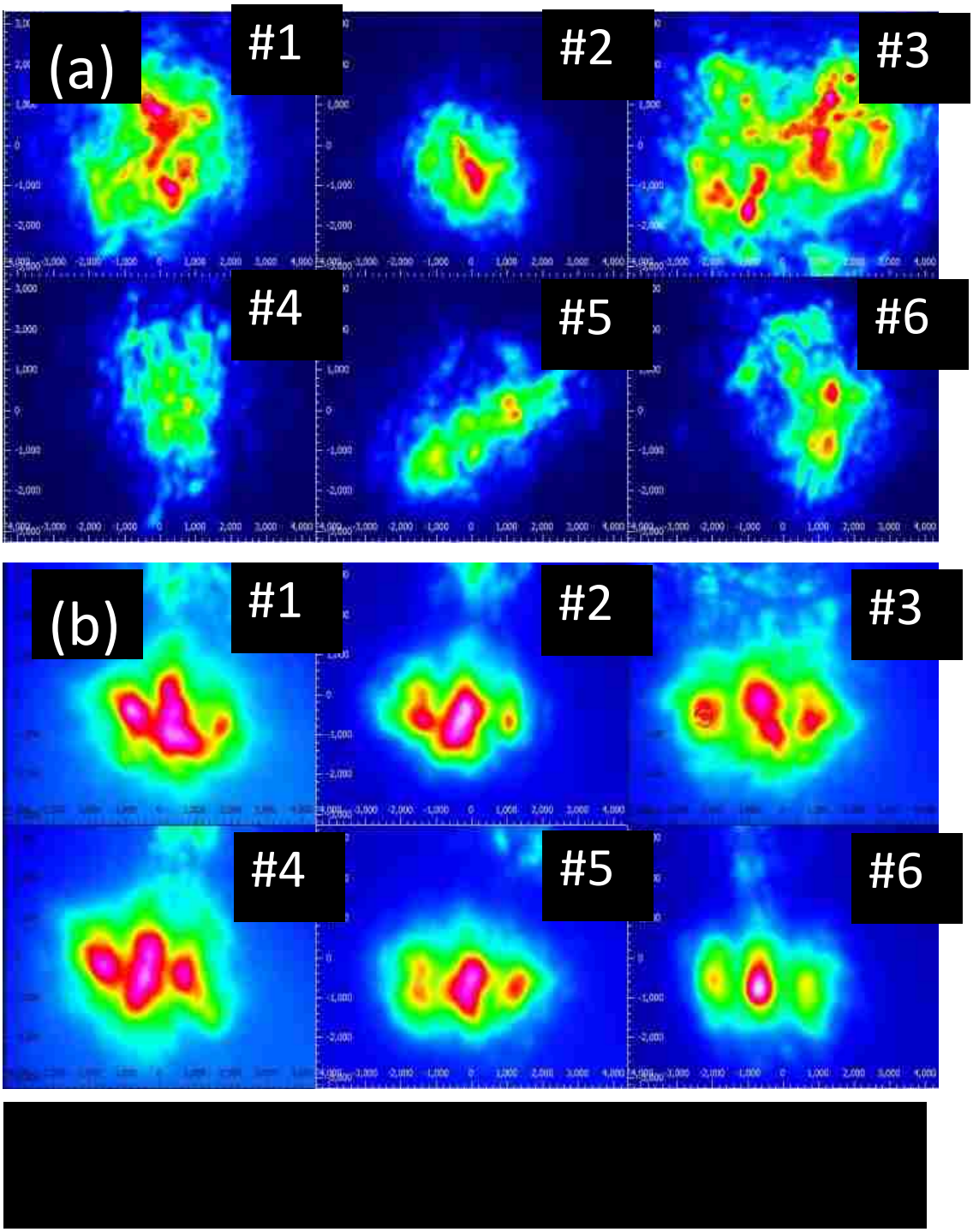

Real-time recovery of image blurred by atmospheric turbulence by phase conjugated beam is demonstrated in Fig. 3.17. Through random rotation of phase plate, atmospheric turbulence is mimicked. The information of object in original image is displayed in Fig. 3.13(a). A phase

distortion is imposed on idler input after it passes through the phase plate, as shown in Fig. 3. 17(a). At six different rotation positions of phase plate, distorted image patterns are recorded and no object information can be collected. Fig. 3.17(b) shows that images suffered from distortion of atmospheric turbulence are restored by phase conjugated beams generated from bulk KTP 2. Benefits from property of instantaneous response speed of DFG in second order nonlinear crystal, real-time image recovery can be achieved when idler input beam propagates through dynamic atmospheric turbulence. Each restored image contains clear and spatially separated vertical bars.

3.3.3 Polarization-Insensitive Image Restoration Achieved by Phase Conjugation from AFB-KTP

3.3.3.1 Phase Matching Condition and Spectra Study

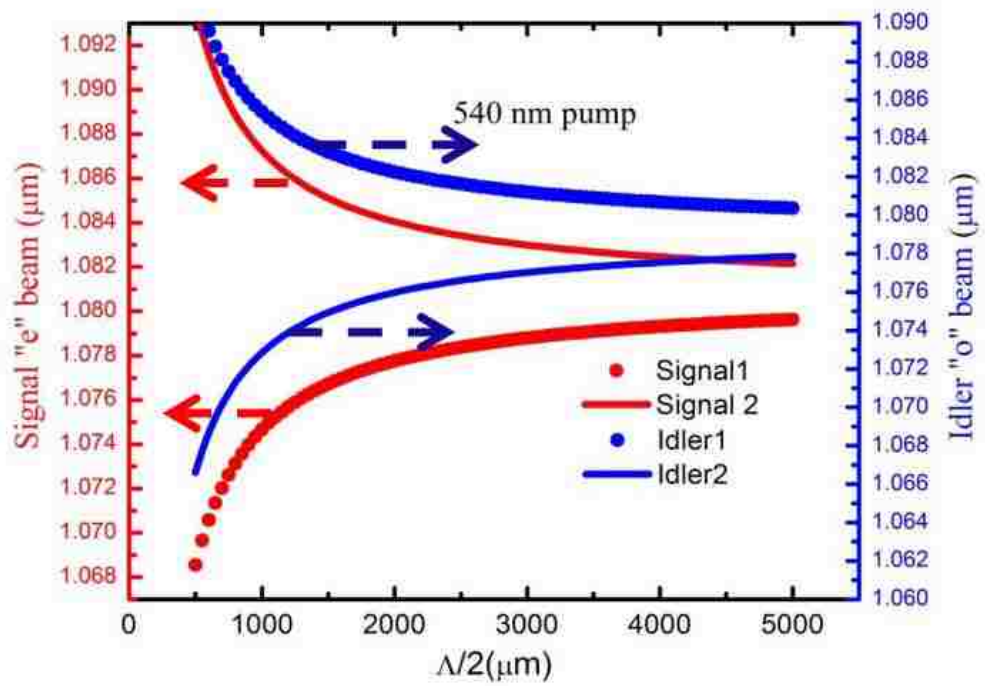

An AFB-KTP composite is utilized in polarization-insensitive image restoration. The calculated wavelengths of signals and idlers are shown in Fig. 3.18. For generation of signals and idlers in

AFB-KTP composite, the wavelengths of signals and idlers need to satisfy phase matching condition and energy conservation condition:

$$\frac{n_p}{\lambda_p} - \frac{n_s}{\lambda_s} - \frac{n_i}{\lambda_i} \pm \frac{1}{\Lambda} = 0 \qquad (7)$$

$$\frac{1}{\lambda_p} - \frac{1}{\lambda_s} - \frac{1}{\lambda_i} = 0 \qquad (8)$$

Where λ_p, λ_s ,λ_i are wavelength of pump beam, signal beam and idler beam, respectively; Λ is the thickness of single crystal thickness.

Therefore, assisted with Sellmeier equations [66, 67], the wavelengths of signals and idlers can be calculated from phase matching condition and energy conservation.

From the above phase matching condition, it is noticed that compared with the one of bulk KTP, there is an additional term for AFB-KTP composite, ($\pm 1/\Lambda$), resulting in generation of two sets of split signals and idlers, as shown in Fig. 3.19. For AFB-KTP, the domain structure is usually greater than 500 micrometers, so it gives small perturbation in phase matching. Also, plus and minus sign are both allowed in phase matching condition, this causes the generation of two pairs of signals and idlers. Such feature is distinguished from PPLN. For PPLN, domain structure for phase matching is usually ten micrometers and there is only one pair of idler and signal generated [68, 69].

One can see that from dependence of wavelengths of signals and idlers on crystal thickness of KTP layer in AFB-KTP composite, as demonstrated in Fig. 3.18, the separation between two signals or two idlers becomes narrower when the crystal length becomes longer, which means that the frequency difference for signal twins or idler twins can be designed by controlling the thickness of KTP crystal.

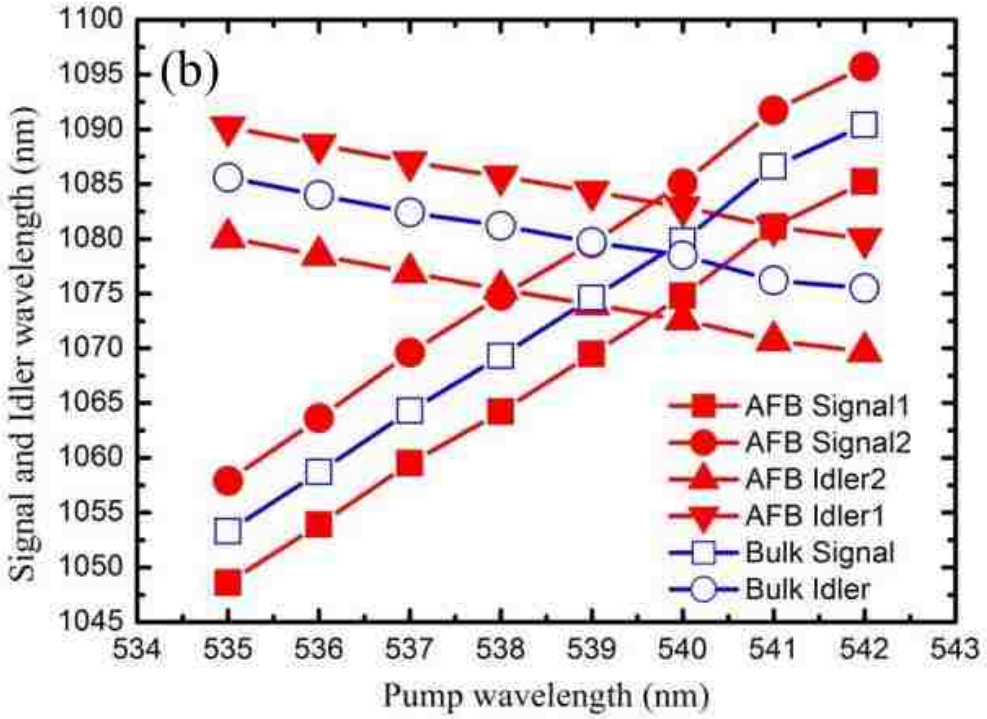

The wavelengths of signals and idlers generated from AFB-KTP and bulk KTP within pump wavelength region of 535 nm-542 nm are measured, as shown in Fig. 3.19. At degenerate point (540 nm), instead of presence of four different wavelengths of signals and idlers, there are only two separated wavelengths. Each joint set contains dual polarization beams: *p*-polarized and *s*-polarized.

3.3.3.2 Polarization-Insensitive Image Restoration by Phase Conjugation from AFB-KTP

For our configuration, the image restoration can be achieved from wavelength of 538 nm to 541 nm. At 540 nm pump (degenerate point), original images formed by *p*-polarized and *s*-polarized idler input beam are displayed in Fig. 3.20(a) and 3.21(a) before the insertion of phase distortion plate. There are three clear vertical bars in original images. The wave fronts of *p*-polarized and *s*-polarized idler input beams are severely distorted by atmospheric turbulence and the information of USAOF is completed lost [Fig. 3.20(b) and 3.21(b)]. The phase distortions are removed by *s*-polarized and

p-polarized phase conjugated beams and images quality is efficiently restored [Fig. 3.20(c) and 3.21(c)]. At the same time, we also demonstrate polarization-insensitive image restoration at pump 537 nm (nondegenerate point). As shown in Fig. 3.22, *s*-polarized phase conjugation effectively reconstructs image quality. Similarly, *p*-polarized phase conjugation also successfully recoveries image information, as demonstrated in Fig. 3.23.

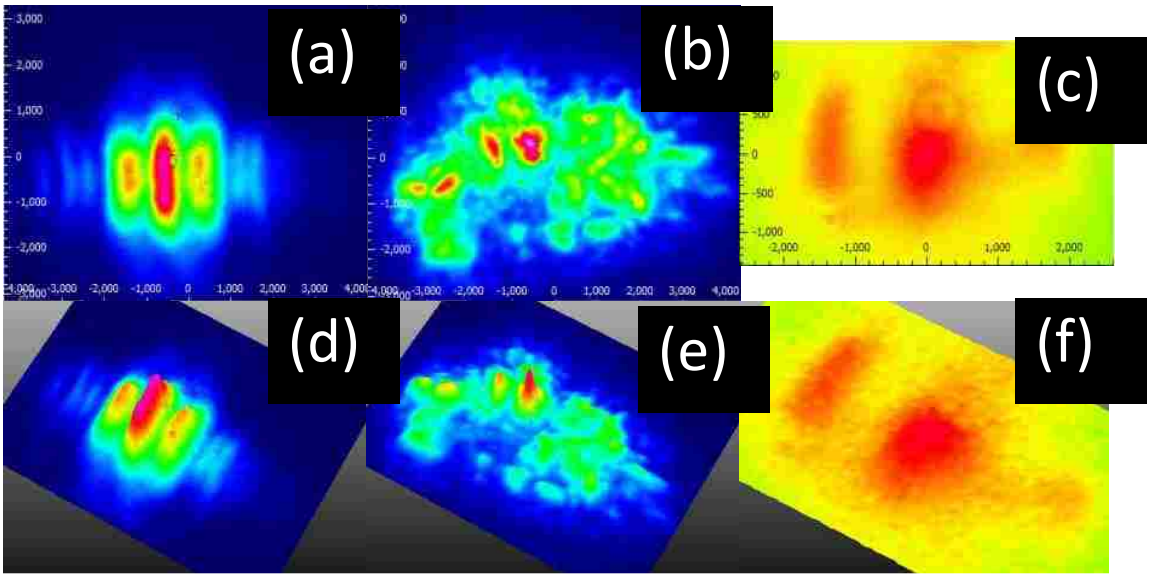

Fig. 3.20. Polarization-insensitive image restoration at degenerate point of 540 nm. Original image without wave front distortion with (a) *p*-polarized; (b) is the distorted image; (c) is recovered image by three-waves mixing. (d), (e) and (f) are the corresponding 3-D images.

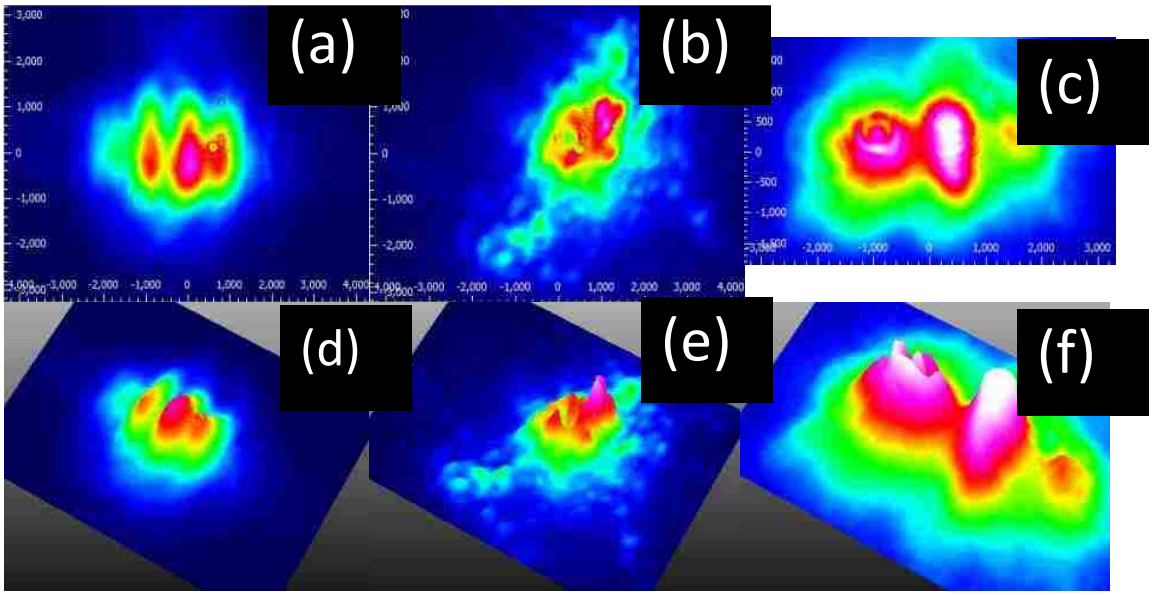

Fig. 3.21. Polarization-insensitive image restoration at degenerate point of 540 nm. Original image without wave front distortion with (a) *s*-polarized input beams; (b) is distorted image; (c) is recovered image by three-waves mixing. (d), (e) and (f) are the corresponding 3-D images.

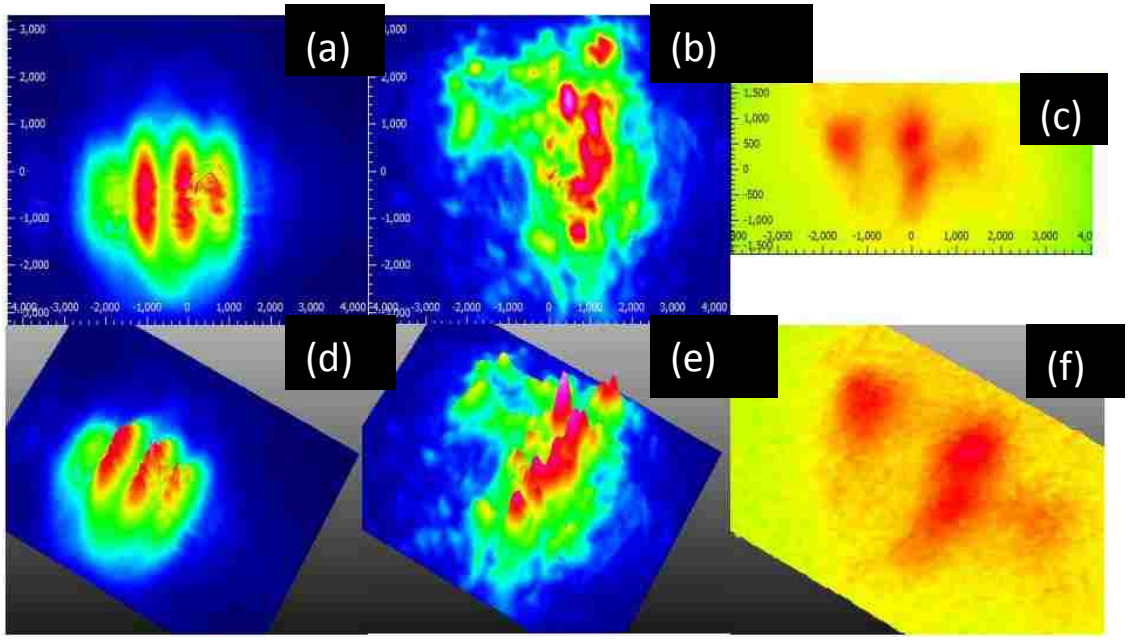

Fig. 3.22. Polarization-insensitive image restoration at nondegenerate point of 537 nm. (a) Original image without wave front distortion with *p*-polarized input beam; (b) is distorted image; (c) is recovered image by three-waves mixing. (d), (e) and (f) are the corresponding 3-D images.

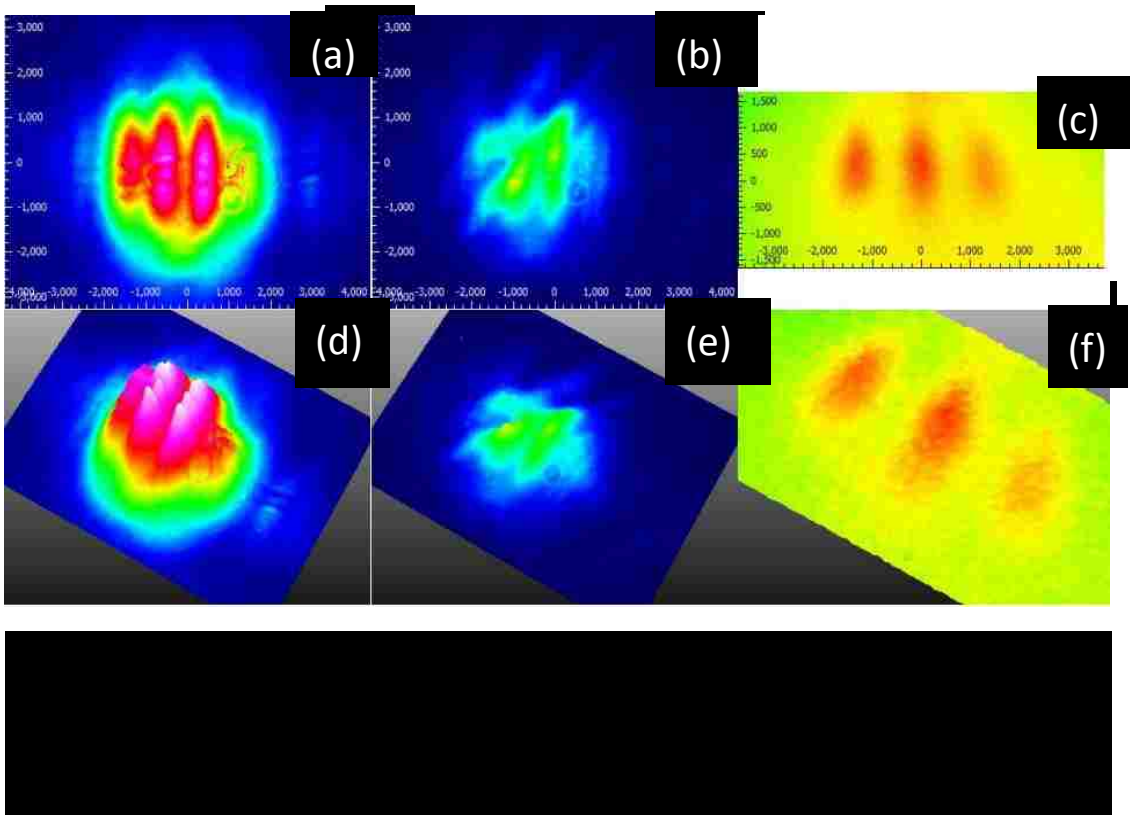

3.3.4 Summary of Project

In this project, real-time restoration of image blurred by dynamic atmospheric turbulence is achieved by phase conjugated beam through DFG process. Atmospheric turbulence distortion is mimicked by random rotation of phase plate in the beam path of idler input beam. The instantaneous response speed makes this scheme to be probably the only one for image correction in atmospheric turbulence. Broadband and polarization-insensitive image restoration is achievable by an AFB-KTP composite, the polarization-insensitive feature is observed even wavelength of pump beam is not at degenerate point. The shortcoming of transmission scheme is that the image restoration part which contains bulk KTP 2 or AFB-KTP composite and the laser source are separated by phase plate, which limits the flexibility in usage of this optics system in practical case.

3.4 Reconstruction of Image Blurred by Simulated Atmospheric Turbulence through Phase Conjugation Beam in Second Order Nonlinear Crystal: Reflection Configuration

3.4.1 Experimental Setup

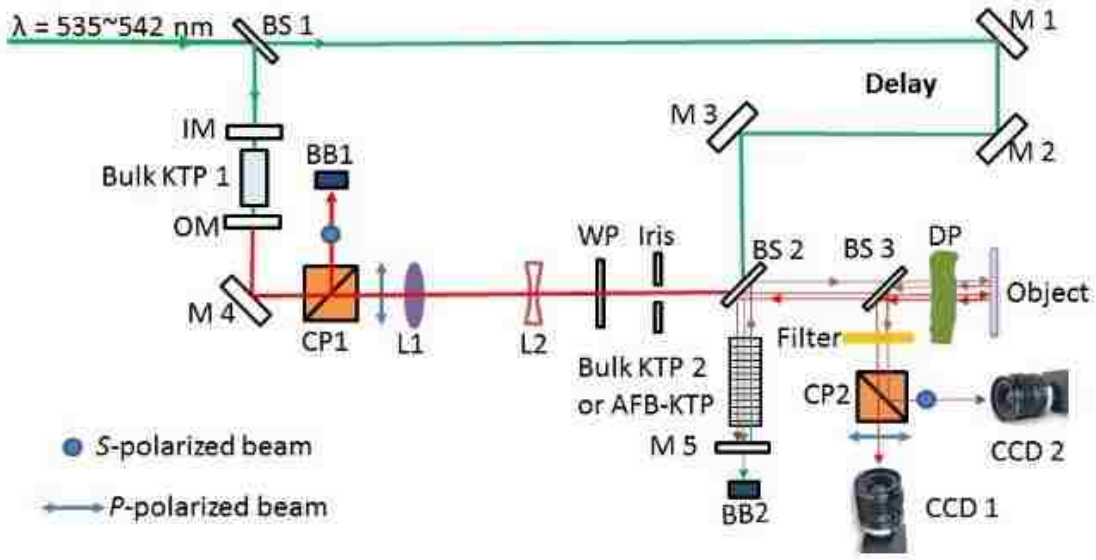

Fig. 3.24. Experimental setup for image recovery by phase conjugation. BS1-3, beam splitter. BS1, 50% reflection for 543 nm pump beam. BS2&3, 50% reflection for 1 μm beams, and high transmission for 543 nm. IM, input mirror; OM, output mirror; M1-5, high reflection mirror; CP1&2, cubic polarizer; L1, convex lens; L2, concave lens; WP, half-wave plate; DP, distortion plate; BB1&2, beam block; CCD1&2, CCD camera.

Fig. 3.24 illustrates the experimental setup for image recovery by phase conjugation based on reflection configuration. The pump beam wavelength is tunable within 535 nm-542 nm with repetition rate of 10 Hz and 4.8 ns pulse duration width. One part of green pump beam reflected by beam splitter BS1 is used as pump source for bulk KTP optical parametrical oscillator. One pair of signal and idler is coupled out of OPO, and cubic polarizer CP1 separates idler from signal beam. Another part of green pump beam is directed by high reflection mirror M1-3 and is mixed with idler input beam by three-waves mixing for phase conjugation generation in bulk KTP crystal or AFB-KTP composite. M1&2 mirrors are adopted to introduce time delay for green pump beam, which

make sure that idler input beam and pump beam are temporal overlapped. Without phase distortion by phase plate, for the *p*-polarized idler input beam, it propagates through BS2 and BS3 and illuminates on the object. One part of reflected and backward propagating idler input beam is directed by BS3 to imaging forming part. After propagating through a filter and cubic polarizer CP2, the object information is captured by CCD1. If a phase plate for mimicking dynamic atmospheric turbulence is placed between BS3 and object, the wave front of idler input will be severely distorted, a phase distortion term is imposed to idler input after it propagates through phase plate, so such phase distortion term will be doubly accumulated for idler input after one round trip. The distorted image will be also captured by CCD1 camera. Another part of reflected and backward propagating idler input beam propagates through BS3 and is reflected by BS2, then it is mixed with pump beam in bulk KTP 2 or AFB-KTP composite for DFG process. *S*-polarized phase conjugated beam is reflected back by M5 mirror and directed into the same beam path of idler input by BS2. Phase distortion term with opposite sign is added to phase conjugated beam, resulting in eliminating wave front distortion. The restored image is captured by CCD2, since phase conjugated beam for image restoration has a perpendicular polarization relative to *p*-polarized idler input beam.

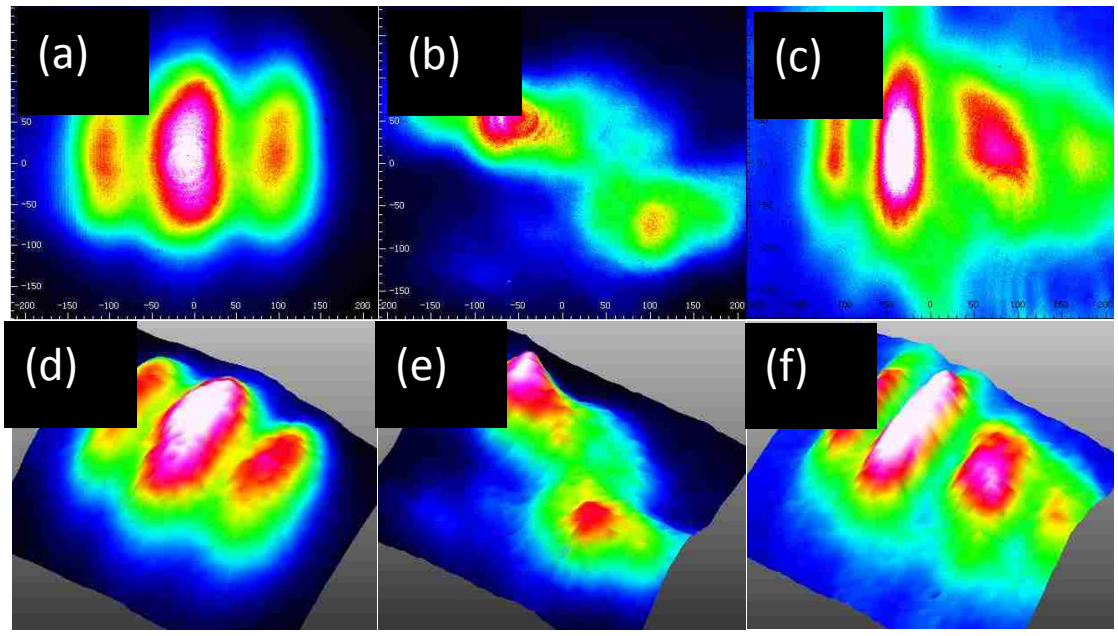

Fig. 3.25. Image recovery by phase conjugation from bulk KTP crystal at pump wavelength of 540 nm. (a) Original image generated by *p*-polarized input beam without phase distortion, and (b) distorted image, (c) reconstructed image by *s*-polarized phase conjugated beam. (d), (e) and (f) are the corresponding 3-D images.

Image recovery by phase conjugated beam generated from bulk-KTP2 with 540 nm pump is achieved and demonstrated in Fig. 3.25. The original image is formed by illumination of *p*-polarized idler input beam on object and captured by CCD1 camera, as shown in Fig. 3.25(a), there are three distinguished vertical bars. The image becomes blurred after wave front of idler input is severely distorted by a phase plate [Fig. 3.25(b)]. Fig. 3.25(c) shows that image quality is effectively restored by *s*-polarized phase conjugated beam.

3.4.2 Image Restoration Achieved by Phase Conjugation from Bulk KTP

3.4.2.1 Demonstration of Image Restoration

The wavelengths of signal and idler generated from bulk KTP based OPO as function of pump beam wavelength is experimentally measured [Fig. 3.26(a)]. From the quasi-phase matching condition, only one pair of signal and idler is generated. At 540 nm pump, the wavelength of idler input beam is 1076.8 nm and *s*-polarized phase conjugated beam is 1083.1 nm. The spectra of *p*-polarized idler input and *s*-polarized phase conjugated beam is demonstrated in Fig. 3.26(b). It can be witnessed that their wavelengths are the same with those coupled out of bulk KTP OPO cavity.

For bulk KTP, the polarization-insensitive image restoration can only be achieved at degenerate point of pump beam. Even pump wavelength is close to degenerate point, polarization insensitivity still can't be observed, e.g. at 540 nm. Original image [Fig. 3. 27(a)] is formed by *p*-polarized idler input beam, and the corresponding restored image is generated from *s*-polarized phase conjugated beam [Fig. 3.27(c)]. With *s*-polarized input beam, the image contrast [Fig. 3.28(c)] for restored image is much weaker than the one generated from *s*-polarized phase conjugated beam [Fig. 3.

27(c)]. The best image contrast can be got in the exact degenerate point.

In conclusion, polarization-insensitive image restoration by phase conjugation from bulk KTP can be only realized in specific pump wavelength. As displayed in Fig. 3.26(a), around 539.5 nm, signal and idler beams merge into one wavelength. With pump wavelength away from degenerate point, polarization-insensitive image recovery can not be achieved.

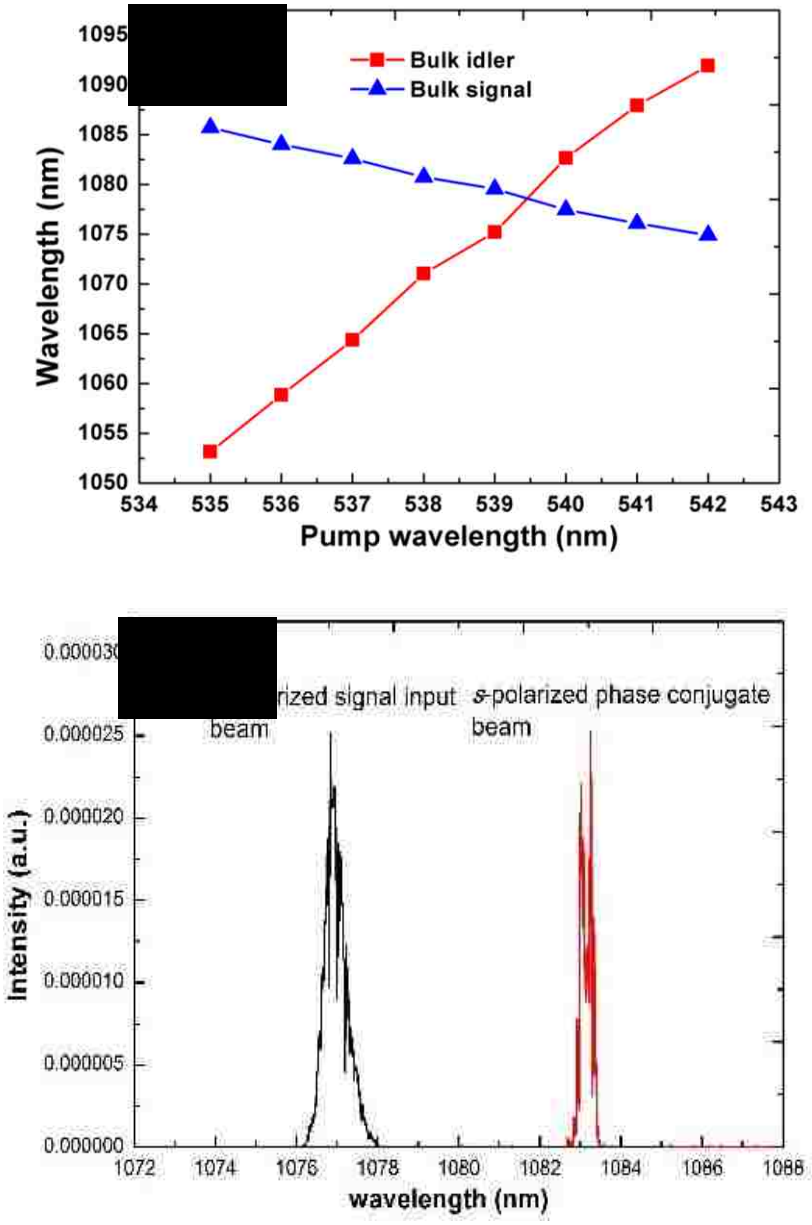

Fig. 3.26 (a) Wavelengths of signal and idler generated from bulk KTP within 535 nm-542 nm pump wavelength region. (b) Spectra of *p*-polarized signal input beam and *s*-polarized phase conjugated beam generated from bulk KTP.

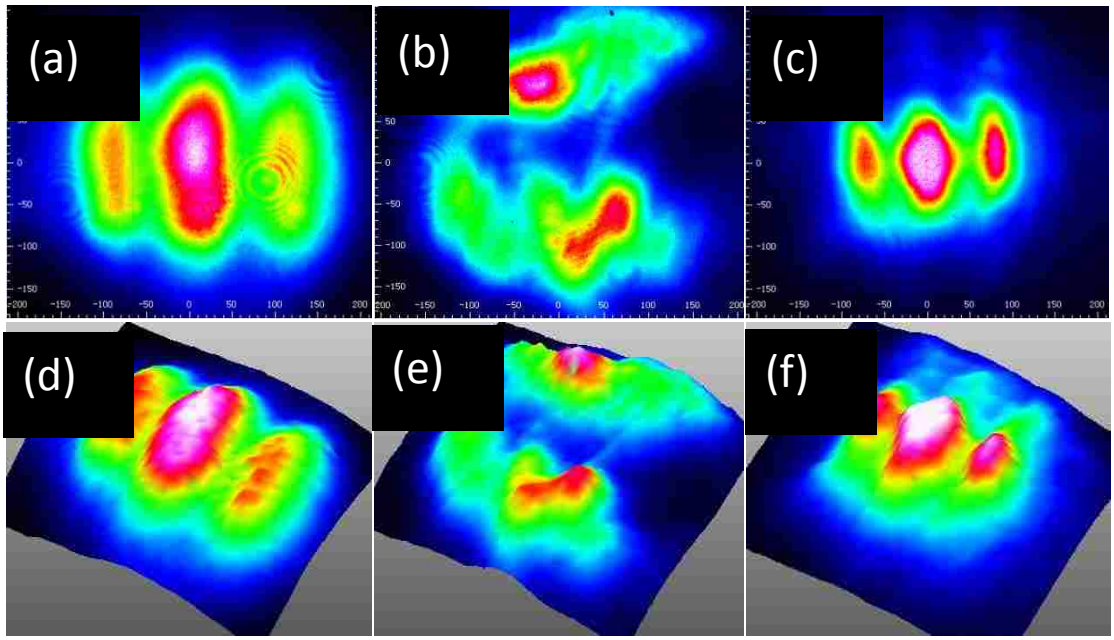

Fig. 3.27. Image recovery by phase conjugation from bulk KTP crystal at pump wavelength of 539.5 nm. (a) Original image generated by *p*-polarized input beam without phase distortion, and (b) distorted image, (c) reconstructed image by *s*-polarized phase conjugated beam. (d), (e) and (f) are the corresponding 3-D images.

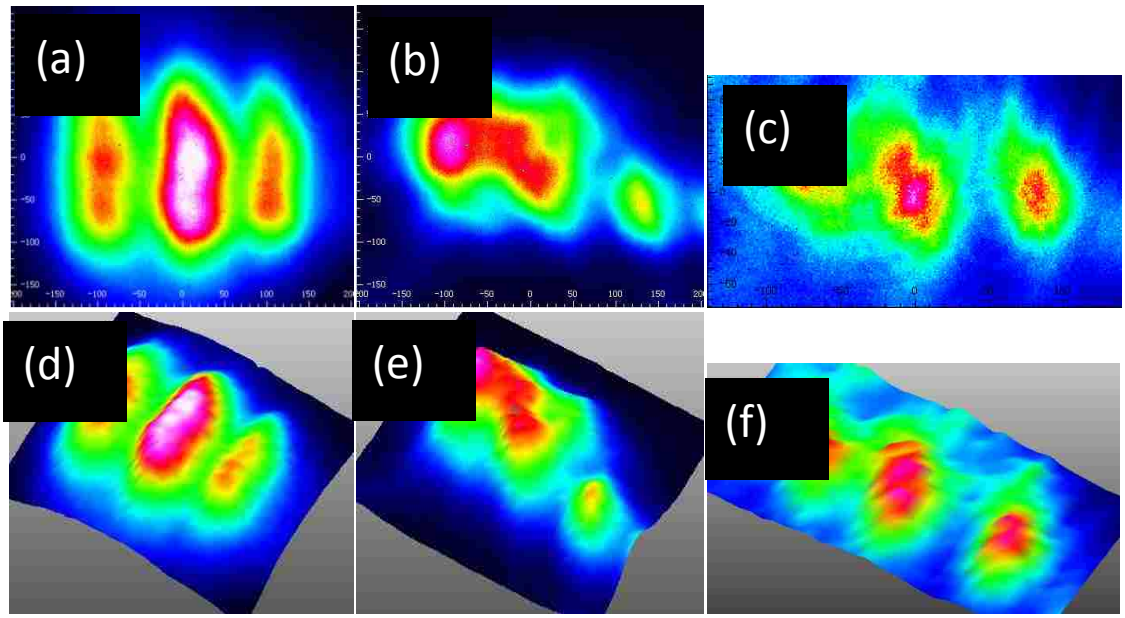

Fig.3.28. Image recovery by phase conjugation from bulk KTP crystal at pump wavelength of 539.5 nm. (a) Original image generated by *s*-polarized input beam without phase distortion, and (b) distorted image, (c) reconstructed image by *p*-polarized phase conjugated beam. (d), (e) and (f) are the corresponding 3-D images.

3.4.2.2 Image Restoration in Dynamic Atmospheric Turbulence

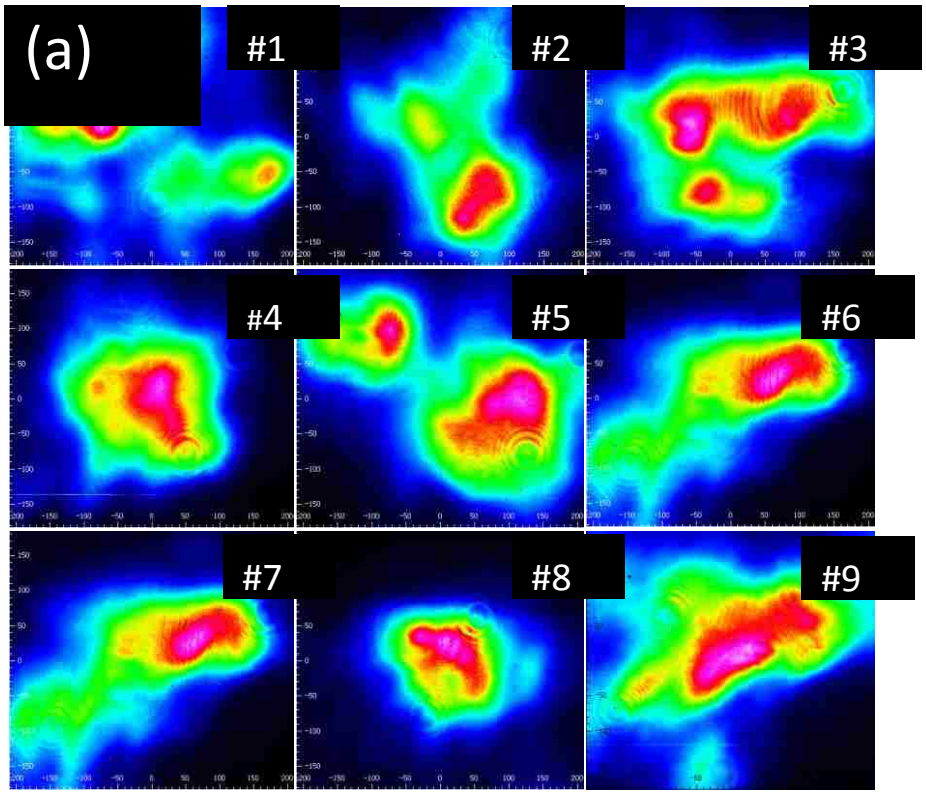

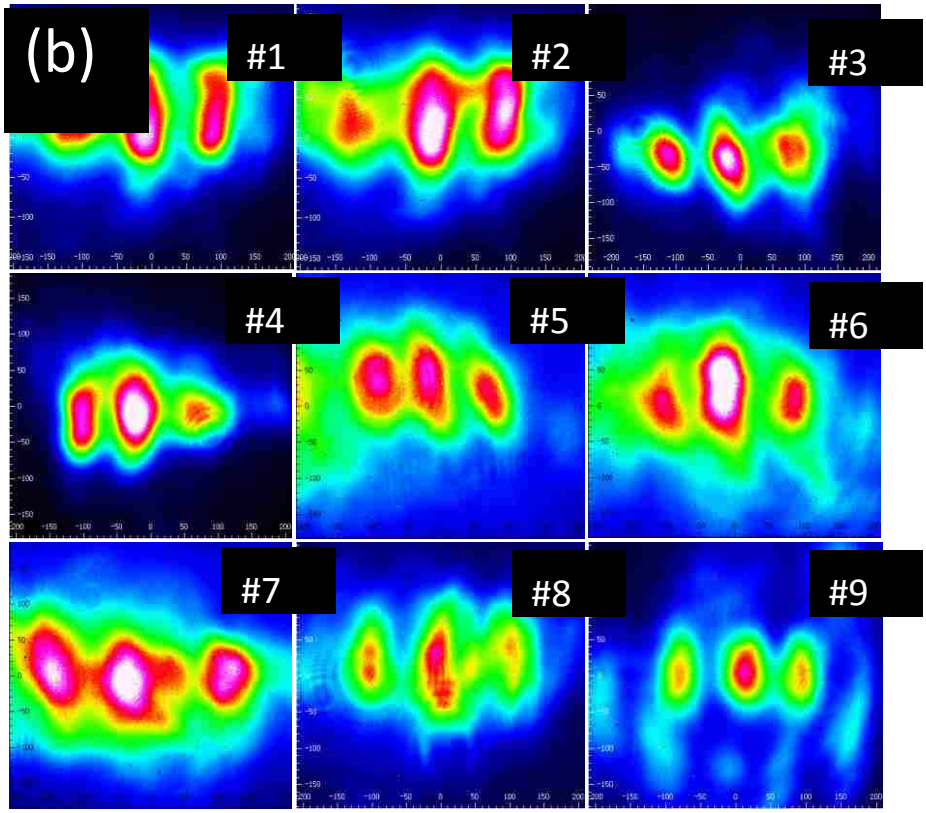

Fig. 3.29 demonstrates real-time image restoration by phase conjugated beam from bulk KTP. The dynamic atmospheric turbulence is mimicked by random rotation of phase plate in idler input beam path. The images are completely distorted and recorded at nine different positions of phase plate [Fig. 3.29(a)], no object information can be collected. *S*-polarized phase conjugated beam eliminates phase distortion and restores information of object. Fig. 3.29(b) illustrates that pattern of restored images is similar to that of original images. In each reconstructed image, three vertical lobes are spatially separated.

3.4.3 Polarization-Insensitive Image Restoration Achieved by Phase Conjugation from AFB-KTP

In order to study polarization-insensitive image restoration, pump wavelength is tuned from 535 nm to 542 nm [Fig. 3.30(a)], wavelengths of signals and idlers generated from AFB-KTP composite as a function of pump wavelengths are measured. We here also demonstrate the spectra of *s*-polarized and *p*-polarized phase conjugated beam at 540 nm pump [Fig. 3.30(b)]. Polarization-insensitive restoration of image blurred by atmospheric turbulence is achieved through AFB-KTP composite. At 540 nm pump, the wavelength of idler is measured to be 1077.8 nm, and its polarization can be tuned by a half-wave plate. Fig. 3.31(a) and 3.32(a) are the original images formed by *p*-polarized and *s*-polarized idler input beam. The images are severely distorted after idler input beams propagate through atmospheric turbulence [Fig. 3.31(c) and 3.32(c)]. Not only the blurred image formed [Fig. 3.31(c)] by *p*-polarized idler input beam can be cleaned up by *s*-polarized phase conjugated beam at 1077.8 nm and 1087.9 nm, as shown in Fig. 3.31(e)-(h), but also distorted image generated by *s*-

polarized idler input beam [Fig. 3.32(c)] is reconstructed by *p*-polarized phase conjugated beam at 1071.9 nm and 1082.1 nm, as demonstrated in Fig. 3.32(e)-(g).

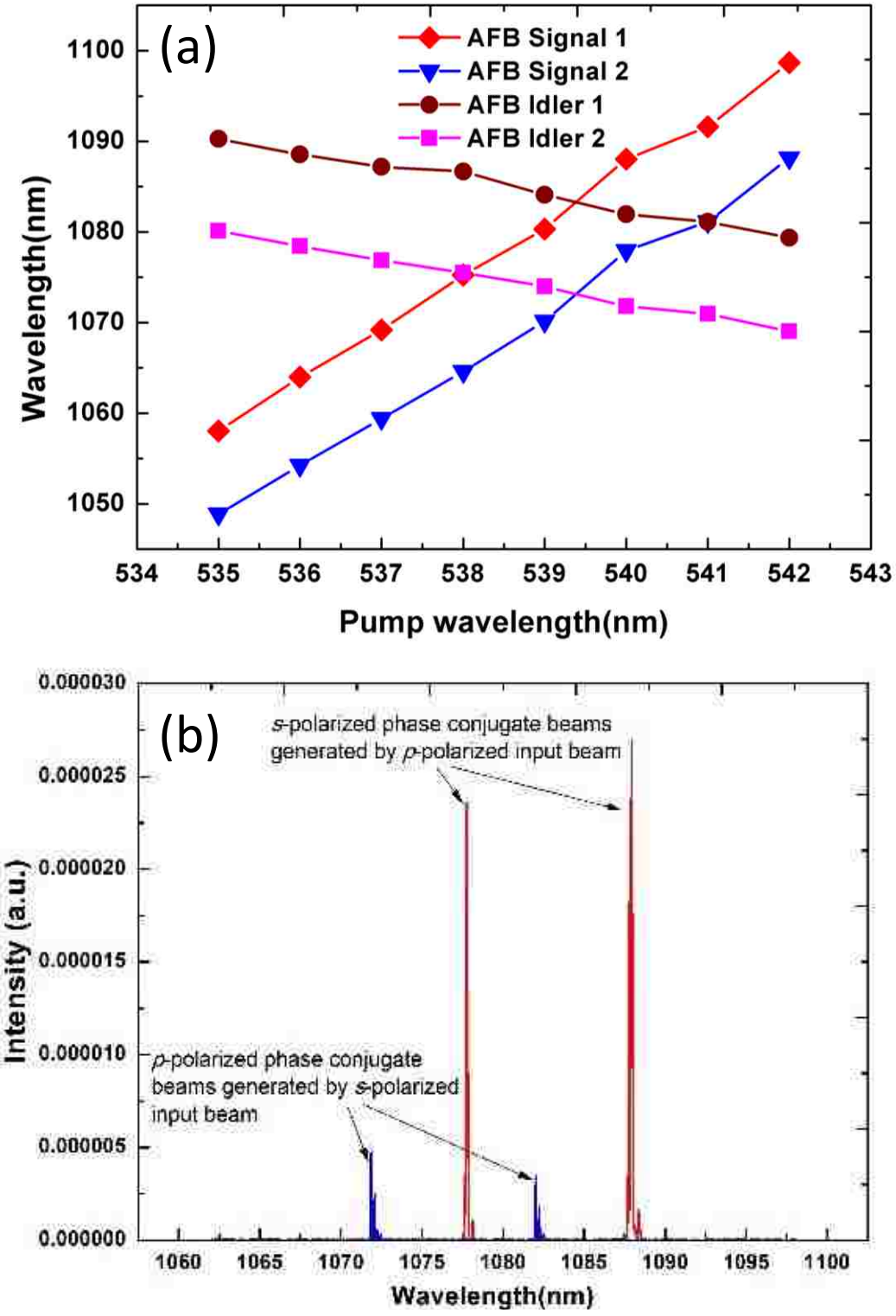

Fig. 3.30. (a) Wavelength of signals and idlers generated from AFB-KTP composite versus pump wavelength. (b) Spectra of *p*-polarized and *s*-polarized phase conjugated beams at pump wavelength of 540 nm.

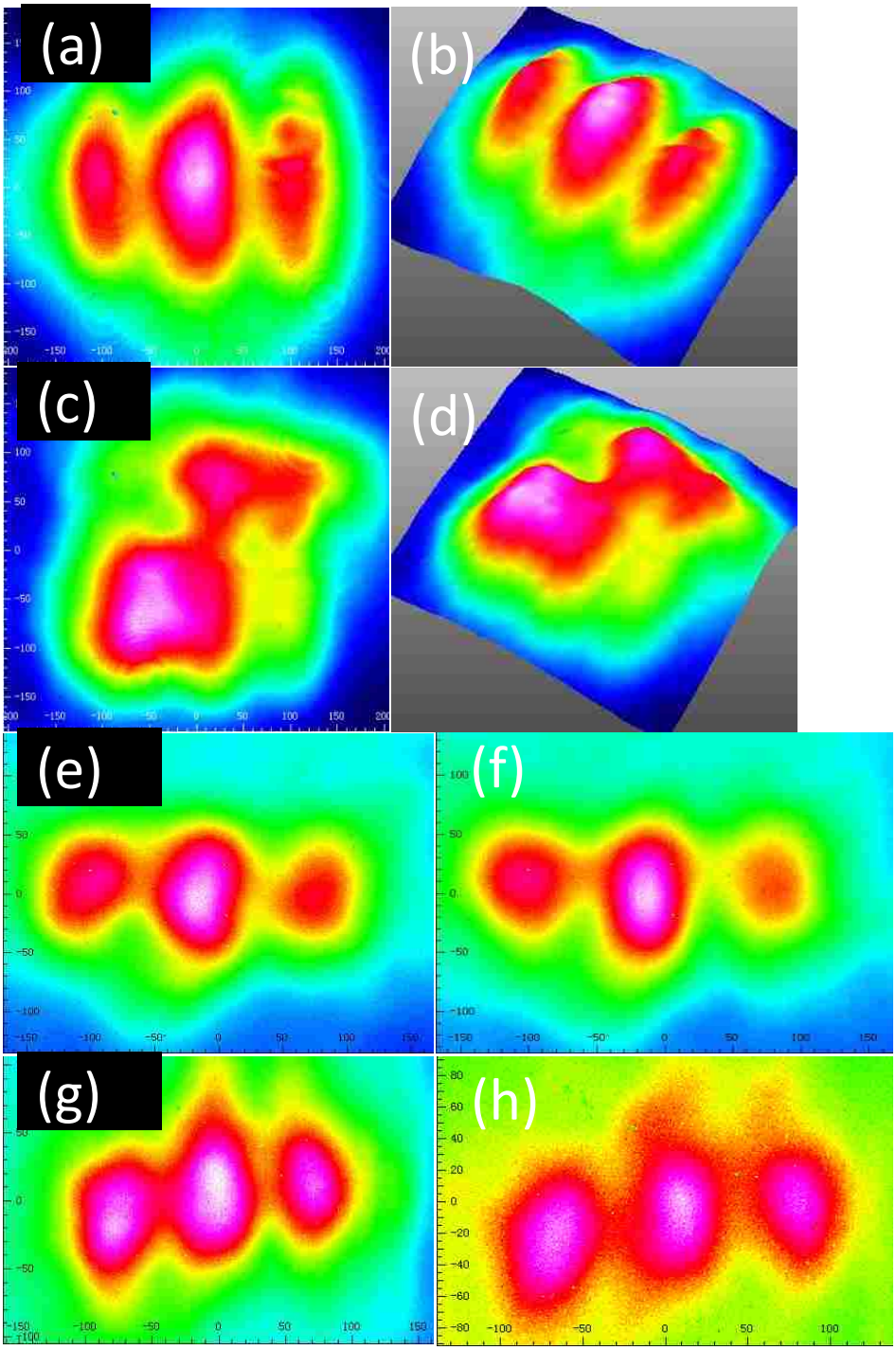

Fig. 3.31. Polarization-insensitive image restoration by phase conjugation. (a) 2-D and (b) 3-D original image generated by *p*-polarized idler input without wave front distortion; (c) 2-D and (d) 3-D distorted image; (e)-(h), recovered images by *s*-polarized phase conjugated beams at degenerate point of 540 nm pump.

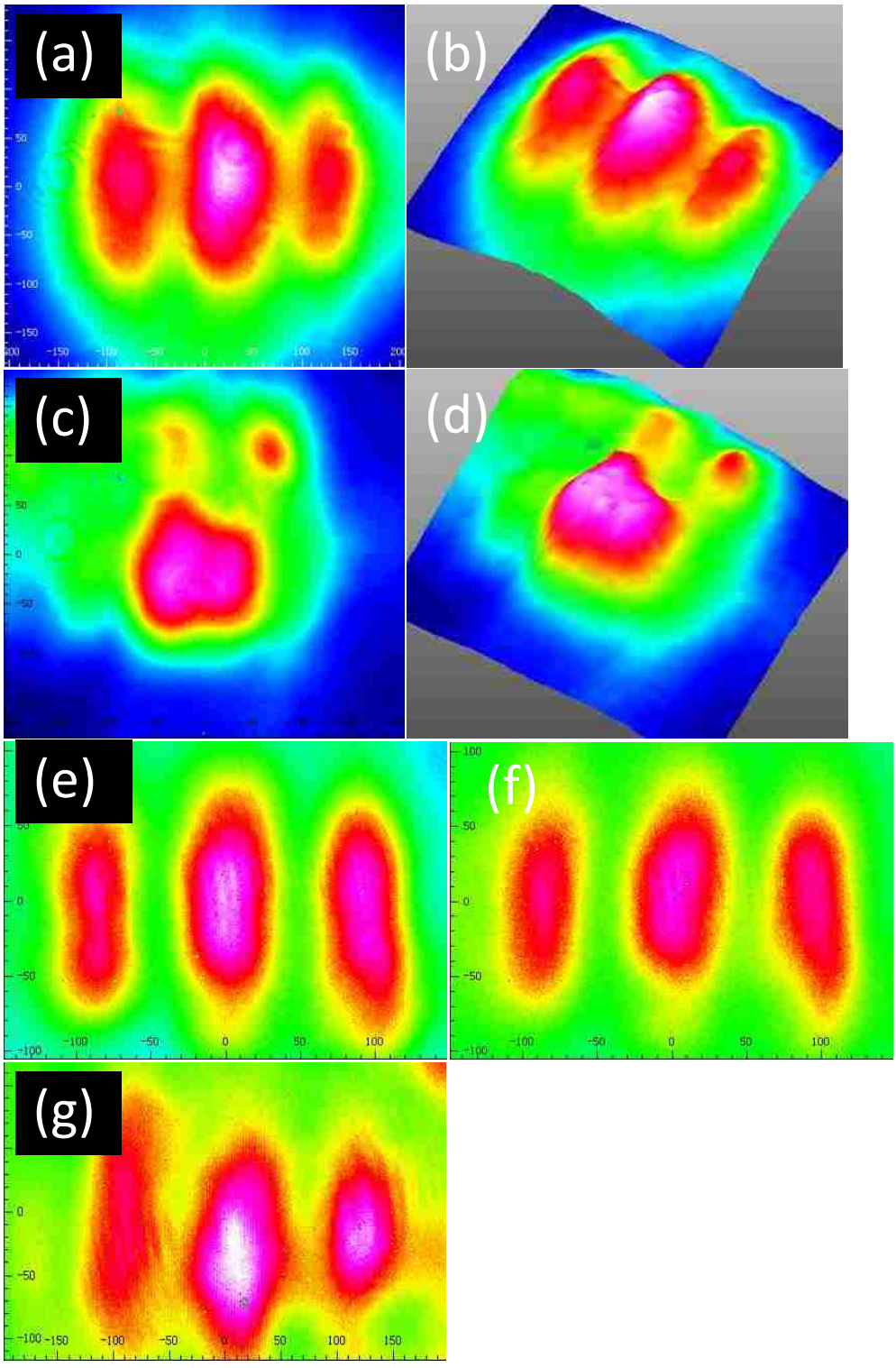

Fig. 3.32. Polarization-insensitive image restoration by phase conjugation. (a) 2-D and (b) 3-D original image generated by *s*-polarized idler input without wave front distortion; (c) 2-D and (d) 3-D distorted image; (e)-(g), recovered images by *p*-polarized phase conjugated beams at degenerate point of 540 nm pump.

Fig. 3.33 shows that polarization-insensitive image restoration is also realized at nondegenerate point of 542 nm. Similar to the case with 540 nm pump, the phase distortion is effectively removed by *s*-polarized [Fig. 3.33(c)] and *p*-polarized [Fig. 3.33(f)] phase conjugated beams.

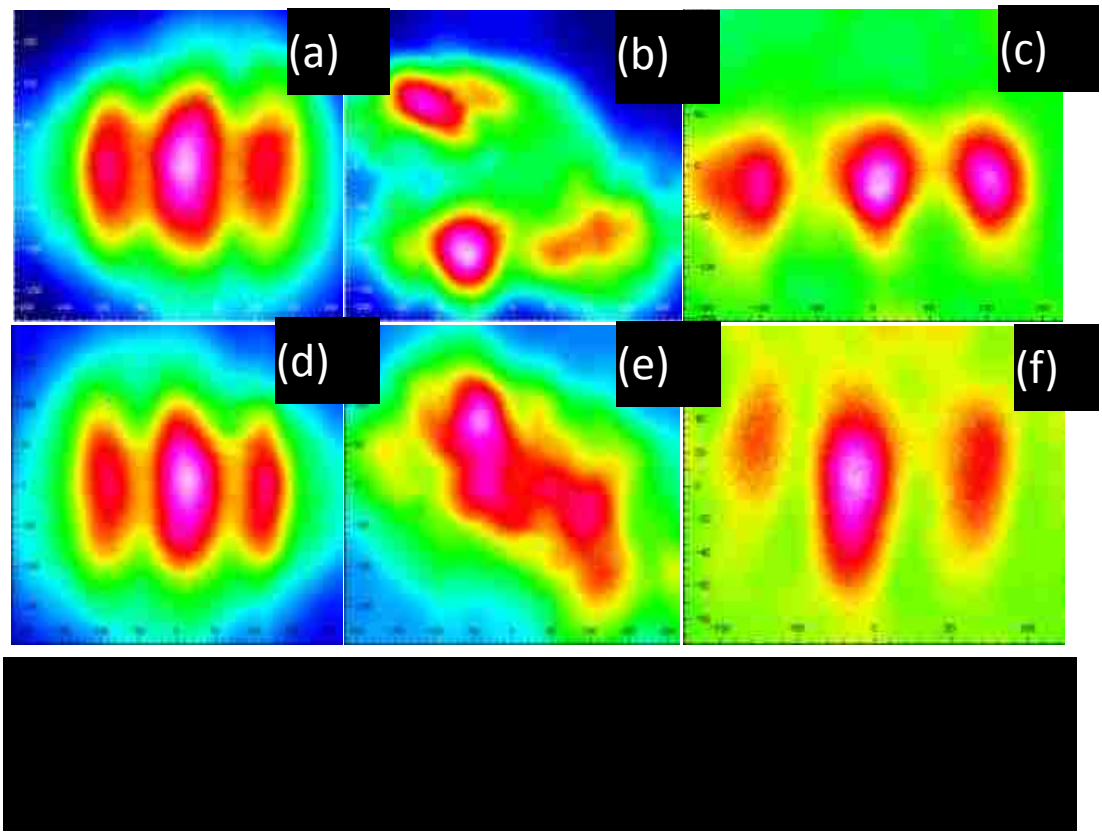

3.4.4 Technical Considerations

One of the technical considerations for the experiments is the background noise from the idler input beam. In order to reduce background noise and increase the contrast of images, usually we introduce a titled angle between pump beam and idler input beam. The image can be restored when idler input beam and pump beam are strictly spatially overlapped, however, there are strong background noise [Fig. 3.34(a)]. Such strong noise can not simply be filtered out by filter. Technically, a very small titled angle is introduced and one can observe the decrease of background noise around vertical bars [Fig. 3.34(b)]. The fine image contrast can be got when optimal tilted angle is reached, in such case, the phase matching condition is still satisfied for generation of phase conjugation. If we continue to

increase the angle to a critical point (~3 ° is estimated), the image restoration can not be achieved since phase matching condition is not satisfied any more.

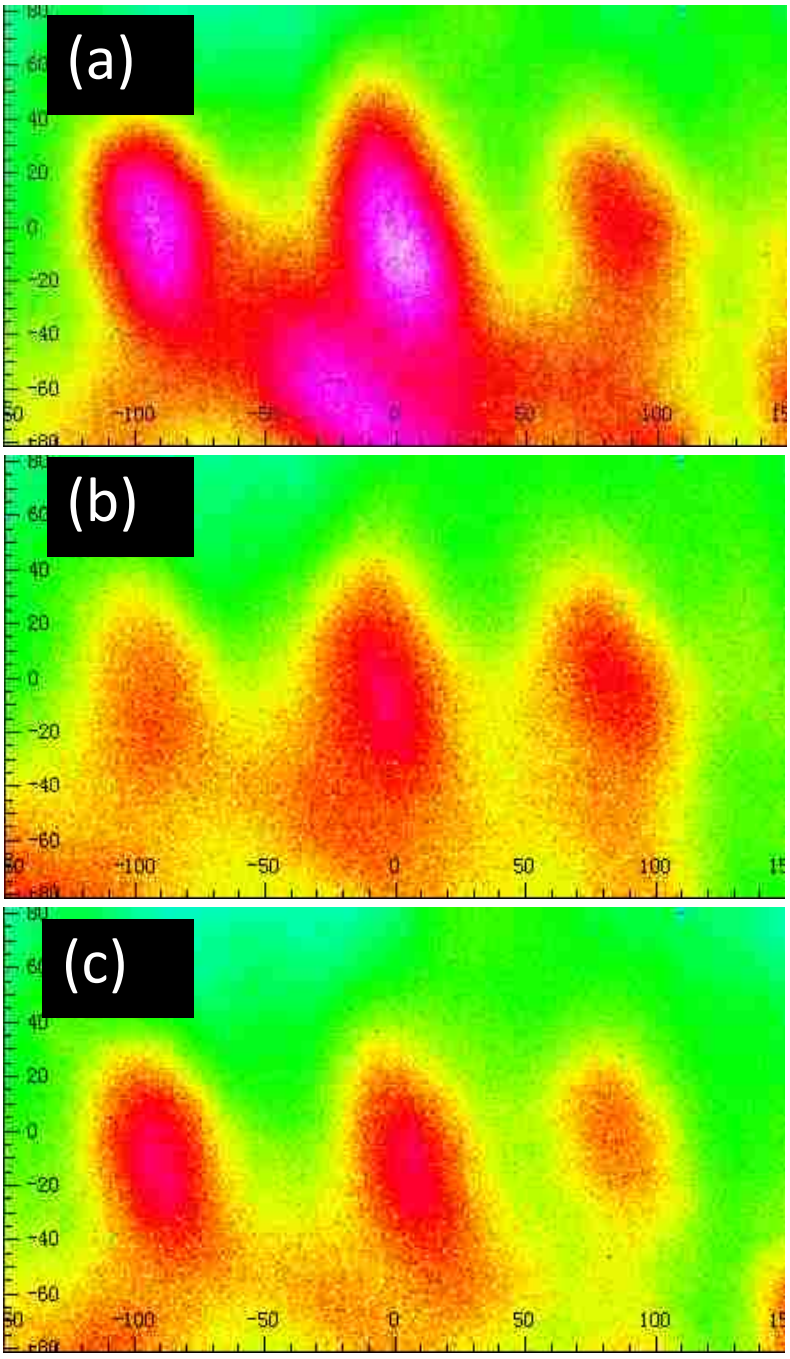

Fig. 3.34. Demonstration of removing background noise in recovered image by tilting the angle between idler input beam and phase conjugated beam. (a) The initial image with strong background noise, (b) the image with improved resolution and (c) the image with optimal resolution.

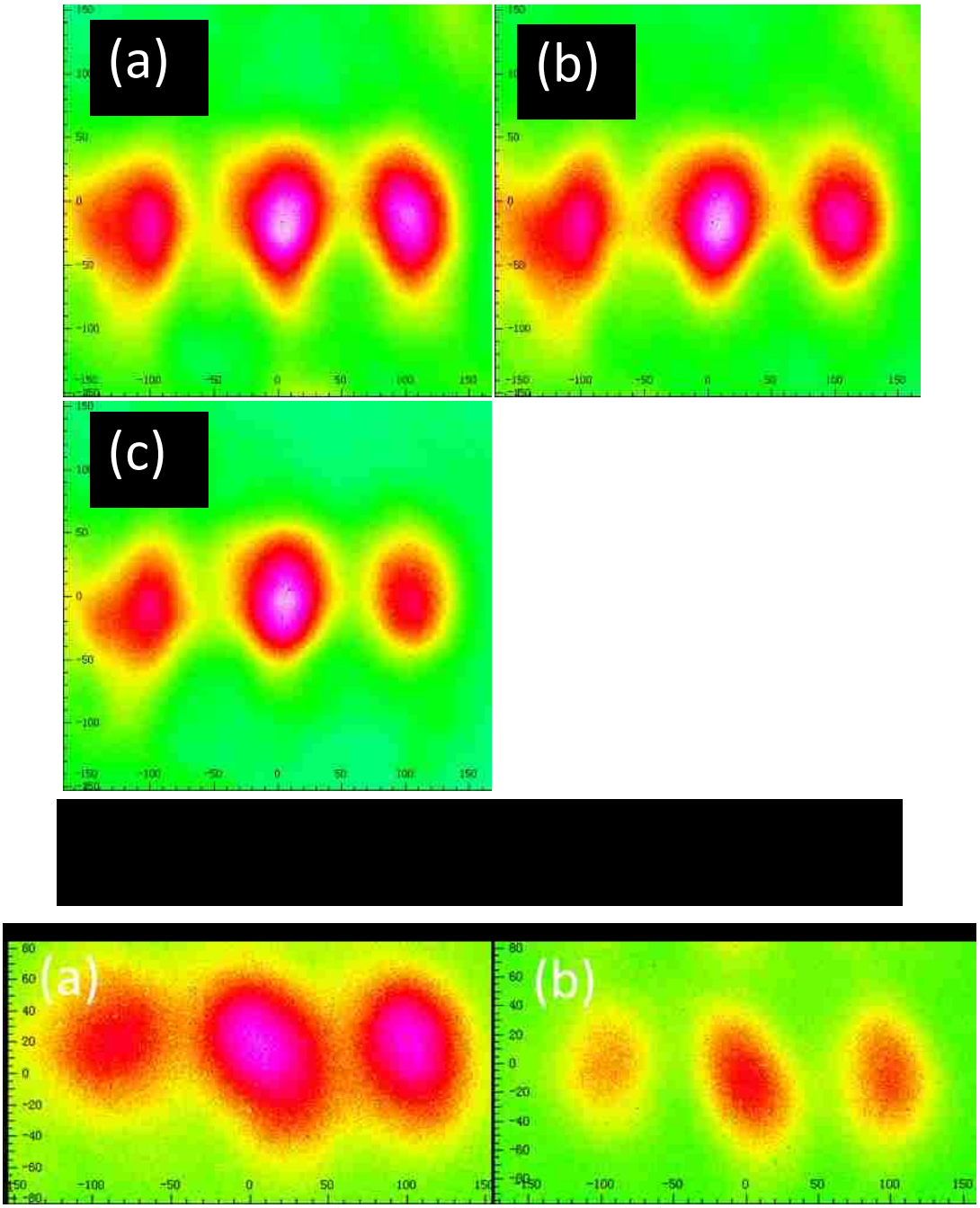

Fig. 3.36. (a) &(b) Recovered images recorded at two different duration positions of laser pulse.

The stability of recovered images is demonstrated in Fig. 3.35. The images are recorded at three consequent pulse peaks. The resolution of images is maintained and object information is clearly contained in each image, so we can conclude that our imaging system is reliable. But for each laser pulse, the contrast of image is going to become weak when the pulse peak passes, which is

demonstrated in Fig. 3.36. Fig. 3.36(a) is recorded at pulse peak position, while Fig. 3.36(b) is captured at the position of around the middle of two pulse peaks. The restored images switch between on and off and are captured by CCD camera, so CW laser source can be adopted for demonstration of continuous reconstruction of blurred images in the future.

Chapter 4 THz Waves from Difference Frequency Generation

4.1 Background of Study

The frequency band of THz wave (1 THz = 10^{12} Hz) is between microwave and Infrared wave, as shown in Fig. 4.1 [70]. It has many applications in imaging Radar [71], chemical sensing [72], bio spectroscopy for genetic [73, 74] and nondestructive testing of composites [75], so there is a great deal of interest in developing THz source. Various methods have been proposed, such as optical rectification [76], quantum cascade laser [77], difference frequency generation (DFG) by mixing two beams [3, 78].

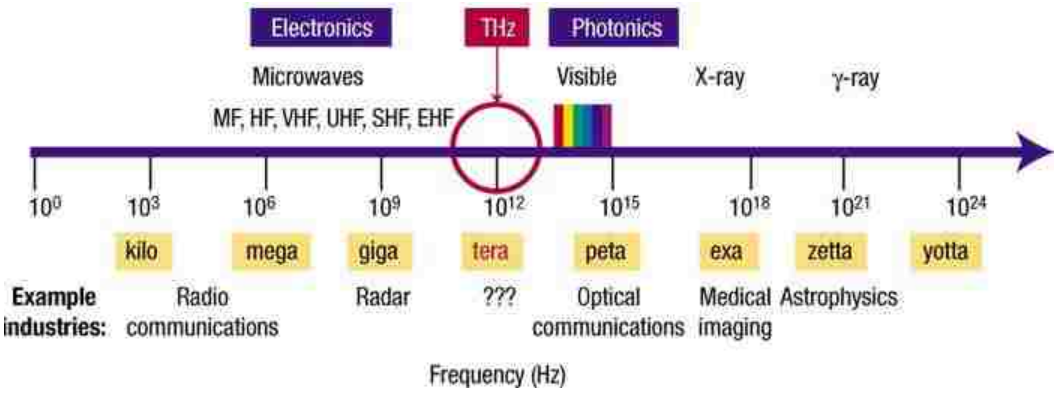

DFG is a very important approach in THz generation, in order to get high THz output power, one should consider the following factors in designing experiments [1]: Using high d_{ij} Elements of nonlinear crystal; Phase matching or quasi-phase matching condition should be satisfied, since it will make sure that the THz, signal and idler beams are spatially accumulated during resonance in OPO, which is similar to phased antenna array; Also the nonlinear materials for generating THz waves should owe low absorption in THz region.

Here I would like to mention that quasi-phase matching is a key consideration in THz generation. Phase matching condition for sure can be achieved by birefringence and polariton resonance. However, it is not flexible, since frequency tuning is desired for the potential utilization, which is usually achieved by tuning pump wavelength or rotation of crystal angle. In practical experiment, quasi-phase matching condition is preferred, which can be expressed as:

$$k_{opt,1} - k_{opt,2} \pm k_{THz} = \pm \frac{2\pi}{\Lambda} m \quad (1) \qquad (1)$$

Where Λ is the periodical domain for providing additional term for QPM. Periodical domain can be introduced by alternatively rotated GaP plates, periodically-poled lithium niobate (PPLN).

Signal and idler beams from OPO have been explored as source in THz generation by DFG. Without seed injection, the OPO initializes from spontaneous emission, resulting large fluctuation in signal and idler beams, and this manifests in frequency spectrum and pulse energy [79]. As we have introduced in Chapter 2, one idler and one signal are coupled out of OPO from quasi-phase matching. Generation of THz wave in Ref. [80] is a specific case for DFG by mixing one idler and one signal. Because the phase of idler and signal is conjugated with each other, THz generated by mixing this pair of signal and idler is sensitive to environmental fluctuation, such as temperature variation, and at the same time, it has large

quantum noise. Differently, idler twins from AFB-KTP composite should show high coherence and theoretically the phase variation for idler twins can always be cancelled in DFG process in nonlinear material, as a result, quantum noise can be suppressed.

In the past, noise reduction and suppression have been studied [81-83], to our best knowledge, the effect of coherent properties of twin idlers beam on THz generation has not been reported yet. We denote signal as $a_s = \bar{a}_s + \delta a_s$, where $\bar{a}_s$ is mean value of signal beam and δa_s is the noise fluctuation factor. Similarly, idler is denoted as $a_i = \bar{a}_i + \delta a_i$. For THz generated by DFG through mixing idler twins beams, the intensity of THz waves can be expressed as $a_{THz} = (\bar{a}_{i1} + \delta a_{i1})(\bar{a}_{i2} + \delta a_{i2})^*$, so that its mean value is $\bar{a}_{THz} = \bar{a}_{i1}\bar{a}_{i2}{}^*$, and the corresponding noise fluctuation term is $\delta\bar{a}_{THz} = \delta\bar{a}_{i1}\bar{a}_{i2}{}^* + \bar{a}_{i1}\delta\bar{a}_{i2}{}^*$, where we omit the higher order term of $\delta\bar{a}_{i1}\delta\overline{a_{i2}}^*$. For THz waves by mixing signal and idler beams, its mean value can be expressed as $\bar{a}_{THz} = \bar{a}_s\bar{a}_i{}^*$, and the corresponding noise fluctuation term is $\delta\bar{a}_i\bar{a}_s{}^* + \bar{a}_s\delta\bar{a}_i{}^*$.

In study I [84], THz generated in GaSe by mixing idler twins from AFB-KTP composite is ultrastable when the temperature of bulk KTP is tuned. This is caused by mutual coherence of idler twins in compensating the variation of intensity and phase. In study II [85], we investigate THz output from mixing idler twins from AFB-KTP composite in GaP. Compared with THz waves generated from mixing signal-idler beams, high coherence of twin idlers demonstrates in enhancement of THz output power and narrowing linewidth. From our theoretical analysis, this is driven by reduction of quantum noise for idler twins, compared with signal-idler beams from bulk KTP based OPO. Finally, the unique patterns of Azimuthal angle dependence of THz output power are demonstrated.

4.2 Generation of Multiple Frequency THz from Coupled KTP OPO

4.2.1 Experimental Setup

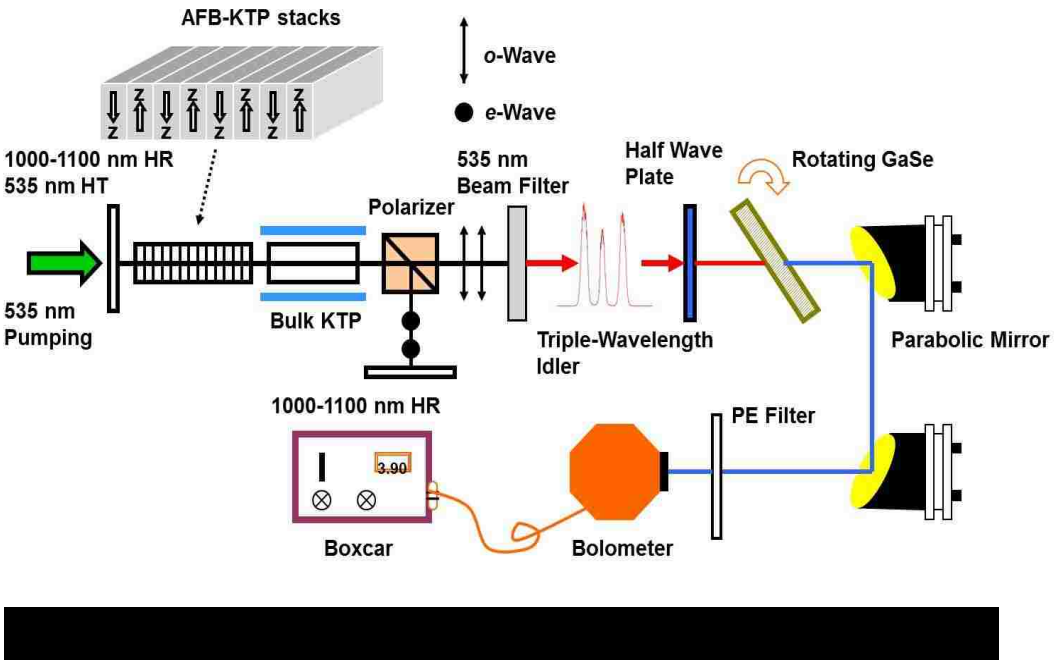

The experimental setup is demonstrated in Fig. 4.2. For generation of triple idler beams, setup of coupled OPO is similar to that in Chapter 2. Differently, in this experiment, the bulk KTP is placed in an oven, in which temperature of bulk KTP can be tuned. The triple waves consist of idler twins from AFB-KTP and one idler from bulk KTP in coupled KTP OPO, and they are all parallel polarized. In order to generate THz waves, a half wave plate is placed in front of GaSe to adjust polarization of idlers input. THz waves generated are focused by two parabolic mirrors and directed to a bolometer. The residual 1 μm pump beam is filtered out by PE filter. In order to study the THz wave intensity of Azimuthal dependence, the Azimuthal angle of GaSe is continuously tuned by galvano scanner.

4.2.2 Results and Discussions

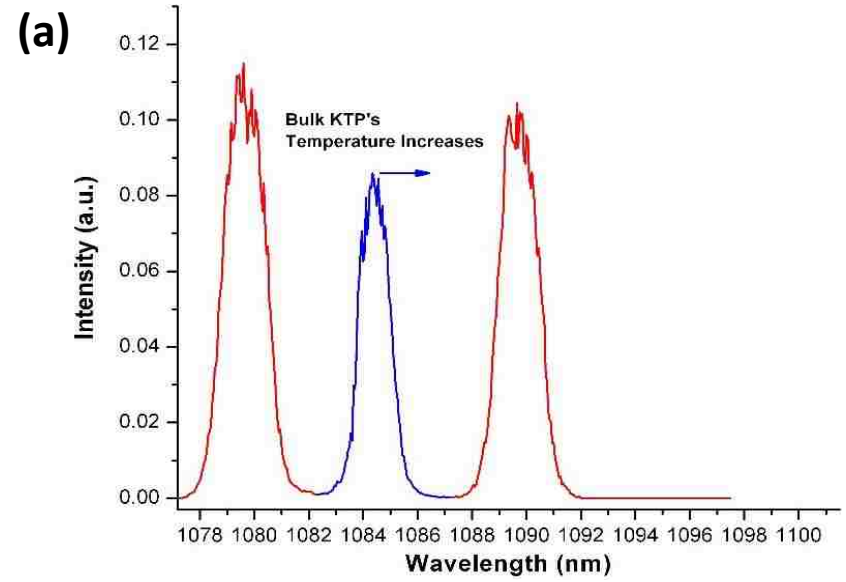

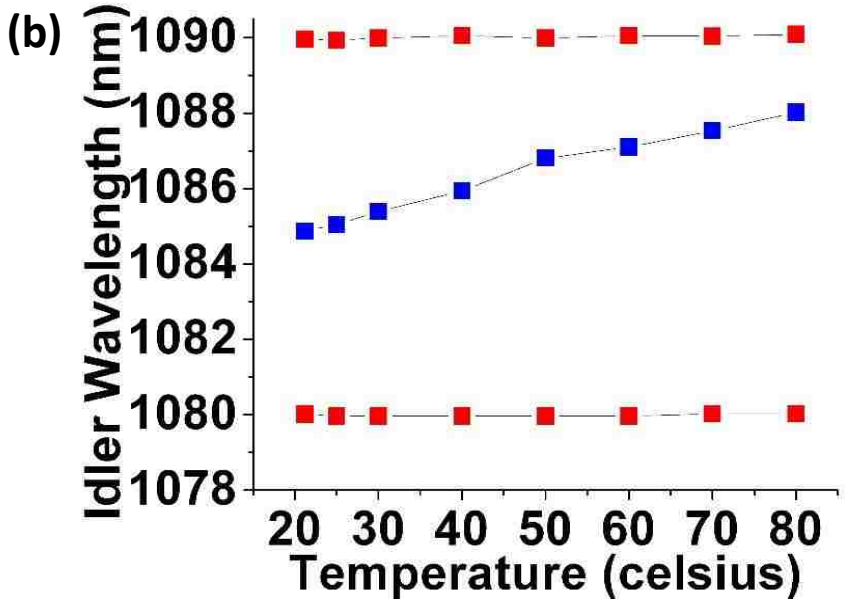

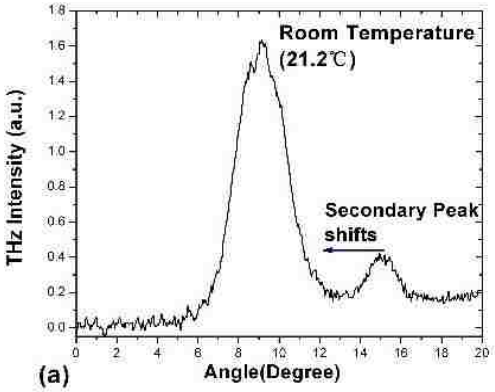
Room Temperature
(21.2℃)
Secondary Peak
shifts
THz Intensity (a.u.)
Angle(Degree)
(a)

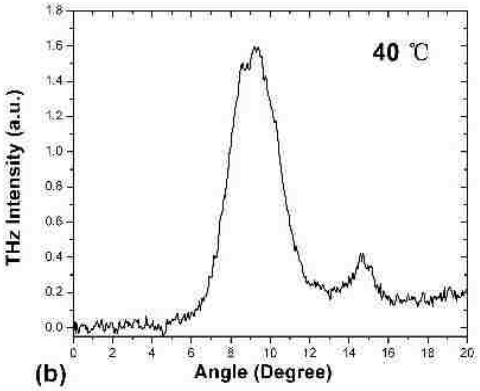
40 ℃
THz Intensity (a.u.)
Angle (Degree)
(b)

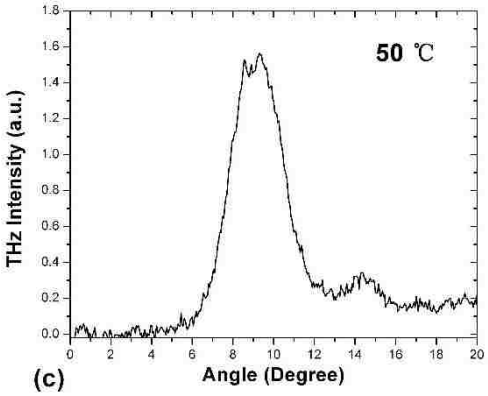
50 ℃
THz Intensity (a.u.)
Angle (Degree)
(c)

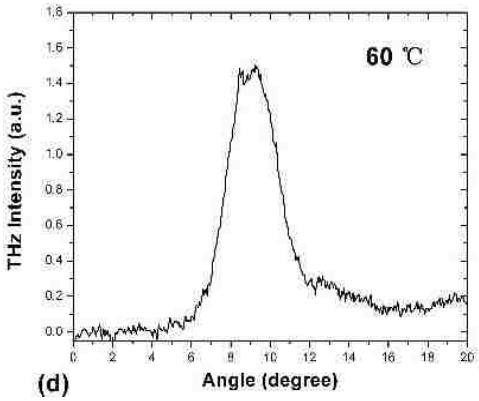
60 ℃
THz Intensity (a.u.)
Angle (degree)
(d)

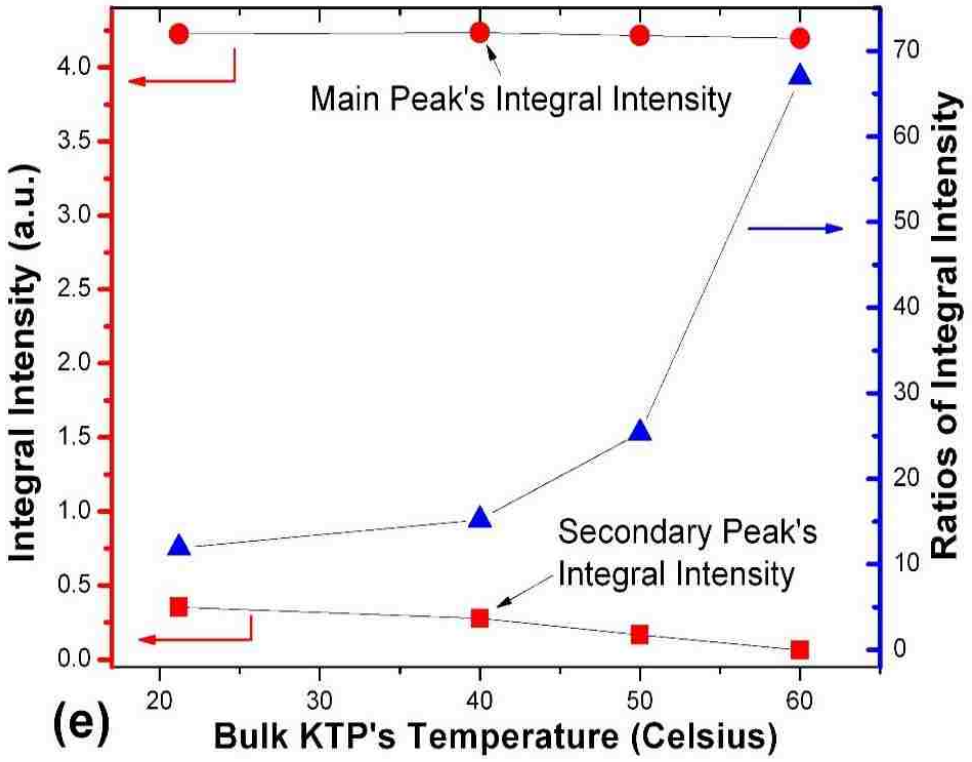
Main Peak's Integral Intensity
Secondary Peak's
Integral Intensity
Integral Intensity (a.u.)
Ratios of Integral Intensity
Bulk KTP's Temperature (Celsius)
(e)

The spectra of triple wavelength idlers generated from coupled OPO are shown in Fig. 4.3 (a). The wavelengths of twin idlers from AFB-KTP composite are 1080.01 nm (idler 2) and 1089.96 nm (idler 1), and wavelength of idler from bulk KTP is nearly in the middle of these twin idlers, since idler twins beams are degenerated from single idler by QPM, and it is determined to be 1084.87 nm. We also observe that the intensity of idler from bulk KTP is relatively weaker than that of idler twins, which would be caused by phase matching condition affecting beam conversion efficiency. We increase the temperature of bulk KTP from room temperature to 80 Celsius degree, the idler peak from bulk KTP shifts to high wavelength region [Fig. 4.3(b)], while the wavelength of twin idlers is fixed.

When bulk KTP is at room temperature, we measure the spectra of THz and two THz peaks at 2.54 THz and 1.24 THz are determined. The main peak at 2.54 THz is generated from mixing idler twins and secondary peak is from mixing idler from bulk KTP and idler(s) from AFB-KTP composite. We increase the temperature of bulk KTP and measure the corresponding THz spectra, as shown in Fig. 4.4 (b)-(d). These spectra show there are only two THz wavelength generated, and the secondary peak is generated by DFG of idler from bulk KTP and idler 1 from AFB-KTP composite. Third peak by mixing idler from bulk KTP and idler 2 is not observed, it is believed that this pair of idlers does not satisfy the phase matching condition in GaSe for efficient THz generation. As temperature of bulk KTP increases, the secondary peak shifts to the position of main peak, which indicates that it is generated from mixing idler 1 and idler from bulk KTP. At room temperature, compared with secondary peak, there is an enhancement factor of 12 for integrated THz power for main peak. Due to coherent property of idler twins, the main peak demonstrates ultrastability in THz generation. Even when the temperature of AFB-KTP is tuned, the variation to intensity and phase of idler twins is the same and can be cancelled in DFG. In contrast,

secondary peak generated from mixing idler 1 and idler from bulk KTP is very sensitive to temperature fluctuation, since this pair of idlers does not compensate with each other to the change of temperature. The variation for secondary peak is around 6% in THz intensity per unit temperature, while for main peak, it is negligible and few magnitude orders lower.

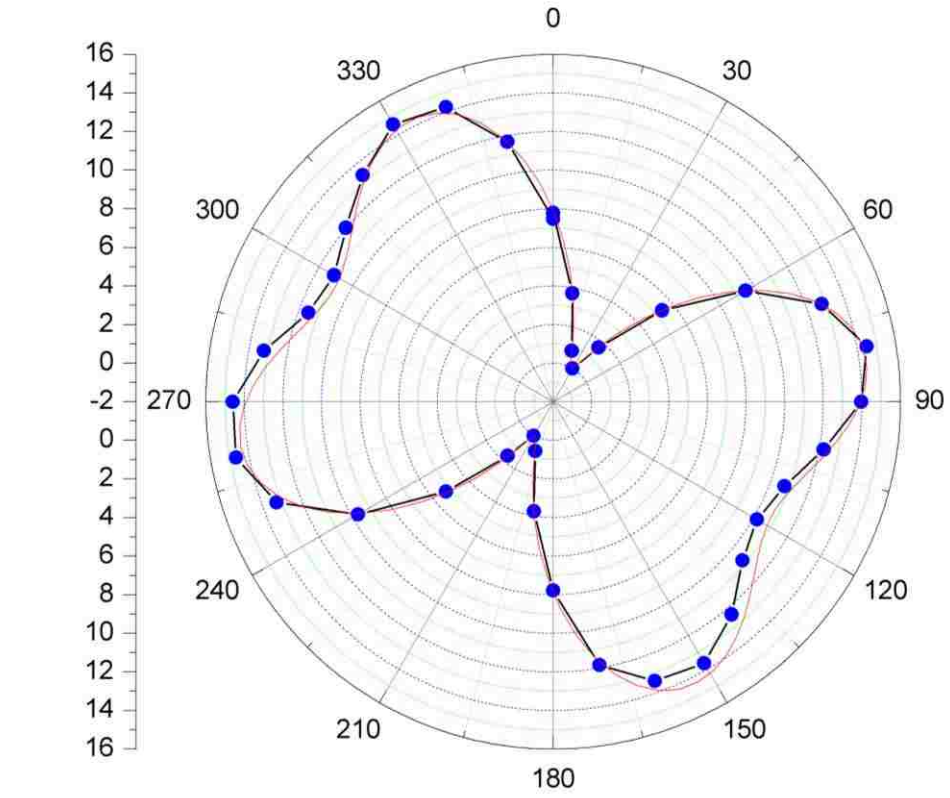

4.3 Theoretical Study on Effect of Coherence between Idler Twins in THz Generation

4.3.1 Noise Reduction in THz Waves Generated from Idler Twins of AFB-KTP

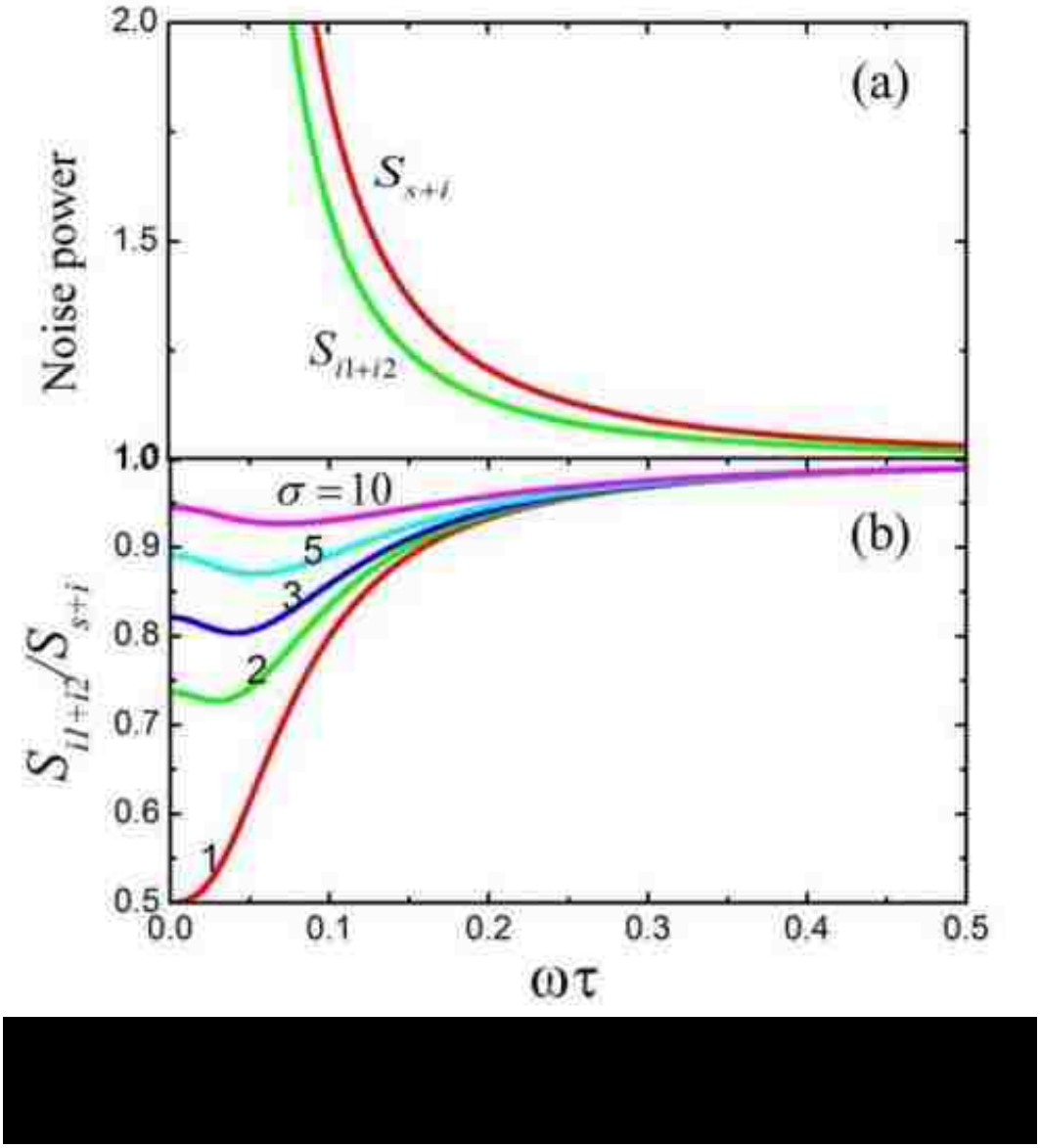

In this part, we analyze the noise spectra of THz waves generated by DFG from mixing idler twins and signal-idler by semi-classical methods [82, 86, 87]. The noise spectra from signal-idler mixing and idler-idler mixing can be deduced from coupled equations as:

$$S_{s+i} = \frac{T_0 T' T(\sigma-1)+T' T+\omega^2\tau^2}{\omega^2\tau^2} \quad (2)$$

$$S_{i+i} = \frac{T_0 T' T(\sigma-1)+T' T+\omega^2\tau^2}{\omega^2\tau^2} - \frac{T'^3 T+2TT'\omega^2\tau^2}{2\omega^2\tau^2(\omega^2\tau^2+T'^2)} \quad (3)$$

Where $\sigma = \sqrt{\frac{P}{P_0}}$, P is the pump power and P_0 is the threshold power of OPO; ω is the frequency and τ is the cavity round trip time. T_0, T and T' is the cavity parameter, and they are 0.9, 0.05 and 0.06 respectively.

Different from the expression of noise spectra of signal-idler mixing, there are two terms for idler-idler beams mixing: the first term is the same one with noise power spectra of signal-idler mixing, and the additional term is determined by parameter of OPO cavity and frequency of beams. It is worth mentioning that the first term is dedicated by pump power factor $\sigma = \sqrt{\frac{P}{P_0}}$ under the condition that cavity parameters and pump beam are fixed.

Fig. 4.6(a) shows the noise spectra of THz waves generated from mixing signal-idler and idler-idler beams. The noise of THz waves by mixing idler-idler is lower than that of mixing signal-idler beams by DFG in GaP. With a fixed pump power, these two noise spectra demonstrate similar tendency with the increase of ωτ. When the frequency of beams increases, noise spectra of THz from mixing signal-idler and idler-idler become close with each other, as shown in Fig. 4.6[a]. This is obvious from the second term in expression of S_{i+i}, since at large ωτ, it will become to be zero. This result is consistent with the discussion in Ref. [83], phase diffusion will build up a coherent part in output beams and it has a trend to destroy squeezing at low frequency. Fig. 4.6(b) illustrates the normalized

noise spectra S_{i1+i2}/S_{s+i} as a function of pump power. With a fixed frequency ω and at low pump power (σ=1), the normalization value can be 50%. When the pump power increases, normalized spectra decrease correspondingly. Similar in Fig. 4.6(a), as ωτ goes larger, normalized noise spectra approaches 1.

In this project, we observe the THz output power from mixing idler-idler is one order magnitude higher than that of signal-idler mixing. Such power enhancement is caused by quantum noise reduction in idler-idler mixing in DFG. In order to rule out the possibility of being affected by pump power intensity, the same 1 μm pump power is used for generating signal-idler beams from conventional KTP OPO and idler-idler beams from AFB-KTP based OPO. The calculated experimental value of ratio for $|P_{THz}^{i+i}|_{max}/|P_{THz}^{s+i}|_{max}$ is 1.3 times of theoretical value.

Furthermore, linewidth of THz waves from signal-idler mixing and idler-idler mixing is measured. The linewidth of THz waves by idler-idler mixing is not only much narrower than that of signal-idler mixing, but also the theoretical value. The linewidth narrowing is attributed to the quantum noise reduction in idler-idler mixing.

4.3.2 Dependence of Patterns of THz Waves by DFG on Azimuthal Angle

We also study the THz output power of Azimuthal angle dependence [Fig. 4.7]. The Azimuthal angle dependence for THz from signal-idler mixing [Fig.4.7 (a)] and idler-idler mixing [Fig. 4.7(b)] shows unique features. The patterns are determined by the polarization of pump beams and the nonlinear coefficient tensor of GaP. Since the signal-idler generated from conventional OPO have perpendicular polarizations and idler-idler generated from couple OPO have the same polarization, these two modulated patterns should be different from theory. In Fig. 4.7, the blue dot is the experimental data and it is consistent with the theoretical fitting (in red line), the signal-idler pattern is theoretical fitted by $P_{THz}^{s+i} \propto 1 + 3cos^2(2\varphi_1)$, while idler-idler is fitted by $P_{THz}^{i+i} \propto 4sin^2(2\varphi_1) + 4cos^4(\varphi_1)$. The Azimuthal angle

dependence of THz waves conforms that THz waves are generated from DFG process in GaP.

The above discussion shows that the idler twins from coupled OPO are highly coherent. The enhancement of output power and linewidth narrowing of THz waves are caused by reduction of quantum noise between these idler twins.

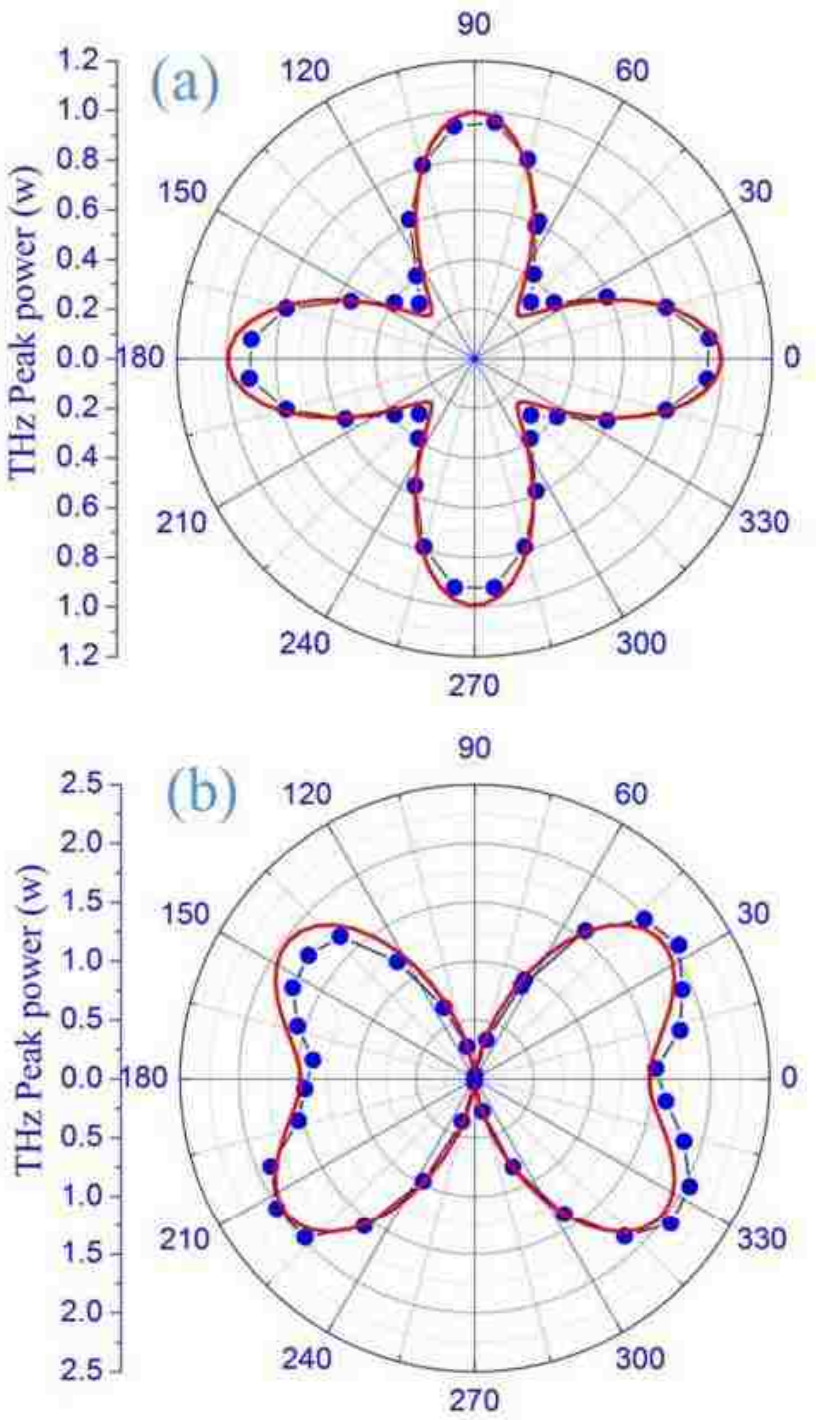

Fig. 4.7. Dependence of THz power of (a) signal-idler mixing (b) idler-idler mixing in GaP on Azimuthal angle. Red line is the theoretical fitting of experimental data indicated in blue dot.

Chapter 5 Single Photon Detection

5.1 Background of Investigation

Raman signal is an important tool in identifying properties of material and figuring out the specific contents of materials. It has been widely explored in studying photons in condensed matter materials [88], such as photon decay [89] and generation [90]. It also has been demonstrated in precisely measuring the temperature of crystal [91, 92] and hot photon effect [93, 94]. What is more, single molecule sensitivity has been achieved by coherent anti Stokes signals [95]. The principle of Raman generation is shown in Fig. 5.1. When a pump beam illuminates material, the electrons in low energy level would be excited to unstable higher energy level, they will emit photons when it drops back to lower energy level. If the frequency of emitted photons is higher than that of pump beam, it is the anti-Stokes signals, while frequency of Stokes Raman signals is lower than that of pump beam.

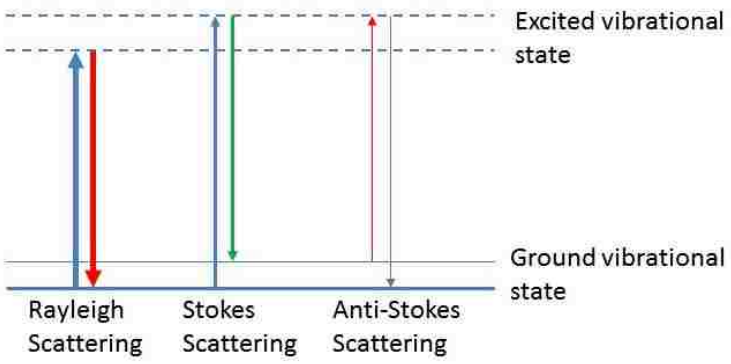

Fig. 5.1. Illustration of process of frequency shifts for Rayleigh scattering, Stokes scattering and anti-Stokes scattering.

There are two main purposes for this project: (a) Using low pump power to excite anti-Stokes Raman signals. Because the electrons occupation of high energy levels is dramatically lower than low energy one, usually high pump power is required to generate anti-Stokes Raman signals. In previous work, anti-Stokes is measurable with around 100 mW pump power, but such high pump power will cause a serious problem in signals' measurement and analysis: local heating effect [88, 96]. When the temperature of crystal increases, the electronic occupation will be adjusted and the measured Raman signals can't accurately interpret the information of material, which manifests in Raman peaks' broadening [97]. (b) Utilization of silicon avalanche photodiode in single photon detection. InGaAs/InP avalanche photodiode has been used in photon number detection. But there are some shortcomings: its large dark count number is as high as 10^3 to 10^4 s^{-1}, its efficiency is as low as around 10% and its long dead time is around 1 μs. In contrast, for silicon avalanche photodiode, its dark count rate is only 25 s^{-1}, and dead time is only around 50 ns. More important, its efficiency can be as high as 70% at the center wavelength of 700 nm. Through using silicon avalanche photodiode, single photon detection sensitivity can be significantly improved within its response region. The process of up conversion of photon in nonlinear crystal can be more exactly interpreted in anti-Stokes Raman signals. One of such similar scheme is shown in Ref. [98], the frequency of input beams can blue-shift to high frequency region, for example, 1.12 μm beams can up-convert to 1.04 μm.

In this project [99], forward and backward anti-Stokes Raman signals generated from lithium niobate waveguide and bulk materials are demonstrated. There is an enhancement factor of 30 for backward anti-Stokes signals from waveguide with 10 μm width, compared with that of bulk material, so for such scheme, we can use very low pump power to excite measurable anti-Stokes

signals with minimum local heating effect. The spectra of backward and forward configurations demonstrate unique features, and reflection of signals from facets of waveguide should be minor factor in spectra measurement. Although generation of Raman signals from lithium niobate has been reported in the past, to our best knowledge, it is the first time to observe unique features of forward and backward anti-Stokes from waveguide and bulk material of lithium niobate.

5.2 Experimental Setup

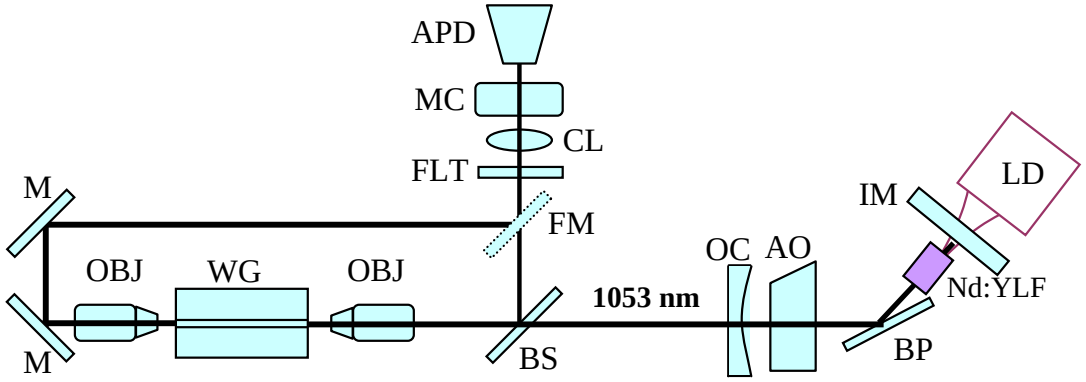

Fig. 5.2. Schematic setup for generation of forward and backward anti-Stokes signals from lithium niobate waveguide or bulk material.

The schematic setup for generating forward and backward anti-Stokes is shown in Fig. 5.2. Pump source is Nd: YLF home-made laser. The dimension of laser crystal Nd: YLF is 4 ×4 ×10 mm^3, it emits two perpendicular polarized beams at 1053 nm and 1047 nm when it is pumped by an 808 nm diode laser. Laser cavity consists of a plano input mirror and a concave output mirror. After inserting a Brewster plate, only 1053 nm fluorescence resonates and couples out of laser cavity, while 1047 nm can't efficiently be generated. Laser system is operated at 5 KHz and the repetition rate is modulated by an acoustic optical modulator in laser cavity. The pulse width is compressed and measured to be 10 ns after Nd:YLF compact laser cavity has been optimized. The input 1053 nm

beam is focused by 20×objective into waveguide or bulk material for anti-Stokes signals generation. 50% beam splitter is used to reflect the backward anti-Stokes signals. For forward anti-Stokes signals detection, two high reflectivity mirrors and a filp mirror are adopted to direct forward signals to measurement part. Before Raman signals are collected by a fiber, the input and signals mixing beams propagate through an edge filter and anti-Stokes signals are selected by a monochromator. Forward and backward anti-Stokes signals are measured by a Si APD. One of the technical considerations is background noise reduction, we conduct the experiments in dark room and the compact Nd:YLF pump laser and signals collection division are arranged into two separated paper boxes to decrease the background noise to minimum.

5.3 Results and Discussions

5.3.1 Enhancement of Anti-Stokes Signals from Lithium Niobate Waveguide

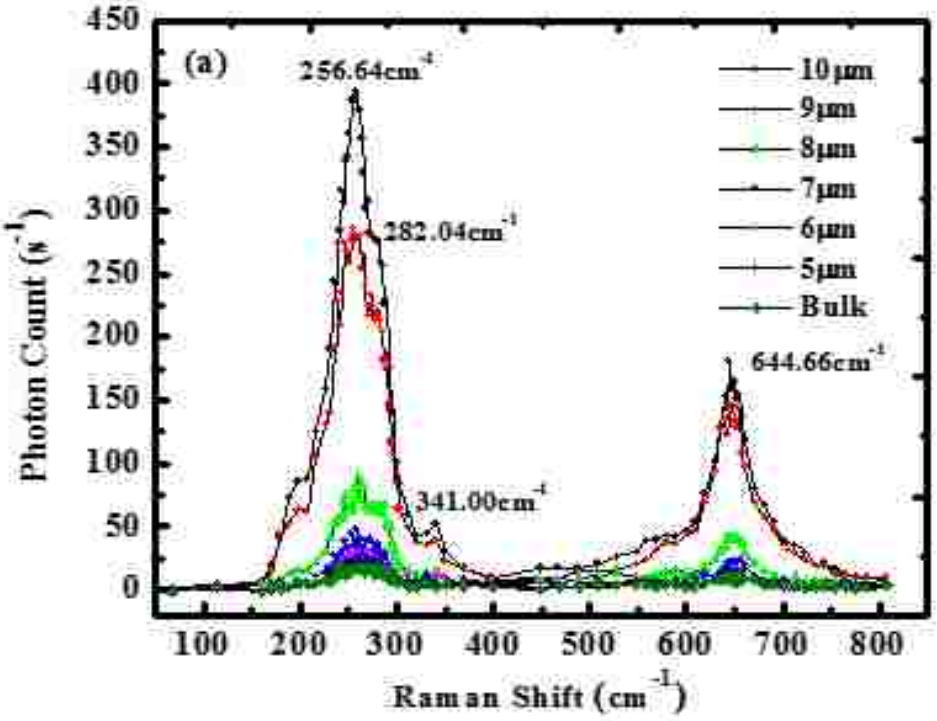

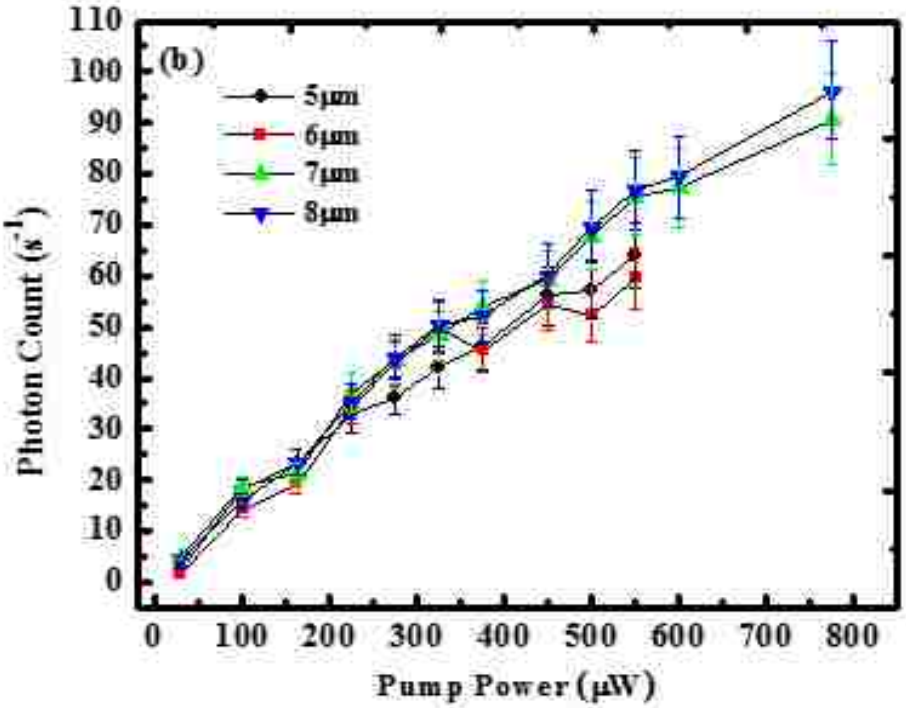

Fig. 5.3. (a) Comparison of photon count of backward anti-Stokes signals among lithium niobate waveguides with different widths and bulk material. (b) Dependence of photon count for lithium niobate waveguides with four different widths on pump power.

For the first part of project, we study the backward anti-Stokes Raman signals from lithium nabiote waveguides with six different widths and bulk material [Fig. 5.3(a)] and dependence of anti-Stokes signals on pump power [Fig. 5.3 (b)]. Ti-diffused lithium nabiote waveguides with widths from 5 μm to 10 μm are used and they are all *x*-cut. The polarization of 1053 nm pump beam is adjusted by a half wave plate before coupling and it is along *z* direction of waveguide. From Fig. 5.3(a), the strongest anti-Stokes signal is generated from lithium niobate waveguide with 10 μm width, there is an enhancement factor of 30 for signal intensity, compared with that of bulk material. Such power enhancement for anti-Stokes signals from waveguide structure is caused by the role of photon accumulation in waveguide after generation. While for bulk material, diffusion will reduce the

photon number being collected. So if 10 μm width waveguide is used, only very low pump power, e.g. 230 nW, is needed to excite measurable anti-Stokes signals. For Ti-diffused lithium niobate waveguide, four Raman peaks at 256.64 cm^{-1}, 282.04 cm^{-1}, 341.00 cm^{-1}, and 644.66 cm^{-1} are identified. They correspond to *E*(TO3) mode, *E*(TO3)+*E*(LO3) combination mode, *E*(LO4) mode, and A_1(TO) mode [100], which indicates that the crystal should be placed in $Y(Z,Z)\bar{Y}$ notation for effective anti-Stokes signals generation [101]. For lithium niobate, optical branches $4A_1$, $5A_2$ and 9*E* are Raman active in phonon branches of $5A_1$, $5A_2$ and 10*E* at a nearly zero wave vector. The main peaks centered in 256 cm^{-1} is much stronger than that of 644.66 cm^{-1}, this is obvious since the number of electron occupation in lower energy level is much more than that of in higher energy level. In Fig. 5.3(b), dependence of intensity of anti-Stokes signals on pump power is studied. At low pump power level (from 30 μW to 350 μW), it demonstrates linear relationship between photon count number and pump power. Starting from 350 μW, it deviates from such linear dependence relationship, which should be caused by local heating effect. After optical system has been optimized, for 5 μm, 6 μm, 7 μm, 8 μm, 9 μm and 10 μm waveguides, the coupling efficiency (the ratio of output beam power and input beam power) is 2.7%, 3.6%, 10.0%, 24.5%, 38.9% and 47.1% respectively. The difference in coupling efficiency should be caused by size matching between focused pump beam size and width of waveguide.

5.3.2 Unique Features of Spectra of Backward and Forward Anti-Stokes Signals from Lithium Niobate Waveguide

The spectra of forward and backward anti-Stokes Raman signals from lithium niobate waveguide and bulk material are studied and shown in Fig. 5.4. We use a reversed proton exchange *x*-cut lithium

niobate waveguide with width of 10 μm for generating Raman signals, it has higher photorefractive damage threshold, compared with Ti-diffused $LiNbO_3$. The reversed proton exchange lithium niobate waveguide supports propagation of both ordinary and extraordinary ray [102]. Anti-Stokes signals from waveguide structure [Fig. 5.4(a)] is much stronger than that of bulk materials [Fig. 5.4(b)]. Raman peaks of 200.96 cm^{-1}, 258.68 cm^{-1}, 292.64 cm^{-1}, 348.61 cm^{-1} and 565.90 cm^{-1} are identified for forward anti-Stokes signals and 257.94 cm^{-1} , 282.45 cm^{-1}, 343.93 cm^{-1}, 654.19 cm^{-1} for backward anti-Stokes. The key difference in spectra of forward and backward anti-Stokes is in the high energy peaks: the one for forward anti-Stokes is in 654.19 cm^{-1}, and backward one is in 565.90 cm^{-1}. Phase matching condition is needed in generating backward and forward anti-Stokes:

$$\hbar\omega_p = \hbar\omega_{as} - \hbar\omega_q \quad (1)$$

$$k_p = \pm(k_{as} - q) \quad (2)$$

where $\pm$ sign presents forward and backward anti-Stokes configuration; ω_p, ω_{as}, ω_q are the angular frequency of pump beam, anti-Stokes and phonon, respectively; k_p, k_{as} and q are wave vector of pump beam, anti-Stokes and phonon, respectively.

The value of q is fallen into region of 0 and $2\pi/c$, where c is crystal constant and it is usually few Ångström (Å). q can always satisfy momentum conservation condition. What is more, phase matching always can be guaranteed if the pump beam and anti-Stokes signals are spatially overlapped, since there always exists pair of ω_q and q for satisfying the above expression. It is important to point out that from dispersion relationship, the obvious peak shift between backward anti-Stokes and forward anti-Stokes is not caused by phase matching condition.

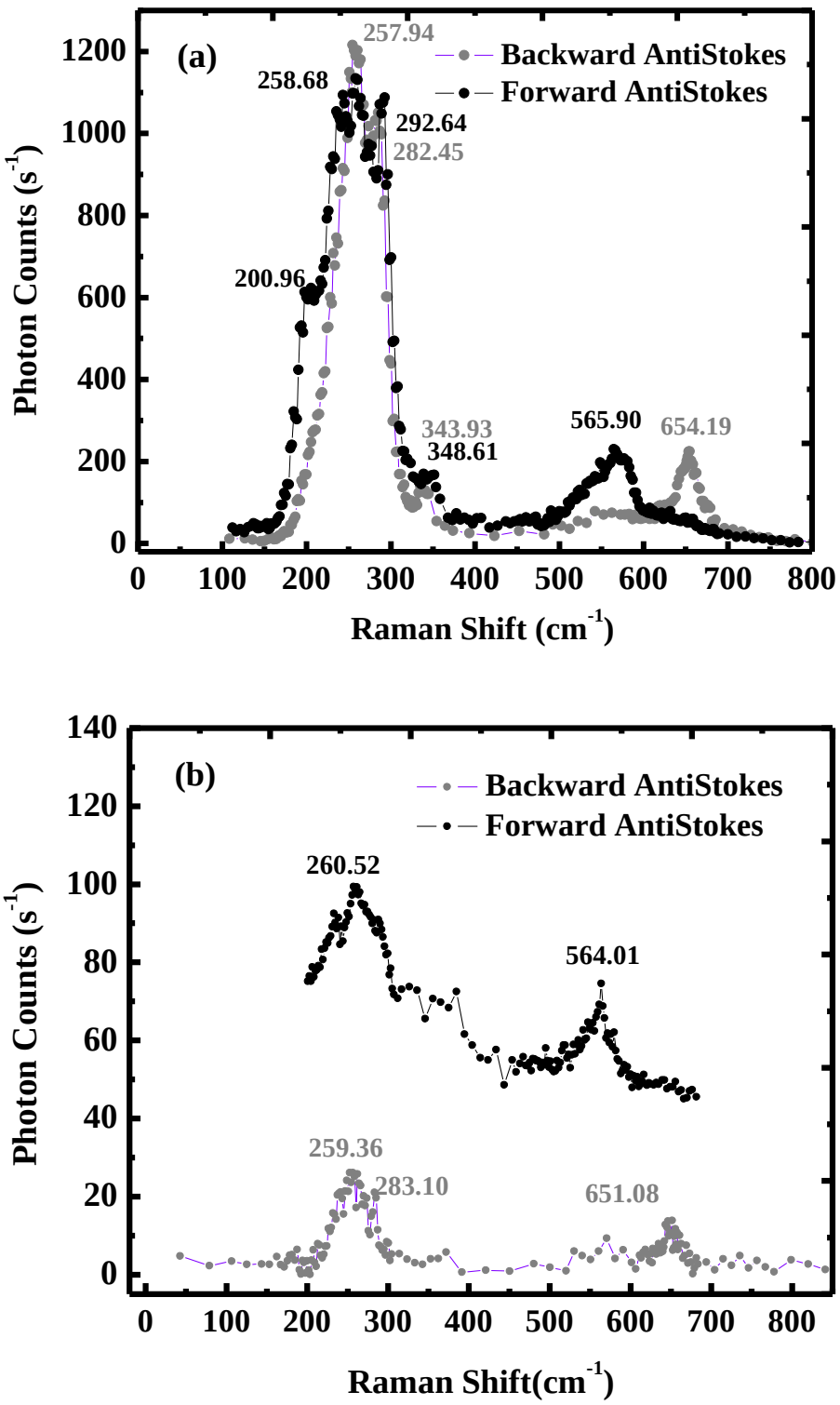

Fig. 5.4. Spectra of forward anti-Stokes and backward anti-Stokes signals from (a) proton exchange lithium niobate waveguide and (b) bulk material.

We here would like to have a discussion on peak shift between forward and backward anti-Stokes signals. The forward and backward spectra can be designated in $Y(Z,Z)Y$ and $Y(Z,Z)\bar{Y}$ in Porto notations, respectively. The phonon modes can be labeled as E(LO1), E(TO3), E(LO3), E(LO4), and E(TO8) for forward anti-Stokes. As shown in Fig. 5.4, the major difference in the spectra of forward and backward anti-Stokes signals lies in the dominant peaks. For forward anti-Stokes, it is at ~565 cm^{-1} and the one for backward anti-Stokes is at ~654 cm^{-1}. From Eq. (1) and (2), one can know that the wave vector for pump beam and anti-Stokes signals are much smaller than $2\pi/c$, and the wave vector for phonon needed for phase matching is very smaller, so the difference in positions of dominant peaks for forward and backward anti-Stokes can not be explained by phase matching. More interestingly, the dominant peak in forward spectrum in 565.90 cm^{-1} corresponds to $Y(ZX)\bar{Y}$ and the one in backward spectrum at 654.19 cm^{-1} corresponds to $Y(ZZ)\bar{Y}$ [103]. There is a tail peak on the left side of dominant peak of backward anti-Stokes, which also corresponds to $Y(ZX)\bar{Y}$. Similarly, there is a tail peak on the right side of that of forward anti-Stokes. The relative intensity of these two peaks {A_1(4TO) and E(8TO)} switches between forward and backward anti-Stokes signals. We right now have not figured out the mechanism yet. More work will be conducted in order to find out the mechanism behind.

Chapter 6 Conclusions and Future work

6.1 Conclusions

In this dissertation, we demonstrate our recent work in applications of nonlinear optics in optical parametrical oscillation, image restoration by phase conjugation, THz generation by difference frequency generation and single photon detection.

In chapter 2, for the first project, we theoretically study the threshold behavior of singly resonant OPO based on twin crystals, to our best knowledge, it is the first time to use matrix methods to calculate its threshold. We experimentally demonstrate nearly degenerate signal twins with wavelength of around 1.57 μm from inverted identical KTA crystals twins based OPO. With careful OPO design, we achieve singly resonant 1.57 μm signal twins from OPO cavity. The OPO threshold is reduced for twin KTAs based OPO, compared with single KTA based OPO. Two different sets of KTAs with crystal length of 15 mm and 23.3 mm are studied. With longer KTA crystal, due to larger parametric gain, the threshold is further reduced and conversion efficiency increases. The second project in Chapter 2 is about generation of multiple coupled OPO for 1 μm beams. We observe strong coupling between two coupled idlers generated from AFB-KTP composite and the idler from bulk KTP. AFB-KTP composite and bulk KTP play the roles of mutual gains in multiple coupled

OPO. For the third project in Chapter 2, we study multiple 2 μm beams from KTP stacks based OPO, the threshold is measured. This is an important step to explore these two sets of idlers and signals for THz generation and image correction.

In chapter 3, the broadband and polarization-insensitive image restoration is investigated in three experiments: novel scheme of image restoration, transmission configuration and reflection configuration of image restoration by phase conjugation from difference frequency generation after blurred by stimulated atmospheric turbulence. Polarization-insensitive image restoration is achieved through AFB-KTP composite. In experiment of novel scheme, we show that wave front is efficiently recovered after original image is blurred by a home-made phase distortion plate. In transmission configuration and reflection configuration of image restoration projects, we demonstrate the phase conjugation can be used in real-time image restoration when input beam is sent through dynamic atmospheric turbulence.

THz wave by difference frequency generation is studied in Chapter 4. In study I, we demonstrate multiple-THz waves generated from AFB-KTP & bulk KTP based singly resonant OPO. At room temperature, THz generated from mixing idler twins in GaSe is much coherent than THz waves by mixing one idler from AFB-KTP and idler from bulk KTP. When the temperature of bulk KTP increases, THz wave from mixing idler twins demonstrates ultrastability. In study II, output power with one order of magnitude higher is observed for THz intensity generated in GaP by mixing idler twins from AFB-KTP based OPO, compared with that of mixing signal and idler from traditional OPO. Our theoretical work based on semi-classical methods shows that such power enhancement is caused by quantum noise reduction, and the significant improvement of coherence between idler twins also demonstrates in linewidth narrowing of THz spectra.

In Chapter 5, we focus on generation of forward and backward anti-Stokes Raman signals from lithium niboate. We observe an enhancement factor of 30 for anti-Stokes signals from waveguide structure, compared with that from bulk material. For Ti-diffused lithium niobate waveguide, at low pump power, it demonstrates linear dependence relationship between pump power and photon counts, and it deviates from such linear dependence when high pump power is used, this is caused by local heating effects. Forward and backward anti-Stokes signals generated from lithium niobate waveguide or bulk material show unique features, especially for the relative intensity of the higher energy peaks.

6.2 Future Work

(I) ~100 GHz can be got from heterodyning of signal twins beams from inverted KTA crystals based OPO via photodiode, such as $In_{1-x}Ga_xAs_{1-y}P_y$ semiconductor materials. The schematic of semiconductor is shown in Fig. 6.1 [32].

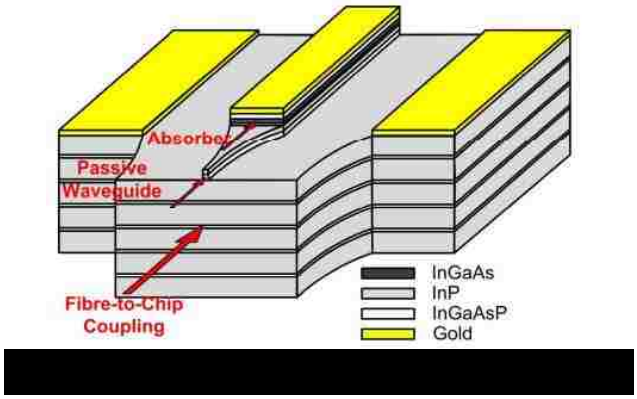

The frequency generated from heterodyning can be accurately designed through controlling thickness of KTA crystal. The signal twins can be applied in carbon dioxide detection in atmosphere with high sensitivity, compared with the conventional differential absorption approach. With signal

twins, we can not only measure the intensity of beams, but also their phase evolution. Signal twins also can be used in restoration of image blurred by dynamic atmospheric turbulence, which is different from the configurations discussed in Chapter 3, we do not need a pump beam in DFG process. Furthermore, twin KTA crystals would be explored for Raman laser [104], and multi-wavelength generated can be used as source for THz generation. For generation of 2 μm beams, two idlers and two signals beams can be explored for THz generation, and the quantum conversion efficiency is expected to be higher than that by mixing 1 μm idler twins beams from AFB-KTP composites.

(II) The optical imaging systems based on DFG can be in explored in bio-imaging for bio-tissue turbidity suppression. Different from our experimental setup in Chapter 3, the objectives are needed for focusing beams to decrease scattering by bio-tissue. The specific configurations are demonstrated as following:

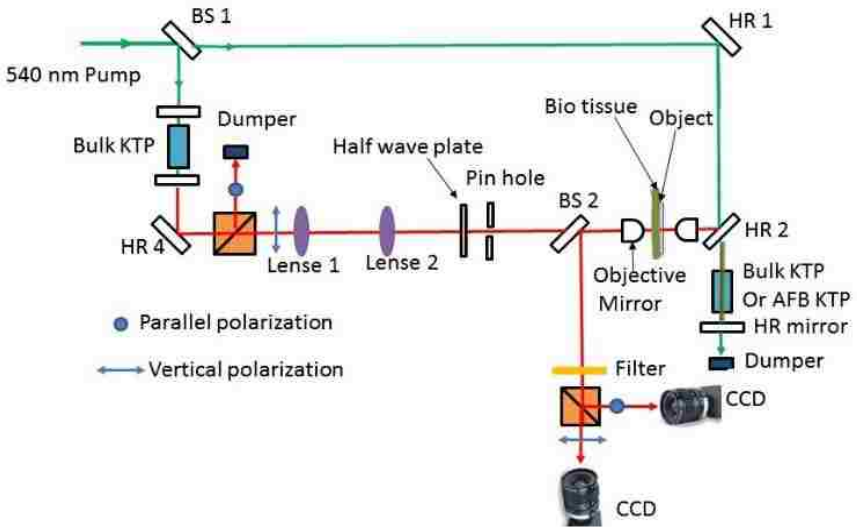

Fig. 6.2. Experimental setup for transmission configuration of image restoration based on DFG for bio-turbidity suppression in bio-imaging.

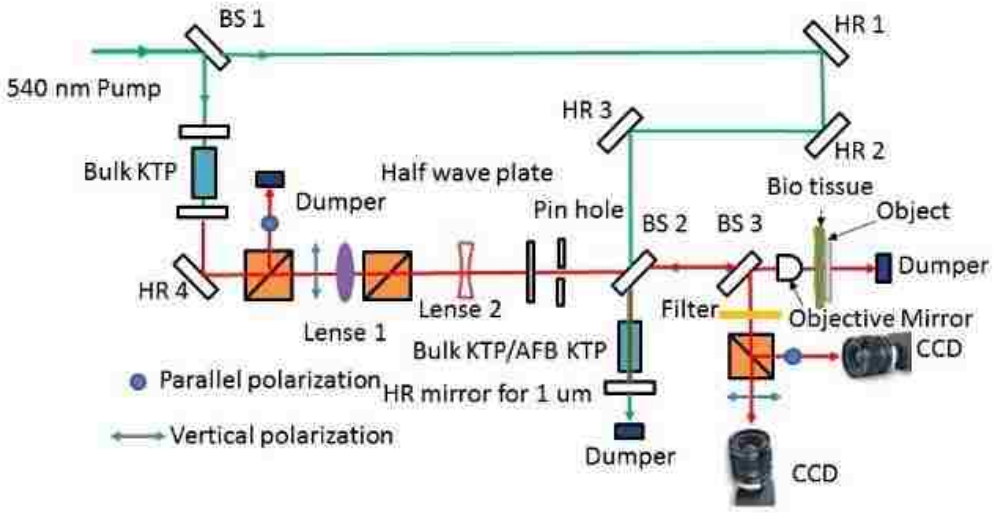

Fig. 6.3. Experimental setup for reflection configuration of image restoration based on DFG for bio-turbidity suppression in bio-imaging.

And we also would like to test our optical system in field, and in other poor vision environments full with other distortion mediums, such as aerosol or polymer. Pulsed laser is used in the optical systems in Chapter 3, we plan to adopt continuous laser for generating original image, and the corresponding continuous recovered images can be collected. The reflection configuration of image restoration can be made into a compact box with a diode laser source, and optical system can become a portal device for daily usage.

(III) Quantum noise reduction will be studied for low frequency THz generation, such as 0.1 THz. Since two idlers are much coherent than idler-signal beams, low frequency THz output beams from mixing idler twins beams from inverted KTA crystals based OPO should own higher output power and narrowing linewidth. The corresponding theoretical work is proposed to be done for this part of result from THz generation experiment.

(IV) For single photon detection project, we can combine our single photon detection system with laser amplifier, so the anti-Stoke signals can be amplified to be large signal. Furthermore, other

nonlinear materials, such as PP-$KTiPO_4$ and GaP, can be explored for achieving generation of backward and forward anti-Stokes signals, since there is local heating problem for lithium niobate waveguide or bulk materials used in Chapter 5.

References

[1] R. Boyd, Nonlinear Optics, Academic Press, 2010.

[2] A. Yariv, Quantum Electronics, Wiley, 1989.

[3] W. Shi, Y. J. Ding, N. Fernelius, and K. Vodopyanov, "Efficient, Tunable, and Coherent 0.18-5.27 THz Source Based on GaSe Crystal," Optics Letters 27, 1454 (2002).

[4] Y. Jiang, and Y. J. Ding, "Efficient Terahertz Generation from Two Collinearly Propagating CO_2 Laser Pulses," Applied Physics Letters 91, 091108 (2007).

[5] B. E. A. Saleh, and M. C. Teich, "Nonlinear Optics," in Fundamentals of Photonics, John Wiley & Sons, 2001.

[6] D. N. Nikogosyan, Nonlinear Optical Crystals, Springer, 2005.

[7] L. W. Kornaszewski, N. Gayraud, J. M. Stone, W. N. MacPherson, A. K. George, J. C. Knight, D. P. Hand, and D. T. Reid, "Mid-Infrared Methane Detection in a Photonic Bandgap Fiber Using a Broadband Optical Parametric Oscillator," Optics Express 15, 11219 (2007).

[8] L. Kong, M. Ji, G. R. Holtom, D. Fu, C. W. Freudiger, and X. S. Xie, "Multicolor Stimulated Raman Scattering Microscopy with a Rapidly Tunable Optical Parametric Oscillator," Optics Letters 38, 145 (2013).

[9] J. Howell, P. Anisimov, J. Dowling, and R. Boyd, "Single and Biphoton Imaging and High Dimensional Quantum Communication," Quantum Information Processing 11, 925 (2012).

[10] A. Amediek, A. Fix, M. Wirth, and G. Ehret, "Development of an OPO System at 1.57 μm for Integrated Path Dial Measurement of Atmospheric Carbon Dioxide," Applied Physics B 92, 295 (2008).

[11] J.-J. Zondy, M. Abed, and S. Khodja, "Twin-Crystal Walk-Off-Compensated Type-II Second-Harmonic Generation: Single-Pass and Cavity-Enhanced Experiments in $KTiOPO_4$," Journal of the Optical Society of America B 11, 2368 (1994).

[12] X. Mu, H. Meissner, and H.-C. Lee, "Optical Parametric Oscillations of 2 μm in Multiple-Layer Bonded Walk-Off Compensated KTP Stacks," Optics Letters 35, 387 (2010).

[13] X. Mu, H.-C. Lee, and H. Meissner, "Walk-Off Corrected KTP Crystal for Low Pulse Energy Pumped Optical Parametric Oscillation," presented at the Proceding of SPIE 71972009.

[14] P. Zhao, S. Ragam, Y. J. Ding, I. B. Zotova, X. Mu, H.-C. Lee, S. K. Meissner, and H. Meissner, "Singly Resonant Optical Parametric Oscillator Based on Adhesive-Free-Bonded Periodically Inverted $KTiOPO_4$ Plates: Terahertz Generation by Mixing a Pair of Idler Waves," Optics Letters 37, 1283 (2012).

[15] X. Zou, P. Zhao, P. Hong, X. Lin, Y. J. Ding, X. Mu, H.-C. Lee, S. K. Meissner, and H. Meissner, "Restoration of Blurred Images Due to Phase Distortion Based on Polarization-Insensitive Phase Conjugation in Second-Order Nonlinear Medium," Optics Letters 38, 3054 (2013).

[16] X. Zou, P. Hong, and Y. J. Ding, "Recovery of Image Distorted by Turbulent Atmosphere Using Phase-Conjugate Image Generated by Difference Frequency Generation," Applied Physics Letters 105, 241105 (2014).

[17] P. Hong, X. Zou, D. Li, J. Y. Ding, and Z. Liu, "Image Restoration Based on Phase Conjugation in Second Order Nonlinear Crystal under Reflection Configuration," Applied Optics 54, 6172 (2015).

[18] X. Zou, P. Hong, D. Li, Y. J. Ding, X. Mu, H.-C. Lee, S. K. Meissner, and H. Meissner, "Highly Coherent Idler Twins Generated by Coupled Optical Parametric Oscillators for Enhancement of THz Generation " Laser and Photonics Review (submitted).

[19] K. Miyamoto, and H. Ito, "Wavelength-Agile Mid-Infrared (5-10 μm) Generation Using a Galvano-Controlled $KTiOPO_4$ Optical Parametric Oscillator," Optics Letters 32, 274 (2007).
[20] P. Hong, D. Li, X. Zou, J. Y. Ding, and Z. Liu, "Nearly-Degenerate Twin Signals Generated by Inverted $KTiOAsO_4$ Twin Crystals Optical Parametric Oscillator," Applied Physics Letters (submitted).
[21] R. Wang, P. Hong, X. Zou, Y. J. Ding, X. Mu, H.-C. Lee, S. Meissner, and H. Meissner, "Investigation of Multiple Coupled Optical Parametric Oscillators," in CLEO: 2014 (Optical Society of America, San Jose, California), P. JTh2A.67.
[22] W. R. Bosenberg, L. K. Cheng, and J. D. Bierlein, "Optical Parametric Frequency Conversion Properties of $KTiOAsO_4$," Applied Physics Letters 65, 2765 (1994).
[23] M. S. Webb, P. F. Moulton, J. J. Kasinski, R. L. Burnham, G. Loiacono, and R. Stolzenberger, "High-Average-Power $KTiOAsO_4$ Optical Parametric Oscillator," Optics Letters 23, 1161 (1998).
[24] D. Sakaizawa, C. Nagasawa, T. Nagai, M. Abo, Y. Shibata, M. Nakazato, and T. Sakai, "Development of a 1.6 μm Differential Absorption Lidar with a Quasi-Phase-Matching Optical Parametric Oscillator and Photon-Counting Detector for the Vertical CO_2 Profile," Applied Optics 48, 748 (2009).
[25] J. Mao, and S. R. Kawa, "Sensitivity Studies for Space-Based Measurement of Atmospheric Total Column Carbon Dioxide by Reflected Sunlight," Applied Optics 43, 914 (2004).
[26] M. Imaki, S. Kameyama, Y. Hirano, S. Ueno, D. Sakaizawa, S. Kawakami, and M. Nakajima, "Laser Absorption Spectrometer Using Frequency Chirped Intensity Modulation at 1.57 μm Wavelength for CO_2 Measurement," Optics Letters 37, 2688 (2012).
[27] Q. B. Sun, H. J. Liu, N. Huang, C. Ruan, S. L. Zhu, and W. Zhao, "High Energy and High Efficiency 3.4 μm Extracavity KTA Optical Parametric Oscillator," Laser Physics Letters 8, 16 (2011).
[28] R. F. Wu, K. S. Lai, H. Wong, W.-J. Xie, Y. Lim, and E. Lau, "Multiwatt Mid-IR Output from a Nd:YALO Laser Pumped Intracavity KTA OPO," Optics Express 8, 694 (2001).
[29] F. Bai, Q. Wang, Z. Liu, X. Zhang, X. Wan, W. Lan, G. Jin, X. Tao, and Y. Sun, "Theoretical and Experimental Studies on Output Characteristics of an Intracavity KTA OPO," Optics Express 20, 807 (2012).
[30] W. Wang, Z. Cong, Z. Liu, X. Zhang, Z. Qin, G. Tang, N. Li, Y. Zhang, and Q. Lu, "THz-Wave Generation Via Stimulated Polariton Scattering in $KTiOAsO_4$ Crystal," Optics Express 22, 17092 (2014).
[31] W. Wang, Z. Cong, X. Chen, X. Zhang, Z. Qin, G. Tang, N. Li, C. Wang, and Q. Lu, "Terahertz Parametric Oscillator Based on $KTiOPO_4$ Crystal," Optics Letters 39, 3706 (2014).
[32] E. Rouvalis, C. C. Renaud, D. G. Moodie, M. J. Robertson, and A. J. Seeds, "Traveling-Wave Uni-Traveling Carrier Photodiodes for Continuous Wave THz Generation," Optics Express 18, 11105 (2010).
[33] Z. Liu, Q. Wang, X. Zhang, Z. Liu, J. Chang, H. Wang, S. Zhang, S. Fan, G. Jin, X. Tao, S. Zhang, and H. Zhang, "Coexistent Optical Parametric Oscillation and Stimulated Raman Scattering in $KTiOAsO_4$," Optics Express 16, 17092 (2008).
[34] V. Pasiskevicius, A. Fragemann, F. Laurell, R. Butkus, V. Smilgevicius, and A. Piskarskas, "Enhanced Stimulated Raman Scattering in Optical Parametric Oscillators from Periodically Poled $KTiOAsO_4$," Applied Physics Letters 82, 325 (2003).
[35] J. D. Bierlein, and H. Vanherzeele, "Potassium Titanyl Phosphate: Properties and New Applications," Journal of the Optical Society of America B 6, 622 (1989).
[36] T. Taniuchi, J. Shikata, and H. Ito, "Tunable Terahertz-Wave Generation in Dast Crystal with Dual-Wavelength KTP Optical Parametric Oscillator," Electronics Letters 36, 1414 (2000).
[37] H. Ito, K. Suizu, T. Yamashitay, A. Nawahara, and T. Sato, "Random Frequency Accessible Broad

Tunable Terahertz-Wave Source Using Phase-Matched 4-Dimethylamino-N-Methyl-4-Stilbazolium Tosylate Crystal," Janpanese Journal of Applied Physics 46, 7321 (2007).
[38] I. T. Sorokina, and E. Sorokin, "Principles, Advances and Applications of Ultrafast Mid-Infrared Lasers," in Lasers & Electro Optics & The Pacific Rim Conference on Lasers and Electro-Optics, 2009. CLEO/PACIFIC RIM '09. Conference on(2009), pp.1-2.
[39] H. Iwai, S. Ishii, R. Oda, K. Mizutani, S. Sekizawa, and Y. Murayama, "Performance and Technique of Coherent 2 μm Differential Absorption and Wind Lidar for Wind Measurement," Journal of Atmospheric and Oceanic Technology 30, 429 (2012).
[40] B. Y. Zeldovich, V. I. Popovichev, V. V. Ragulskii, and F. S. Faisullov, "Connection between the Wavefronts of the Reflected and Exciting Light in Stimulated Mandelshtam–Brillouin Scattering," Sov. Phys. JETP 15, 109 (1972).
[41] Z. Yaqoob, D. Psaltis, M. S. Feld, and C. Yang, "Optical Phase Conjugation for Turbidity Suppression in Biological Samples," Nature Photonics 2, 110 (2008).
[42] F. Paleari, A. Andreoni, M. Bondani, and V. Parfenov, "Phase Conjugation to Recover from Modal Dispersion in Propagation through Fibers," Journal of the Optical Society of America B 23, 812 (2006).
[43] M. R. Fewings, and A. L. Gaeta, "Compensation of Pulse Distortions by Phase Conjugation Via Difference-Frequency Generation," Journal of the Optical Society of America B 17, 1522 (2000).
[44] M. Bondani, A. Allevi, A. Brega, E. Puddu, and A. Andreoni, "Difference-Frequency-Generated Holograms of Two-Dimensional Objects," Journal of the Optical Society of America B 21, 280 (2004).
[45] G. S. He, "Optical Phase Conjugation: Principles, Techniques, and Applications," Progress in Quantum Electronics 26, 131 (2002).
[46] I. M. Vellekoop, M. Cui, and C. Yang, "Digital Optical Phase Conjugation of Fluorescence in Turbid Tissue," Applied Physics Letters 101, 081108 (2012).
[47] T. R. Hillman, T. Yamauchi, W. Choi, R. R. Dasari, M. S. Feld, Y. Park, and Z. Yaqoob, "Digital Optical Phase Conjugation for Delivering Two-Dimensional Images through Turbid Media," Scientific Report 3 (2013).
[48] M. Cui, E. J. McDowell, and C. Yang, "An in Vivo Study of Turbidity Suppression by Optical Phase Conjugation (TSOPC) on Rabbit Ear," Optics Express 18, 25 (2010).
[49] D. M. Bloom, and G. C. Bjorklund, "Conjugate Wave-Front Generation and Image Reconstruction by Four-Wave Mixing," Applied Physics Letters 31, 592 (1977).
[50] I. V. Tomov, B. VanWonterghem, A. S. Dvornikov, T. E. Dutton, and P. M. Rentzepis, "Degenerate Four-Wave Mixing in Azo-Dye-Doped Polymer Films," Journal of the Optical Society of America B 8, 1477 (1991).
[51] P. Günter, and J.-P. Huignard, Photorefractive Materials and Their Applications 1, Springer, 2006.
[52] P. Yeh, "Fundamental Limit of the Speed of Photorefractive Effect and Its Impact on Device Applications and Material Research," Applied Optics 26, 602 (1987).
[53] C. A. Primmerman, D. V. Murphy, D. A. Page, B. G. Zollars, and H. T. Barclay, "Compensation of Atmospheric Optical Distortion Using a Synthetic Beacon," Nature 353, 141 (1991).
[54] D. Korff, "Analysis of a Method for Obtaining Near-Diffraction-Limited Information in the Presence of Atmospheric Turbulence," Journal of the Optical Society of America 63, 971 (1973).
[55] G. C. Holst, Testing and Evaluation of Infrared Imaging Systems, JCD Publishing, Winter Park & SPIE Optical Engineering Press, Bellingham, 2008.
[56] F. Devaux, E. Guiot, and E. Lantz, "Image Restoration through Aberrant Media by Optical Phase Conjugation in a Type II Three-Wave Mixing Interaction," Optics Letters 23, 1597 (1998).

[57] F. Devaux, G. le Tolguenec, and E. Lantz, "Phase Conjugate Imaging by Type II Parametric Amplification," Optics Communications 147, 309 (1998).
[58] V. N. Mikhailov, M. Bondani, F. Paleari, and A. Andreoni, "Optical Phase Conjugation in Difference-Frequency Generation," Journal of the Optical Society of America B 20, 1715 (2003).
[59] V. I. Sokolov, A. M. Nugumanov, and R. V. Smirnov, "Phase Conjugation of Broadband Light at Three-Wave Mixing in a Nonlinear Crystal," Optics Communications 189, 377(2001).
[60] V. Kemlin, D. Jegouso, J. Debray, E. Boursier, P. Segonds, B. Boulanger, H. Ishizuki, T. Taira, G. Mennerat, J.-M. Melkonian, and A. Godard, "Dual-Wavelength Source from 5% MgO:PPLN Cylinders for the Characterization of Nonlinear Infrared Crystals," Optics Express 21, 28886 (2013).
[61] Y. J. Ding, "Phase Conjugation Based on Single Backward Second-Order Nonlinear Parametric Process," Optics Letters 37, 4792 (2012).
[62] P. Hong, X. Zou, D. Li, Y. J. Ding, and Z. Liu, "Image Restoration Based on Phase Conjugation in Second-Order Nonlinear Materials under Reflection Configuration," Applied Optics 54, 6172 (2015).
[63] R. Rampy, D. Gavel, D. Dillon, and S. Thomas, "Production of Phase Screens for Simulation of Atmospheric Turbulence," Applied Optics 51, 8769 (2012).
[64] T. A. Rhoadarmer, and J. R. P. Angel, "Low-Cost, Broadband Static Phase Plate for Generating Atmosphericlike Turbulence," Applied Optics 40, 2946 (2001).
[65] X. Zou, P. Hong, and Y. J. Ding, "Recovery of Image after Distortion by Atmospheric Turbulence Using Phase-Conjugate Beam through Difference Frequency Generation," in CLEO:2014 (Optical Society of America, San Jose, California, 2014), p. JTh2A.103.
[66] D. N. Nikogosyan, Nonlinear Optical Crystals*:* A Complete Survey, Springer, NY, 2005.
[67] T. Y. Fan, C. E. Huang, B. Q. Hu, R. C. Eckardt, Y. X. Fan, R. L. Byer, and R. S. Feigelson, "Second Harmonic Generation and Accurate Index of Refraction Measurements in Flux-Grown $KTiOPO_4$," Applied Optics 26, 2390 (1987).
[68] Y. J. Ding, J. B. Khurgin, and S.-J. Lee, "Optical Phase Conjugation and Waveguide Coupling by Cascading Transverse Second-Harmonic and Difference-Frequency Generation in a Vertical Cavity," Optical Quantum Electronics 28, 1617 (1996).
[69] Y.-Q. Lu, Z.-L. Wan, Q. Wang, Y.-X. Xi, and N.-B. Ming, "Electro-Optic Effect of Periodically Poled Optical Superlattice $LiNbO_3$ and Its Applications," Applied Physics Letters 77, 3719 (2000).
[70] B. Ferguson, and X.-C. Zhang, "Materials for Terahertz Science and Technology," Nature Materials 1, 26 (2002).
[71] Y.-W. Huang, T.-F. Tseng, C.-C. Kuo, Y.-J. Hwang, and C.-K. Sun, "Fiber-Based Swept-Source Terahertz Radar," Optics Letters 35, 1344 (2010).
[72] M. Walther, B. Fischer, A. Ortner, A. Bitzer, A. Thoman, and H. Helm, "Chemical Sensing and Imaging with Pulsed Terahertz Radiation," Analytical and Bioanalytical Chemistry 397, 1009 (2010).
[73] A. Arora, T. Q. Luong, M. Kruger, Y. J. Kim, C.-H. Nam, A. Manz, and M. Havenith, "Terahertz-Time Domain Spectroscopy for the Detection of PCR Amplified DNA in Aqueous Solution," Analyst 137, 575 (2012).
[74] M. Nagel, P. Haring Bolivar, M. Brucherseifer, H. Kurz, A. Bosserhoff, and R. Büttner, "Integrated THz Technology for Label-Free Genetic Diagnostics," Applied Physics Letters 80, 154 (2002).
[75] I. Amenabar, F. Lopez, and A. Mendikute, "In Introductory Review to THz Non-Destructive Testing of Composite Mater," Journal of Infrared, Millimeter, and Terahertz Waves 34, 152 (2013).
[76] Y. S. Lee, T. Meade, T. B. Norris, and A. Galvanauskas, "Tunable Narrow-Band Terahertz Generation from Periodically Poled Lithium Niobate," Applied Physics Letters 78, 3583 (2001).

[77] B. S. Williams, H. Callebaut, S. Kumar, Q. Hu, and J. L. Reno, "3.4-THz Quantum Cascade Laser Based on Longitudinal-Optical-Phonon Scattering for Depopulation," Applied Physics Letters 82, 1015 (2003).
[78] G. D. Boyd, T. J. Bridges, C. K. N. Patel, and E. Buehler, "Phase-Matched Submillimeter Wave Generation by Difference-Frequency Mixing in $ZnGeP_2$," Applied Physics Letters 21, 553 (1972).
[79] G. Arisholm, "Quantum Noise Initiation and Macroscopic Fluctuations in Optical Parametric Oscillators," Journal of the Optical Society of America B 16, 117 (1999).
[80] K. Suizu, K. Miyamoto, T. Yamashita, and H. Ito, "High-Power Terahertz-Wave Generation Using Dast Crystal and Detection Using Mid-Infrared Powermeter," Optics Letters 32, 2885 (2007).
[81] W. J. Munro, and M. D. Reid, "Quantum Noise Reduction in the Squeezed Pump Non-Degenerate Parametric Oscillator " Quantum Optics 4, 181 (1992).
[82] A. Heidmann, R. J. Horowicz, S. Reynaud, E. Giacobino, C. Fabre, and G. Camy, "Observation of Quantum Noise Reduction on Twin Laser Beams," Physical Review Letters 59, 2555 (1987).
[83] M. D. Reid, and P. D. Drummond, "Correlations in Nondegenerate Parametric Oscillation: Squeezing in the Presence of Phase Diffusion," Physical Review A 40, 4493 (1989).
[84] H. Pengda, W. Ran, Z. Xingquan, Y. J. Ding, M. Xiaodong, L. Huai-Chuan, S. K. Meissner, and H. Meissner, "Ultrastable THz Generation Based on Frequency Mixing of Output Beams from Coupled Optical Parametric Oscillators," in Photonics Conference (IPC), 2014 IEEE(2014), pp. 398-399.
[85] X. Zou, P. Hong, D. Li, and Y. J. Ding, "Power Enhancement, Noise Reduction, and Linewidth Narrowing of THz Output by Mixing Beams from Coupled Oscillators," in CLEO: 2014(Optical Society of America, San Jose, California, 2014), p. JTh2A.105.
[86] C. Fabre, E. Giacobino, A. Heidmann, and S. Reynaud, "Noise Characteristics of a Non-Degenerate Optical Parametric Oscillator - Application to Quantum Noise Reduction," Journal of Physics. France 50, 12009 (1989).
[87] D. Wang, Y. Shang, X. Jia, C. Xie, and K. Peng, "Dependence of Quantum Correlations of Twin Beams on the Pump Finesse of an Optical Parametric Oscillator," Journal of Physics B 41 (2008).
[88] Y. Repelin, E. Husson, F. Bennani, and C. Proust, "Raman Spectroscopy of Lithium Niobate and Lithium Tantalate. Force Field Calculations," Journal of Physics and Chemistry of Solids 60, 819 (1999).
[89] K. T. Tsen, D. K. Ferry, A. Botchkarev, B. Sverdlov, A. Salvador, and H. Morkoc, "Time-Resolved Raman Studies of the Decay of the Longitudinal Optical Phonons in Wurtzite Gan," Applied Physics Letters 72, 2132 (1998).
[90] K. T. Tsen, D. K. Ferry, A. Botchkarev, B. Sverdlov, A. Salvador, and H. Morkoç, "Direct Measurements of Electron-Longitudinal Optical Phonon Scattering Rates in Wurtzite Gan," Applied Physics Letters 71, 1852 (1997).
[91] H. Fujimori, M. Kakihana, K. Ioku, S. Goto, and M. Yoshimura, "Advantage of Anti-Stokes Raman Scattering for High-Temperature Measurements," Applied Physics Letters 79, 937 (2001).
[92] D. S. Moore, and S. D. McGrane, "Raman Temperature Measurement," presented at the Journal of Physics: Conference Series 2014.
[93] Y. J. Ding, and J. B. Khurgin, "From Anti-Stokes Photoluminescence to Resonant Raman Scattering in Gan Single Crystals and Gan-Based Heterostructures," Laser & Photonics Reviews 6, 660 (2012).
[94] G. Xu, S. K. Tripathy, X. Mu, Y. J. Ding, K. Wang, Y. Cao, D. Jena, and J. B. Khurgin, "Stokes and Anti-Stokes Resonant Raman Scatterings from Biased Gan/Aln Heterostructure," Applied Physics Letters 93, 051912 (2008).
[95] Y. Zhang, Y.-R. Zhen, O. Neumann, J. K. Day, P. Nordlander, and N. J. Halas, "Coherent Anti-

Stokes Raman Scattering with Single-Molecule Sensitivity Using a Plasmonic Fano Resonance," Nature Communication 5 (2014).
[96] R. F. Schaufele, and M. J. Weber, "Raman Scattering by Lithium Niobate," Physical Review 152, 705 (1966).
[97] S. Kouteva-Arguirova, T. Arguirov, D. Wolfframm, and J. Reif, "Influence of Local Heating on Micro-Raman Spectroscopy of Silicon," Journal of Applied Physics 94, 4946 (2003).
[98] D. Li, Y. Jiang, Y. J. Ding, I. B. Zotova, and N. S. Prasad, "Approaching Single-Photon Detection in Near-Infrared Region," Applied Physics Letters 101, 141126 (2012).
[99] D. Li, P. Hong, Y. J. Ding, Z. Liu, L. Wang, P.-R. Hua, and D.-L. Zhang, "Investigation of Enhanced Forward and Backward Anti-Stokes Raman Signals in Lithium Niobate Waveguides," Journal of Applied Physics 118, 013107 (2015).
[100] P. Hermet, M. Veithen, and P. Ghosez, "First-Principles Calculations of the Nonlinear Optical Susceptibilities and Raman Scattering Spectra of Lithium Niobate," Journal of Physics: Condensed Matter 19 (2007).
[101] T. C. Damen, S. P. S. Porto, and B. Tell, "Raman Effect in Zinc Oxide," Physical Review 142, 570 (1966).
[102] Y. N. Korkishko, V. A. Fedorov, T. M. Morozova, F. Caccavale, F. Gonella, and F. Segato, "Reverse Proton Exchange for Buried Waveguides in $LiNbO_3$," Journal of the Optical Society of America A 15, 1838 (1998).
[103] S. Margueron, A. Bartasyte, A. M. Glazer, E. Simon, J. Hlinka, I. Gregora, and J. Gleize, "Resolved E-Symmetry Zone-Centre Phonons in $LiTaO_3$ and $LiNbO_3$," Journal of Applied Physics 111, 104105 (2012).
[104] Y. T. Chang, Y. P. Huang, K. W. Su, and Y. F. Chen, "Diode-Pumped Multi-Frequency Q-Switched Laser with Intracavity Cascade Raman Emission," Optics Express 16, 8286 (2008).

Biography

Publication

Journal Papers

1. Pengda Hong, Xingquan Zou, Da Li, and Yujie J. Ding, Zhaojun Liu, Image Restoration Based on Phase Conjugation in Second-Order Nonlinear Materials under Reflection Configuration, Appl. Opt. 54, 6172 (2015).

2. Pengda Hong, Da Li, Xingquan Zou and Yujie J. Ding, Zhaojun Liu, Nearly-Degenerate Twin Signals Generated by Optical Parametric Oscillator in Inverted KTA Twin Crystals, Submitted for Appl. Phys. Letters.

3. Da Li*, Pengda Hong*, Yujie J. Ding, Zhaojun Liu, Lei Wang, Ping-Rang Hua, and De-Long Zhang, Enhanced Forward and Backward Anti-Stokes Raman Signals in Lithium Niobate Waveguides, J. Appl. Phys. 118, 013107 (2015), co-first author.

4. Xingquan Zou*, Pengda Hong*, Da Li, Yujie J. Ding, Xiaodong Mu, Huai-Chuan Lee, Stephanie K. Meissner, and Helmuth Meissner, Highly Coherent Idler Twins Generated by Coupled Optical Parametric Oscillators for Enhancement of THz Generation, Submitted for Laser Photonics Rev, co-first author.

5. Xingquan Zou, Pengda Hong, and Yujie Ding, Recovery of Image Distorted by Turbulent Atmosphere Using Phase-Conjugate Image Generated by Difference Frequency Generation. Appl. Phys. Letters. 105, 241105 (2014).

6. Xingquan Zou, Pu Zhao, Pengda Hong, Xiaomu Lin, Yujie J. Ding, Xiaodong Mu, Huai-Chuan Lee, Stephanie K. Meissner, and Helmuth Meissner, Restoration of Blurred Images Due to Phase Distortion Based on Polarization-Insensitive Phase Conjugation in Second-Order Nonlinear Medium. Opt. Letters. 38, 16 (2013).

Conference Papers

1. Pengda Hong, Xingquan Zou, Da Li, Ruolin Chen, Liang Gao, and Yujie J. Ding, Zhaojun Liu, Reflection-Mode Image Restoration through Optical Phase Conjugate Beams in Second-Order Nonlinear Crystal, IEEE Photonics , 2015, Virginia, Accepted.

2. Pengda Hong, Da Li, Xingquan Zou and Yujie J. Ding, Zhaojun Liu, Investigation of Degenerate

1.5 μm Beams from KTA Optical Parametric Oscillator, IEEE Photonics, 2015, Virginia, Accepted.

3. Pengda Hong, Ran Wang, Xingquan Zou, and Yujie J. Ding, Xiaodong Mu, Huai-Chuan Lee, Stephanie K. Meissner, and Helmuth Meissner, Ultrastable THz Generation Based on Frequency Mixing of Output Beams from Coupled Optical Parametric Oscillators, IEEE Photonics, 2014, San Diego, California, WB 3.4

4. Xingquan Zou, Pengda Hong, Yujie J.Ding, Image Restoration Based On Phase Conjugation in Second-Order Nonlinear Medium, IEEE Photonics 2014, San Diego, California, WB 4.4

5. Xingquan Zou, Pengda Hong, Da Li, Yujie J Ding, Power Enhancement, Noise Reduction, and Linewidth Narrowing of THz Output by Mixing Beams from Coupled Oscillators, Conference on Lasers and Electro-Optics 2014, San Jose, California: QELS_Fundamental Science, JTh2A. 105

6. Xingquan Zou, Pengda Hong, Yujie Ding, Recovery of Image after Distortion by Atmospheric Turbulence Using Phase-Conjugate Beam through Difference Frequency Generation, Conference on Lasers and Electro-Optics 2014, San Jose, California: Applications and Technology, JTh2A. 103

7. Da Li, Pengda Hong, Zhaojun Liu, Yujie J Ding, Lei Wang, Enhanced Forward and Backward Anti-Stokes Raman Signals in Lithium Niobate Waveguides, Conference on Lasers and Electro-Optics 2014, San Jose, California: QELS_Fundamental Science, JW2A. 103

8. Ran Wang, Pengda Hong, Xingquan Zou, Yujie J Ding, Xiaodong Mu, Huai-Chuan Lee, Stephanie Meissner, Helmuth Meissner, Investigation of Multiple Coupled Optical Parametric Oscillators, Conference on Lasers and Electro-Optics 2014, San Jose, California: Science and Innovations, JTh2A. 67

9. Da Li, Zhaojun Liu, Pengda Hong, Yujie J Ding, Lei Wang, Ping-Rang Hua, De-Long Zhang, Enhancement of Backward-Propagating Anti-Stokes Raman Scattering from Ti-diffused Lithium Niobate Waveguides, Conference on Lasers and Electro-Optics 2013, San Jose, California: QELS_Fundamental Science, QF1D. 4

10. Xingquan Zou, Xiaomu Lin, Pu Zhao, Pengda Hong, Yujie J. Ding, Xiaodong Mu, Huai-Chuan Lee, Stephanie K. Meissner, and Helmuth Meissner, Restoration of Blurred Images Due to Phase Distortion Based on Polarization-Insensitive Phase Conjugation in Second-Order Nonlinear Medium: Novel Scheme, Conference on Lasers and Electro-Optics 2013, San Jose, California: QELS_Fundamental Science, QM4E. 5

Vita

Pengda Hong got B.Sc in Applied Physics from Sichuan University, Chengdu, China, and Master of Philosophy in Physics from University of Hong Kong. He right now studies in Electrical and Computer Engineering of Lehigh University for Ph.D. and his research focus is in nonlinear optics, including solid state laser, optical parametric oscillator, image restoration, THz generation and detection and waveguide structure for single photon detection.